INFORMATION TO USERS

This reproduction was made from a copy of a document sent to us for microfilming. While the most advanced technology has been used to photograph and reproduce this document, the quality of the reproduction is heavily dependent upon the quality of the material submitted.

The following explanation of techniques is provided to help clarify markings or notations which may appear on this reproduction.

1. The sign or "target" for pages apparently lacking from the document photographed is "Missing Page(s)". If it was possible to obtain the missing page(s) or section, they are spliced into the film along with adjacent pages. This may have necessitated cutting through an image and duplicating adjacent pages to assure complete continuity.

2. When an image on the film is obliterated with a round black mark, it is an indication of either blurred copy because of movement during exposure, duplicate copy, or copyrighted materials that should not have been filmed. For blurred pages, a good image of the page can be found in the adjacent frame. If copyrighted materials were deleted, a target note will appear listing the pages in the adjacent frame.

3. When a map, drawing or chart, etc., is part of the material being photographed, a definite method of "sectioning" the material has been followed. It is customary to begin filming at the upper left hand corner of a large sheet and to continue from left to right in equal sections with small overlaps. If necessary, sectioning is continued again—beginning below the first row and continuing on until complete.

4. For illustrations that cannot be satisfactorily reproduced by xerographic means, photographic prints can be purchased at additional cost and inserted into your xerographic copy. These prints are available upon request from the Dissertations Customer Services Department.

5. Some pages in any document may have indistinct print. In all cases the best available copy has been filmed.

University Microfilms International
300 N. Zeeb Road
Ann Arbor, MI 48106

Jan, Gwo-Jen

OPTICAL, MODULATED OPTICAL AND RAMAN SCATTERING STUDY OF HYDROGENATED AND FLUORINATED AMORPHOUS SILICON

City University of New York PH.D. 1982

OPTICAL, MODULATED OPTICAL AND RAMAN SCATTERING STUDY OF HYDROGENATED AND FLUORINATED AMORPHOUS SILICON

BY

GWO-JEN JAN

A DISSERTATION SUBMITTED TO THE GRADUATE FACULTY IN PHYSICS IN PARTIAL FULLFILLMENT OF THE REQUIREMENTS FOR THE DEGREE OF DOCTOR OF PHILOSOPHY, THE CITY UNIVERSITY OF NEW YORK.

1982

This manuscript has been read and accepted for the graduate faculty in physics in satisfaction of the dissertation requirement for the degree of doctor of philosophy.

1/23/82
Date

Fred H. Pollak
Chairman of Examining Committee
Fred H. Pollak

9/22/82
Date

Executive Officer

1 Frederick W. Smith
Frederick W. Smith

2 Joseph B. Krieger
Joseph B. Krieger

3 George Skorinko
George Skorinko

4 Raphael Tsu
Raphael Tsu Supervisory Committee

The City University of New York

ABSTRACT

The prominant features in the optical properties of semiconductors due to the long range order and hence are sensitive to disorder. In order to gain information about the nature of disorder in hydrogenated amorphous silicon (a-Si:H) and hydrogenated and fluorinated amorphous silicon (a-Si:F:H) the Raman scattering, optical and modulated optical (Electrolyte Electroreflectance, EER) spectra of (a) high temperature thermally annealed (HTA) a-Si:H(B), as well as unannealed a Si:H(B) and a Si.H(P), (b) heavily doped n-type a-Si:F:H with microcrystalline (μc) structure and (c) lightly doped a Si:F:H were studied. Comparison had been made with the optical features of crystalline silicon (c-Si). EER studies of ion-damaged, laser-annealed Si were also performed.

In the Raman spectra of (a) HTA-a-Si:H(B) and (b) a-Si:F:H alloys with μc-structure we have observed Raman frequencies intermediate between these of the amorphous phase (480 cm^{-1}) and the crystalline phase (522 cm^{-1}). The results for Si:F:H have been interpreted in terms of the μc structure and the related relaxation of the $\vec{q}$-vector restrictions. However, the structure for the HTA-a-Si:H are somewhat more complex since there is also a Fano-shift due to the high doping level.

For the modulated optical spectra we have obtained energy features at 3.4 eV and 4.5 eV (which are related to the optical transitions for c-Si) in HTA-a-Si:H, heavily doped n-type Si:F:H alloys (μc structure) as well as ion-demaged, laser-annealed Si. The EER spectra of HTA-a-Si:H showed features very similar to the ion-damaged, laser-annealed Si. No EER spectra was observed in unannealed Si:H(B) and lightly doped n-type Si:F:H specimens.

The reflectivity and the imaginary part of the dielectric function, $\epsilon_2(\omega)$, of (a) high temperature annealed, as well as unannealed, a-Si:H(B) and (b) n-type Si:F:H alloys with uc structure have been investigated in the energy range 1 - 10 eV. Unannealed Si:H(B) showed the featureless single bump spectra which is characteristics of amorphous Si. However, we have found that the HTA-a Si:H(B) and highly doped n-type Si:F:H samples exhibited well-defined structures associated with those of c-Si. The electron number per single Si-atom contributing the optical transition is calculated from a Kramers-Kronig analysis.

ACKNOWLEDGMENTS

I wish to express my deepest gratitude to my thesis advisor, Professor Fred H. Pollak, without his valuable guidance, patience and understandings throughout my graduate work, this dissertation would not have been possible. I would also like to express my thanks to Dr. Raphael Tsu of Energy Conversion Devices, Inc. for supplying the samples for this investigation, many helpful discussions and his constant encouragement.

I like to acknowiidge with deep appreciation the advice and guidance given to me by Professors Josph Krieger and George Skorinko of Brooklyn College of CUNY and Professor Frederick W. Smith of City College of CUNY, for his careful reading of this manuscript.

There are many whom I would like to express my appreciations, in particular, I want to mention Professor M. K. Liou, as well as Drs. Robert Silberstein, Joe Lyden, Peter Bratin, Paul Amirtharaj Won-Sing Pong and Ying-Sheng Huang.

Finally, I am grateful to my wife, Shu-Jen; my son, I-Chien; and my mother for their love, encouragement and understandings, to whom this thesis is dedicated.

I also want to knowledge with deep gratitude, the financial support throughout these three years from the Research Foundation of the City University of New York.

TABLE OF CONTENTS

LIST OF TABLES

LIST OF FIGURES

LIST OF FIGURES (continued)

LIST OF FIGURES (continued)

LIST OF PUBLICATIONS

R.Tsu, S.S.Chao, M.Izu, S.R.Ovshinsky, G.J.Jan and F.H.Pollak, "Electronic and vibrational properties of glow-discharge amorphous Si:F:H", Proc. 15th Int. Conf. Physics of semiconductors, Kyoto 1980; J. Phys. Soc. Japan, 49 Suppl. A, 1249 (1980).

R.Tsu, S.S.Chao, M.Izu, S.R.Ovshinsky, G.J.Jan and F.H,Pollak, "The nature of intermediate range order in Si:F:H(P) alloy system", Proc. 9th Int. Conf. of Amorphous and Liquid Semiconductor, Grenoble, 1981; Journal de Physique 42, C4-269 (1981).

G.J.Jan, F.H.Pollak and R.Tsu, "Optical properties of disordered silicon in the range 1-10 eV", to be published in Solar Energy Materals.

CHAPTER I INTRODUCTION

A crystalline semiconductor has a periodic atomic structure and hence exhibits a long range order (LRO). The macroscopic physical properties of such a material have been interpreted by the quantum theory of solids. This theory of solids was developed on the basis of the long range periodicity in order to simplify the calculation of physical quantities. Amorphous semiconductors, as opposed to crystalline materials, have an arrangement of atoms without periodicity. Without the symmetries resulting from periodicity, therefore, it is more difficult to calculate their physical properties using the one electron quantum theory of solids. Ioffe and Regel [1] have stated the empirical rule that amorphous materials will retain their semiconducting properties in spite of the destruction of long range order, — if the non-crystalline phase conserves the short range order present in the semiconducting crystal. Thus, it is of considerable importance to study this subject in order to understand the physical properties of amorphous semiconductors.

From the structural point of view a crystalline semiconductor is an ordered system whereas the amorphous semiconductor is a disordered one. Futhermore, since the theoretical understanding of disordered sys-

tems is still not well developed, it is important to study the physical properties of amorphous semiconductor from a fundamental point of view. Raman scattering is a sensitive tool to measure the vibrational states of semiconductors from order to disorder. Optical as well as modulated optical spectroscopies are sensitive probes to study the electronic states of semiconductors. Therefore, in order to gain information about the nature of disorder Raman scattering, optical and modulated optical experiment have been used to investigate specimens of disordered Si alloy (Si:H and Si:P:H) systems. Amorphous silicon was chosen because the crystalline (ordered) state of this material has been extensively studied and is quite well understood. Thus we can readily make a comparison of amorphous and crystalline properties. And also from the technological standpoint, amorphous silicon is a semiconductor of considerable current interest[2-4].

In amorphous silicon (a-Si), the continuous random network model[5] (CRN) has been widely accepted. An ideal CRN and a more realistic structure which includes extrinsic disorder due to structural defects (such as : dangling bonds, microvoid, etc.), have been studied[6] for many years. The structural defects depend heavily upon the methods and the conditions of preparation (such as vacuum evaporation or sputtering,

the pressure of the working chamber, the temperature of the substrate, introduction of hydrogen [7] and / or fluorine [8] , etc.).

One of the most important subjects in the development of semiconductor physics and electronic devices is doping [7] : adding a small concentration of impurities to crystalline silicon, thereby controlling the electrical conductivity. It has been shown [7] that the electronic properties of a-Si and amorphous germanium (a-Ge) prepared by plasma glow discharge decomposition (GDD) could be controlled over a remarkably wide range by substitutional doping introduced in the gas phase. Thin film specimens have been prepared by decomposing the mixture of silane gas (SiH_4) and (a) diborane (B_2H_6) for p-type doping, and (b) phosphine (PH_3) or arsine (AsH_3) for n-type doping. Since hydrogen is incorporated into the CRN, its presence can greatly influence the structural and electronic properties of the deposited material. The addition of hydrogen [9] to passivate the defects (terminate the dangling bonds) allows the a-Si film to be doped successfully. A hydrogenated amorphous silicon (a-Si:H) film prepated by plasma glow discharge decomposition of silane gas changes its properties dratically at temperature above 350 °C, due to the effusion of hydrogen [10-11] . Therefore, it is important to find a new

dangling bond terminator which does not effuse at such low temperatures. Fluorine (F) is such a candidate, because its binding energy with Si is higher than that of H by as much as 60%. Also there is evidence that the presence of F in a-Si will reduce the number of electronically active defect state (traps) in the gap[8,12].

Ovshinsky[12] and Madan et al.[13] have found a new a-Si material which contains both hydrogen and fluorine. This hydrogenated and fluorinated amorphous silicon (a-Si:F:H) film is prepared by plasma glow discharge decomposition of silicon tetrafluorine (SiF_4) gas mixed with H_2. The a-Si:F:H film has silicon and fluorine as its major structural components. This new alloy has overcome a number of proboems[12] associated with a-Si and a-Si:H. Other types of a-Si alloy materials such as purely fluorinated amorphous silicon (a-Si:F) have also been studied by Matsumura et al.[14-16]. It has been demonstrated by Matsumura et al.[17] that the conductivity can be controlled by doping with boron or phosphorus. They have investigated the structure of a-Si:F with transmission electron microscope (TEM), infrared absorption (IR), Rutherford backscattering measurements and structural changes in this material due to chemical etching. Their results suggested that a-Si:F alloy consists of many pure a-Si grains of about 40 Å in size, and that the enlargement of the grain size is

a key factor to improve the properties of a-Si:F such as photoconductivity. They have also examined Si:F vibrations in a-Si:F and a-Si:F:H alloys[12,18-21] . It is important to futher study the nature of the bonding in this new alloy which appears to differ from the bonding of the other a-Si compounds.

Within the past two years several groups[17,22-26] have reported the observation of the microcrystalline (μc) phase in thin films of the Si:H and Si:F:H alloy systems. They have prepared their samples under various conditions. The particle size of the μc-Si "particle" are 20 Å - 100 Å. The preparation of thin films of microcrystalline Si(μc-Si) and Ge (μc-Ge) via chemical transport in a hydrogen plasma was reported in 1968 by Veprěk and Maršcek[17] , and μc-Si alloys have also been produced by deposition from silane diluted to a few mole % by hydrogen in a discharge operating at a high power level[22] . During the past years, μc-Si has received considerable attention because of its possible application such as contact interlayers in solar cell [23-25]. It has been found that during the deposition of silicon from Si/H, in a low pressure discharge plasma, the decisive parameter controlling the formation of either an amorphous or crystalline phase is the departure of the system from chemical equilibrium. In the case of fluorinated a-Si, the presence of high concentration

of P- or As-doping, results in μc-structure[26] .

It is of considerable interest to investigate the electronic and vibrational properties of (a) high temperature annealed Si:H(B) as well as unannealed a-Si:H(B) and a-Si:H(P), (b) highly doped a-Si:F:H with microcrystalline structure, (c) lightly doped a-Si:F:H alloy systems. In order to obtain information about the vibrational states of specimens, we have investigated these modes using Raman scattering spectroscopy. Optical and modulated optical spectroscopies are two of the several sensitive tools used to study the evolution of the electronic states from order to disorder of silicon alloys. In order to understand the electronic properties of a-Si, μc-Si and c-Si alloy systems we have measured the optical reflectance and EER spectra of these specimens.

The first order Raman active spectrum provides a fast and convenient method of determining whether a silicon film is crystalline, microcrystalline or amorphous. Because the interaction requires the conservation of momentum in c-Si, the first order Raman active mode involves only the zone center ($\vec{q}$=0) optical phonon at ω= 522 cm^{-1} which gives rise to a single spectral line with a full width at half maximun (FWHM) of about 4 cm^{-1} at room temperature. But in a-Si the phonon momentum is not a good quantum number due to the

lack of translational symmetry. Therefore, this Raman spectra exhibits broad peaks, the most prominent one being around 480 cm^{-1} which reflects the phonon density of states of the transverse optical (TO) modes at the zone boundary. It has been shown by Iqbal et al.[13] that polycrystalline films with a measured grain size of the order of 100 Å have Raman frequencies of 520 cm^{-1} and a linewidth ~ 7 cm^{-1} . We have observed a microcrystalline phase of silicon in heavy As- or p-doped alloy[26-28] . Tanaka et al.[29] also reported observing a μc-phase in highly P-doped Si:F:H alloy. Hamasaki et al.[30] have produced crystallization in P-doped a-Si:H by applying high radio frequency (RF) power during the crystal formation process. It is important to point out that the occurance of μc-Si is desirable for solar cell contacts[27-28] because of higher electrical conductivity and lower optical absorption.

We have also measured the first order Raman active spectra of high temperature annealed boron doped a-Si:H specimens. We found that Raman frequencies of these samples are around 517 cm^{-1} but that the Raman linewidth is narrower than the highly P- or As- doped a-Si:F:H alloys. Therefore, the high temperature annealing improves the crystalline structure of silicon. There are two known mechanisms which result in a down shift of the frequency of the zone center optical pho-

non : (a) finite particle size and (b) Fano shift due to the interaction of a continum, i.e. free carriers, with the phonons[31] . In the highly P- or As-doped a-Si:F:H samples that exhibited μc structure only a small fraction of the dopants are substitutional, and have the down shift is mainly due to finite size effects. However, for the high temperature annealed case, a higher fraction of the dopants are substitutional, the down shift of Raman frequency associated with c-Si is a Fano shift due to the high doping level[31] .

In order to understand the electronic states of Si:H and Si:F:H alloy we have utilized optical and modulated (electroreflectance) techniques. Since the optical properties are affected by the LRO of the material they are quite sensitive to disorder. The most useful modulation technique has proven[32] to be electroreflectance (ER) or electroabsorption (EA). Both of these methods provide the sharpest structures since they are related to the third-order derivative of the unperturbed optical dielectric functions[32-35] . Okamoto et al.[36] have reported energy features in the electroreflectance spectra of a-Si:H near the fundamental optical edge (1.8 eV). Freeman et al.[37] have also reported ER spectra possessing only one distinct peak (1.8 eV) in sputtered a-Si:H. Nonomura et al.[38] have studied the ER spectra of a-Si:H which is made by RF

plasma deposition from silane (SiH_4) diluted with hydrogen to 10 %. The energy feature of ER spectra at 2 eV. The energy features above 2 eV in EER spectra were first found by Tsu et al.[27]. These features above 2 eV (i.e. 3.4 eV and 4.5 eV) in the EER spectra of heavily P- or As-doped Si:F:H alloys are associated with the crystallinity of Si. We will show how the optical and modulated optical properties of semiconductors are sensitive to the degree of crystallinity.

We have characterized several Si:H and Si:F.H alloy systems using the EER modulation technique. We have seen the 3.4 eV and 4.5 eV energy features, which can be associated with optical structure of c-Si[34-35] , in the EER spectra for (a) heavily P- or As-doped Si:F:H alloys with μc structure and (b) high temperature thermally annealed boron doped Si:H alloys. All of these samples also exhibited a down shift of Raman frequency from the 522 cm^{-1} peak of c-Si. Therefore we conclude that these peaks at 3.4 eV and 4.5 eV originate from the crystalline-like structure of these alloy systems. We have also measured the EER spectra for an ion-damaged silicon wafer that has been laser-annealed with different power densities. We found that the EER spectra of thermally annealed Si:H(B) are very similar to the spectra of the ion-damaged, laser-annealed Si samples.

In order to gain more information about the electronic properties of these HTA-a-Si:H(B) and uc-Si:F:H materials we measured the reflectivity of these sample using a very high precision rotating light-pipe reflectometer (RLPR)[39-41] . The complex dielectric function of a solid is related to its electronic band structure. One method of determining the dielectric function consists of measuring the reflectance at near normal incidence over a sufficiently large range of photon energies and using a Kramers-Kronig (K.K.) analysis. Two optical constants n and k (or $\epsilon_1(\omega)$ and $\epsilon_2(\omega)$) can be determined from the K.K. analysis. The imaginary part of the dielectric function $\epsilon_2(\omega)$ is sensitive to structural order.

We have carried out the measurement of the reflectance spectra for several As- or P-doped Si:F:H alloys and the thermally annealed, B-doped Si:H alloys. The results of reflectance spectra and imaginary part of dielectric function for all measured specimens showed that the samples of heavily P- or As-doped Si:F:H alloy have formed a μc structure of Si and the sample of thermally annealed B-doped Si-:H alloys showed a high degree of crystallinity (large μc structure). The thermal annealing improves the degree of crystalliinity. The unannealed a-Si:H(B) shows a single bump for $\epsilon_2(\omega)$, characteristic of a-Si.

The change of the short range order has a shift the joint density of states. It should also alter the optical transition matrix elements. Most likely these changes are responsible for the large variation of the height of the $\epsilon_2(\omega)$ peak. We applied the sum rule to the $\epsilon_2(\omega)$ spectra to calculate the effective number n (E) of electrons per Si atom which have been exicted at given energy E. The expression for the sum rule is written in the following formula:

$$n_{eff}(E) = \frac{m}{2\hbar^2\pi^2e^2N}\int_0^E E'\epsilon_2(E')dE'$$

where m is the rest mass of electron, e is the charge of electron and N is the density of Si crystal.

The major differences and similarities in the structure of amorphous and crystalline Si are dicussed in chapter II. We were interested in some of the electronic and vibrational properties of a-Si alloys. Therefore, we described some of the problems and new development of a-Si semiconductors in recent years. The last section of this chapter is concerned with major aspects of electronic and vibrational states in the presence of microcrystalline structure of silicon. We also included a description of properties of electronic conduction of a-Si semiconductors in this chapter.

In chapter III, section 1 give the characteris-

tics we describe the sample prepartion method and of the specimen. A general description of the theory of Raman scattering is given in section 2. The experimental setup and details about Raman scattering spectroscopy, results and interpretation are also given in this section. Section 3 gives a general description of electroreflectance (EER) theory, the EER experimental set up, the EER experimental results and data interpretation. Optical reflectance studies including theory, experimental technique, results and data interpretation are described in the last section of chapter III.

In chapter IV we summarize all of the results of the optical, modulated optical and Raman scattering studies. We discuss all of the results which have been obtained by these three experimental techniques. The conclusions of this investigation are also given in chapter IV.

CHAPTER II AMORPHOUS SILICON SEMICONDUCTORS

During the last few years interest in the fundamental and applied aspects of amorphous semiconductors has grown rapidly. This chapter is a brief synopsis of the consenus of thought on the nature of the salient properties of amorphous silicon (a-Si) semiconductors. We give a brief historical survey of the work and the present interest in the a-Si semiconductors. We would especially like to concentrate on the description of the recent experimental results and explanations in microcrystalline silicon (μc-Si) alloys. Theoretical considerations and important background information on a-Si and μc-Si alloy systems, especially their electronic, and vibrational properties are presented.

A crystal is defined as a substance consisting of atoms arranged in a pattern that repeats periodically in three dimensions. Amorphous semiconductors in general do not have a definite arrangement aof periodic structure. Howover there is a definite short range order(SRO). The short range order is characterized by the nearest neighbor atoms.

In crystalline material the electronic states can be described by Bloch functions. Because amorphous semiconductors lack a periodic structure the electron states cannot be described by Bloch states. It is difficult to calculate the electronic states of amorphous

solids from first principle because of the lack of crystalline periodicity. However, for those amorphous materials with the same short-range order as in a corresponding crystal, the one electron density of states of the former can be estimated from the latter by the introduction of a non-k-conserving perturbation. This perturbation destroys both the validity of k as a good quantum number and the concepts of a Brillouin zone. In addition, it removes the Van Hove singularities from the density of states and, most important of all, it renders Bloch's theorem invalid.

Application of a non-k-conserving perturbation to the periodic potential of a crystalline semiconductor clearly will shift states from the valence and conduction bands into the forbidden gap, thus creating band tails. There have also been many theoretical studies of the electronic structure of a-Si and a-Ge, including a study of the band structure of the normal crystalline phase under the influence of specific kinds of disorder. Some of the investigators, Ziman[42], Kramer and Treusch[43], Cohen et al.[44] and Joannopoulos et al.[45] were among the first attempting to theoretically calculate the density of states. Later on, Singh[46], Tanaka and Tsu[47] have determined the various kinds of specific disorder on the band structure of Si. They considered small distortions, including extensions and contrac-

tions of bond lengths, various bond angle changes, and dihedral angle variations from the normal crystalline phase of Si. The model which they used was a realistic tight-binding Hamiltonian including third nearest neighbor interactions decribing the electronic states of amorphous Si. A number of models such as the structural, compositional, cellular, quantitative, and topological have been investigated. The model of purely topological disorder, as represented by the Hamiltonian used by Weaire and Thorpe[48-50] results in a description of the behavior of bands and band gaps in tetrahedrally bonded semiconductor silicon. A Hamiltonian representing pure compositional disorder that is suggested by Anderson[51] provides the key for the understanding of electron localization in a disordered system. These idealized models are used as a skeletal basis for understanding the electronic properties of a-Si semiconductors.

Ioffe and Regel[1] have stated the empirical rule that amorphous semiconductors retains its semiconducting properties in spite of the destruction of the LRO if the non-crystalline phase conserves the SRO present in the related semiconducting crystal. The short range order was characterized by the number of atoms in, and the radius of, the first coordination sphere.

The most generally accepted structural model for

a-Si is the continuous random network (CRN) due to Polk [5] . A schematic of CRN model is shown in Fig.(2.1)[52] . According to this model, a-Si consists of an infinite, non-periodic three dimensional array of interlinked atoms. The SRO about each atom results from the same chemical bond as in c-Si. The structure of this covalently-bonded a-Si has the following principal features: (1) each atom has equal coordination; (2) bond angle deviation is allowed ; (3) there are no dangling bonds; (4) the bond angle is minimized. The random character of the network results from a statistical distribution of dihedral angle and bond angle. The dihedral angle is the relative orientation of triads of bonds emanating from two nearest neighbors and has been discussed by Mott and Davis [53] . The CRN model represents an ideal structure for a-Si which is free of voids, impurities, dangling bonds, and other defects.

It is of considerably importance to understand the gap states in a-Si. In crystalline materials each electron can be described by a Bloch wave function. Mott and Davis [53] have shown, however that it is not necessary to use this particular function although the Schrodinger solution must exist. Therefore, a common concept which can be carried over from c-Si to a-Si is the density of states (DOS). The DOS can be determined experimentally by soft x-ray emission and absorp-

tion, x-ray photo-electron emission, UV spectroscopy[54-58] etc. Generally speaking, the DOS in a-Si does not differ greatly from that of c-Si except that the fine features may be smeared out[59], and some localized states may appear in the energy gap in a-Si. One of the effects of disorder on the electron states in the gap of amorphous semiconductors was given by Gubanov[60], who suggested that the conduction and valence band edges tailed into the gap and that in the tails the states were localized in space. Later, Cohen et al.[61] introduced the Cohen-Fritzsche-Ovshinsky (CFO) model in which the tails were considered to be sufficiently extended that they overlapped near the center of the gap. They assumed that the tail states extend across the gap in a structureless distribution. This general gradual decrease in the number of localized states destroys the sharpness of the conduction and valence band edges. The overlap of the cnduction and valence band tails leads to an appreciable DOS in the middle of the gap. One consequence of the band overlap is that there are states in the valence band, ordinarily filled, which have higher energies than states in the conduction band that are ordinarily unfilled. A redistribution of the electrons must take place, forming filled states in the conduction band tail which are negatively charged, and empty states in the valence band which are

positively charged. Thus, self-compensation pins the Fermi level close to the middle of the gap. However, one of the major objections against the CFO model had to do with the observed high transparency of the amorphous chalcogenides below a well-defined absorption edge. Therefore Davis and Mott[53] proposed that tails of localized states should be rather narrow and should extend only a few tenths of an electron volt into the forbidden gap. They also suggested the existence of a band of compensated levels near the middle of the gap, originating from defects in the random network, such as voids, vacancies, and dangling bonds. This model is called the Davis-Mott model[53]. The band at mid-gap may be split into donor states and acceptor states, which would also pin the Fermi level. This is called the modified Davis-Mott model . The density of states is illustrated for the CFO model in Fig.(2.2a), for the Davis-Mott model in Fig.(2.2b), and for the modified Davis-Mott model in Fig.(2.2c). Fig.(2.2d) illustrate the DOS for a real glass with defects. In each of the figures, the states are localized for $E_v < E < E_c$ and extened elsewhere. In Fig.(2.2b) for energies above E_c and below E_v the electron wave functions extend throughout the material so that these states, denoted by E, are extended states. The states between E_c and E_A (shown shaded in the figure) are localized states.

These marked T between E_c and E_A and between E_v and E_B are thought to arise because of the lack of LRO and are called tail states. The states denoted by D arise from defects in the material and the density of these depends critically on the method used to prepare the amorphous film. Mott[53] also suggested that at the transition from localized states to extended states the mobility should increase by several orders of magnitude, producing a mobility edge. The interval between the energies E_c and E_v acts as a pseudogap and is defined as the mobility gap. In recent years experimental evidence has shown[62] that various localized gap states exist which are located at well-defined energies in the gap. These states are associated with defects, the nature of which is not always known. For most of the amorphous semiconductors prepared by fast deposition from the vapor phase, there will be appreciable densities of different types of structural defects, some of which may be examined by electron spin resonance (ESR)[62].

The Dundee group[63] were stimulated by the new concepts and ideas that had been introduced by Mott and others and the initial aim of their work in 1968 was to provide some reasonably conclusive experimental tests of the proposed models and transport mechanisms. After investigating evaporated, sputtered and glow discharge

films of a-Si, they concluded at the early stage of the work that the plasma glow discharge decomposition technique was the most promising approach for their purpose. It led to material in which the basic properties of the amorphous phase were not obscured by the presence of high density of states. For this reason, since 1969, some of the investigators concentrated their efforts on the development of the plasma glow discharge decomposition method for the preparation of a-Si thin films.

The first electron drift mobility results on glow discharge a-Si were published by Spear and Le Comber[64] in 1970. From the temperature dependence of the drift mobility and conductivity they came to the conclusion that above about 250 ^{o}K electrons propagate in the extended states with mobility between 1 and 10 $cm^{2}V^{-1}$ Sec^{-1}. Below that temperature, phonon assisted hopping through localized states near the bottom of the band tail begins to predominate and eventually, with decreasing temperature, the conduction path moves towards the Fermi level. This interpretations, which supported some of Mott's basic ideas, appears to have stood the test of time.

Although band tails can have very significant effects on the electronic properties of amorphous semiconductors and the breakdown of the selection rule can

seriously modify the optical properties, the presence of disorder has much more profound consequence for transport. Since Bloch states in crystalline materials extend through the crystal, free carriers are scattered only by deviations from periodicity. In the absence of long range order, it is possible that valence and conduction electronic states are localized in the vicinity of a particular atom.

Cohen et at.[61] assumed the existence of band tails and mobility edges for amorphous silicon, thus yielding a finite density of states at the Fermi energy, $g(E)$. They also assumed that all atoms locally satisfied their chemical valence requirements, thus precluding the existance of sharp bumps within the mobility gap, as occurs in doped crystalline semiconductions Their model provides a useful structure for the analysis of transport and optical date.

Extensive band tails should be an evident in ordinary optical absorption experiments. In crystalline semiconductors, the material is essentially transparent to light of frequency below that of energy gap, and optical-absorption coefficients rapidly increase with photon frequencies above the gap. It might be expected that if there exist band tail states, the optical-absorption coefficient should begin to increase with photon frequencies well below the mobility gap, and

this increase should not be as sharp as in the case of the corresponding crystalline semiconductor gap.

Experimental information on gap state distribution was evidently of considerable importance. Spear et al.[65] developed a field effect technique for this purpose. They carried out a fairly detailed study of the optical and photoconductive properties of glow discharge a-Si. The most striking feature brought out by the early field effect work was the remarkly low overall density of states that could be achieved in glow discharge a-Si deposited at substrate temperature around 250 ^{o}C. Density of states g(E) in the center of the gap appeared to be at least two orders of magnitude lower than in evaporated or sputtered a-Si. The failure of doping on these materials is due to a large density of states in the energy gap. In 1975 Le Comber and Spear[63-65] showed the electronic properties of a-Si could be controlled by substitutional doping in a systematic way over a remarkably wide range. The possibility of substitutional doping has removed one of the main limitations and opened up an exciting new field for fundamental and applied developments. The information on the nature and structure of the defects in tetrahedrally coordinated amorphous materials obtained by Brodsky and his colleageus[62] , Paul's group[66], Stuke and his collaborators[67] . Brodsky et al.[64] had suggested that

one of the reasons for the promising properties of glow discharge a-Si might be the incorporation of hydrogen which serves to saturate danging bonds during growth. The most important development in this direction was reported by the work of Lewis et al.[68] at Harvard in 1974 on influence of the hydrogen atom of sputtered a-Ge films. In 1976 Paul and his colleagues were able to show[69] that the addition of hydrogen to the Argon sputtering gas has a drastic effect on the electronic properties of the sputtered a-Si thin films. The hydrogenated amorphous silicon (a-Si:H) materials can now be doped with reasonable efficiency by the addition of phosphine, arsine or diborane and this result has contributed to the present applied interest in a-Si semiconductors. The role of hydrogen in amorphous semiconductors has stimulated a great deal of experimental work. Various methods of incorporating hydrogen in a-Si have been examined.

It is pertinent at this point of our discussion to present a short account of deposition techniques. Essentially five techniques have been used to date, such as (a) plasma glow discharge deposition, (b) RF sputtering, (c) ion implantation, (d) thermal diffusion hydrogenated process and (e) chemical vapor deposition (CVD) for the preparation of doped a-Si semiconductors. However, the glow discharge technique has received a

considerable amount of attention in recent years since it was used in the first successful doping experiments on a-Si and a-Ge by Spear and Le Comber[65] in 1975. Thin film specimens of a-Si or a-Ge were formed by decomposing the corresponding hydrides silane (SiH_4) or germane (GeH_4) in a radio frequency field, The power level is small, typically a few watts, and frequencies between 1 and 100 MHz have been tried. The electronic properties of deposited specimens are critically dependent on a number of varriables such as the temperature of the substrate during deposition, flow rates and partial pressure of mixed gases, power level of RF, the bias on specimens and other surfaces, doping type and level, etc. Doping from the gas phase can be achieved by adding phosphine (PH_3) or diborane (B_2H_6) to the silane. The room temperature conductivity of a-Si prepared in this way is shown in Fig.(2.3) as a function of gas composition[65]. On the right-hand side this is the ratio of the number of phosphine to the number of silane molecules in the gas mixture, whereas on the left the corresponding diborane to silane ratio is shown. In the center of the graph, the conductivities of 10^{-8} to $10^{-19}\Omega^{-1}\,cm^{-1}$ are representative of undoped glow discharge specimens. The results demonstrate clearly that σ_{RT} can be controlled over some ten oredrs of magnitude, from 10^{-12} to $10^{-2}\Omega^{-1}cm^{-1}$, with both n- and

p-type doping, as the Fermi level is moved over approximately 1.2 eV.

In this paragraph we summarize the electronic coductivity is described by the electron transport theory of solids. The electron density, n(E), at a particular energy can be expressed[53] in terms of the density of states, g(E), at that energy and the Fermi-Dirac distribution function, f(E)

$$n(E) = g(E)f(E) \text{ ----------(2.1)}$$

and

$$f(E) = \left[1 + \exp(E-E_F)/K_BT\right]^{-1} \text{ --(2.2)}$$

in which E_F is the Fermi energy. If the kinetic energies of electron is restricted to be more than a few K_BT away from E_F ,then we can used Boltzmann distribution function to describe the occupancy of states, so that n(E) becomes

$$n(E) = g(E)\exp\left[-(E-E_F)/K_BT\right] \text{ ---(2.3)}$$

In a material with mobilities of the order 1-10 cm^{-2} /VSec, the mean free path becomes comparable with lattice constant — the Boltzmann equation is no longer suited to described the transport proeprties of the electron. The concept of Anderson localization has often played a key role in the interpretation of transport phenomena for amorphous semiconductors. The

valence and conduction bands are considered to have the schematic form shown in Fig.(2.2), with mobility edges separating extended and localized states, the latter making no contribution to the conductivity σ at $T=0^{o}K$. The localization of elections by disorder has been studied by Arderson[51]. However, the general expression for the conductivity[53] is the Kubo-Greenwood formula, from which the Boltzmann equation can be derived in the limit of long mean free path. When the states involved in the conductivity are several K_BT above the Fermi energy, the Kubo-Greenwood formula takes the form

$$\sigma = \int e\mu(E)n(E)dE \text{ ----------(2.4)}$$

where $\mu(E)$ is the mobility gap. The contribution to the conductivity from the electron at any particular energy is given by:

$$\sigma(E) = e\mu(E)n(E) \text{ ----------(2.5)}$$

$$\sigma(E) = e\mu(E)g(E)\exp[-(E-E_F)/K_BT] \text{ ----(2.6)}$$

A similar expression can be written for the hole contribution. We shall restrict the discussion to electron case. In a pure crystal, $g(E)$ is zero within the energy gap so that $\sigma(E)$ will also be zero in this energy. In the amorphous case $g(E)$ is finite throughout the whole energy range so that we can expect contributions to the conductivity from each of these energies. From

Eq.(2.6) it is clear that the details of the mobility in the various energy ranges is as important as the density of states and the occupancy of those states in determining the magnitude of conductivity.

The transport properties of amorphous semiconductors are dominated by carries within K_BT of the energy at the mobility gap. Thus, the localized states in the band tails near the mobility gap and trapping from the deeper states present a substantial influence to electronic conduction process in amorphous semiconductors.

Near the mobility edge, the conventional expression for semiconduction transport may still be applicable, i.e.

$$\sigma = N_c e \mu_e \exp[-(E_c'-E_F)/K_BT] + N_v e \mu_h \exp[-(E_F'-E_v')/K_BT] \quad \text{----------(2.7)}$$

where Nc and Nv are the effective densities of states in the conduction and valence bands, μ_e and μ_h are the electron and hole mobilities beyond the mobility edges, and E_c' and E_v' are the positions of the conduction and valence band mobilty edges, respectively. Eq.(2.7) would yield a $\log\sigma$ vs. T^{-1} plot that is either a single straight line or two intersecting straight lines. On the other hand, a diffuse mobility edge should yield a concave upward curve on a plot of $\log\sigma$ vs. T^{-1}, reflecting the fact that at lower temperature the con-

ductivity is dominated by relatively low mobility carriers much closer to the Fermi energy.

If the suggestion of Cohen et al.[61] that a finite $g(E_F)$ exists is correct, the Fermi energy would then appear to be pinned in the sense that conductivity would be quite insensitive to substitution doping or to the injection of excess carriers. In addition, the redistribution of electrons which should leave relatively high-energy valence-band states above E_F should create relatively large densities of unpaired electron spins these would be expected to be observable in electron spin resonance (ESR) experiments and a Curie term in the magnetic susceptibility.

Mott[70] has pointed out that for a sufficiently large $g(E_F)$, phonon-assisted hopping among localized states near E_F might well predominates band-like contribution beyond the mobility edges at sufficient low temperatures. He further suggested that at very low temperatures, when very few energtic phonons are present, such hopping conduction would involve hopping beyond nearest neighbors. Mott showed that for this mechanism of v the
conductivity varies as

$$\sigma = \sigma_o \exp[-(T_o/T)^{1/4}] \quad \text{----------(2.8)}$$

where σ_o and T_o are constants. When Eq(2.8) is valid,

a $\log\sigma$ vs. T^{-1} plot is concave upward, but a $\log\sigma$ vs. $T^{-1/4}$ plot should be linear.

The possibility of variable-range hopping actually somewhat muddles the test for the existance of sharp mobility edges. A linear plot of $\log\sigma$ vs. T^{-1} could indicate either band-like conduction beyond a sharp mobility edge or phonon-assisted localized states. Alternatively, a concave upward log vs. T^{-1} plot could reflect either the absence of a sharp mobility edge or the predominance of variable-range hopping conduction.

Measurements of field effect and electron spin resonance (ESR) have given some evidence[6] for the presence of unsaturated dangling bonds. However, it has recently been noted that the ESR signal may also have contribution from defect states in the case of a-Si films prepared by ion-damaged c-Si or by sputtering deposition. Many properties of a-Si are not intrinsic to the material, but are due to structural defects, because many defect states exist inside the gap. For this reason one could not control the electrical properties of a-Si by doping with impurities. First of all we need to reduce the large numbers of defects which arise during the film preparation. Fortunately Spear et al.[64,65] have found that a-Si films prepared by the decomposition of silane gas using a glow discharge plasma had reduced the densities of dangling

bonds to undetectable levels ($< 10^{16}/cm^3$). For these films we can proceed to change the electrical properties by controlling the concentration of extrinsic dopants.

Controlling the extrinsic dopants changes the optical as well as electrical properties of a-Si films. For example, photoluminescence, AC conductivity and ESR are affected. In GDD-a-Si:H films no ESR signal has been observed and normal activated DC conduction is found. Similar properties have been observed in materials which are prepared by sputtering in an Ar/H atmosphere. The main effects of the hydrogen incorporated into the film is to saturate most of the dangling bonds. Street et al.[71] have demonstrated that in undoped a-Si:H specimens prepared under varying deposition conditions, the photoluminescence intensity is correlated with the spin density. It has been deduced that non-radiative recombination occurs by tunneling to defect states with nonzero spin. Bombardment of a-Si:H samples by either high energy electrons or He ions introduces structural defects that quench the band edge luminescence. Annealing of bombarded a-Si films removes the structural defects , as shown by the reduced ESR signal and enhanced luminescence intensity. Generally amorphous semiconductors will exhibit, in a certain frequency range, AC conductivity which is dependent on

frequency ω and is given approximately by $\sigma_{AC} = A\omega^s$, where $s<1$[53].

Recently a new type of amorphous alloy based on a-Si:F:H has been produced by Ovshinsky et al.[8,12] This new a-Si:F:H alloy is highly photoconductive and possesses a rather low DOS in the upper half of the band gap compared with a-Si:H. Madan et al. have shown that for a gas ratio (SiF :H) < 10 the resuting alloy has a low DOS and exhibits high conductivity. They also found that, as the ratio of SiF to H decreases down to 10, the predominant transport mechanism changes from a variable-range hopping type conduction to a well-defined activated process mechanism. In their new a-Si:F:H materials the DOS g(E) decreases rapidly with decreasing gas ratio. The peak in g(E) which is observed in the a-Si:F:H alloy is absent in these new a-Si:F:H alloys. The DOS for this new material in the upper half of the band gap is lower than in a-Si:H. Amorphous semiconductors ordinarily have a very large density of localized states which act as traps, leading to low values for the drift mobility and low recombination times for the free carries. Spear and Le Comber[65] have reported that a-Si:H films produced from silane gas by RF glow discharge and deposited on a heated substrate have a much reduced DOS; at the Fermi level it is only $\sim 10^{17}$ $cm^{-3}eV^{-1}$. Because of the low DOS, a-

Si:H films can be fabricated successfully, and n- or p-type semiconductors doped with phosphorus (or arsenic) or boron, respectively, have been succeedfully produced.

During the last two years, a microcrystalline (μc) phase of Si (particle size ~20 Å - 60 Å) has been found in Si:F:H alloys[26-28] . The possibility of controllable μc deposition is of great interest from both a basic and applied point of view. It would permit an extension of fundamental studies of electronic properties of semiconductors just beyond the amorphous phase as a function of structural ordering. It also has considerable applied interest because of possible application of μc-Si as contact interlayers in solar cell. The preparation of μc-Si thin films via chemical transport (CT) in a hydrogen plasma was reported in 1968 by Veprek and Mareck[22] . Recently μc-Si has been produced by deposition from silane diluted to a few mole % by hydrogen gas in a glow discharge operating at high RF power level. It is also known that the presence of a high concentration of dopants, such as phosphorus and arsenic, can cause crystallization due to a catalytic effect on the formation of nuclei with the diamond lattice. Veprek and Mareck have investigated the a-Si and μc-Si alloys produced in a SiH_4 discharge plasma under a variety of conditions. The low limit for the crystal-

lite size is 30 Å for stress- free μc-Si .

Spear et al.[64] have investigated the electronic properties of GDD-uc-Si films by conductivity, Hall effect, and field effect measurements as a function of crystallite size and phosphorus doping ratio. Normally the Hall coefficient of a-Si films has an anomalous sign (i.e. positive in n-type a-Si films and negative in p-type films) . But the Hall coefficient in GDD-μc-Si is negative in n-type materials, which would be expected in c-Si. They found that the sign of the Hall coefficient behaved normally down to a crystallite size of about 20 Å. They also suggested that the large increase in conductivity over that in a-Si was almost entirely caused by an increased carrier density resulting from delocalized electron tail states. The information that limit for the crystallite size of the ordered regions in this material is around 20 Å .

Richter et al.[59] have used electron photoemission spectroscopy (EPS) to study the transition from a-Si to μc-Si. Their Si:H films were prepared by chemical transport in a hydrogen plasma or by sputtering in a H /Ar gas mixture. Their investigation showed that the first order Raman active spectra were a superposition of the spectra for the a-Si and c-Si phases. Uchida et al.[72] also investigated the electronic and optical properties of p-doped GDD-μc-Si films for a variety of

deposition conditions. They found that the electrical conductivity of films increased from 2 x $10^{-12}(\Omega\text{-cm})^{-1}$ to 8 $(\Omega\text{-cm})^{-1}$ as the discharge power during deposition was increased. The GDD-μc-Si films changed correspondingly in structure from the a-Si phase into a c-Si phase with increasing conductivity. Even very thin (100 Å) p-doped Si:H films could still have a microcrystalline structure. Tsu et al.[28] also observed a microcrystalline structure of Si in heavily doped n-type (P or As) a-Si:F:H alloys. Because of the lower absorption coefficient at short wavelengths and the higher conductivity, this p-doped μc-Si film shows promise as a good material for the contact layer in solar cells.

First order Raman scattering provides a convenient tool for determining whether a silicon film is crystalline, μc or amorphous. The a-Si film exhibits a broad feature at~480 cm^{-1} (width ~80 cm^{-1}) which associated with the density of states of phonon at the zone boundaries. The c-Si exhibits a single sharp line of Raman feature at 522 cm^{-1} (linewidth ~4 cm^{-1}) which associated to optical phonons at the zone center. In μc-Si films prepared by chemical transport or by laser annealing of a-Si, the sharp line at 522 cm^{-1} is broaded and shifts to lower with decreasing crystallite size. These effects can be explained by finite particle size[28]. In an "infinitely large" crystal of Si,

the first order Raman active spectrum is due to the symmetry allowed optical phonon at $\vec{q} \approx 0$. The optical modes for a finite crystal will be lower in frequency than those for an "infinite" crystal. In a-phase materials the $\vec{q}$ selection rule breaks down. The first order Raman intensity consists of phonon modes of the entire optical and acoustical branches, since $\vec{q}$ is no longer conserved. Raman spectrum exhibits a broad spectral feature at $\sim$480 cm^{-1} of which is due to the amorphous component, and the sharp Raman spectral feature at $\sim$522 cm^{-1} is due to the crystalline component. In μc-Si, Raman spectrum presents a down shift of Raman frequency associated with c-Si and broadening Raman linewidth due to finite size effect. It would be even more interesting the fundamental physical proeprties of the a-Si:F:H alloy, this material shows improvement in many of problem areas of a-Si:H.

The electronic states of semiconductors can be studied by optical and modulated optical spectroscopies. Optical reflectance spectroscopy provides information from the long range order (crystalline state) to short range order (amorphous states). The imaginary part $\epsilon_2(\omega)$ of the dielectric function can be obtained from the optical reflectance spectra using Kramers-Kronig analysis. The $\epsilon_2(\omega)$ function can be related to optical transitions. Modulated perturbation gives rise

to sharp, differential-like spectrum of the optical features in the energy regions, where optical excitation process occur. The detailed general description of optical and modulated optical spectroscopies will given in Chapter III.

CHAPTER III EXPERIMENTS

In this chapter we describe the different optical experiments which include Raman scattering spectroscopy, oPtical and modulated optical measurements used in this investigation. The chapter is divided into four main sections.

In Sec. 3.1 we describe the method and procedures used in the preparation of a-Si.F:H alloys which we have studied. In Sec. 3.2 we discuss the appropriate theory, techniques and results of Raman scattering measurements. Similarly, in Sec.3.3 and 3.4 we discuss theory, techniques and results of electrolyte electroreflectance and optical reflectivity experiments respectively.

3.1 CHARACTERISTICS OF SAMPLES

The plasma glow discharge decomposition technique for preparing the a-Si:H alloy has proven to be a very good process to prepare specimens exhibiting a marked reduction of structural defects. There are two different types of reactors[73] : the capacitor type and the inductor type. The inductor glow discharge decomposition system was used by Chittick[74] et al. in 1969. In this type system the plasma glow discharge is powered by an external RF coil. Frequencies in the range 0.5 to 13.5 MHz are used. This type of glow discharge system

has two distinct advantages, it provides a uniform a-Si:H films over a large area, and it has a fast deposition rate. However, the most popular technique for depositing a-Si:H is that ultilizing an RF capacitive discharge system with the substrate located on one of the electrodes. Generally a negative bias of 100 - 300 V is applied with a RF of 13.56 MHz. Biasing the substrate negatively appears to reduce defect densities at high RF powers. This also has the capability of producing a uniform a-Si alloy over large areas. In some electrodeless discharge systems the RF power is supplied by external capacitor plate. Flowing silane (SiH_4) in a DC cathodic plasma glow discharge is used to produce a relatively uniform thin film of a-Si:H alloy.

Most of the samples in this work were prepared at Energy Conversion Devices (ECD) Inc. in Michigan. Most of the a-Si:F:H samples studied were made by the capacitive discharge method using an RF power of 30 watt to decompose a gas mixtire of SiF_4:H_2 of 5:1. Normally the sample substrate electrode was biased at approximately -100 V. A gas flow rate around 0.05 liter/min at 0.5 torr was normally used. The n-type doping in the sample was accomplished by the introduction of PH_3 or AsH_3 gas. The specimens of B-doped alloy were prepared using a mixture of SiH_4:H_2 and B_2H_6 gas. The temperature of the substrate was maintained at $\sim$ 300 °C during the

deposition of the thin film. The substrates used were 7059 Corning glass, Quartz, c-Si as well as stainless steel. Some glass substrates were coated with a SnO_2 film to give a good electrical contact. The high temperature thermally annealed a-Si:H(B) samples were annealed about 10 min. at different annealing temperatures. Many films of a-Si:F:H of varying thickness were used for experiments. The room temperature electrical conductivity of the Si:F:H samples have been measured.

Detailed information about P- or B-doped a-Si:H alloys is listed in Table I. The characteristics of the n-type (P or As) a-Si:F:H alloys are listed in Table II. The characteristics of the high temperature thermally annealed (HTA) a-Si:H(B) samples are listed in Table III. For comparison, we have also made EER measurements on ion-damaged, laser-annealed Si samples. A silicon wafer, (100), was bombarded with 100 KeV Si ion (total dosage of 10^{16} ions/cm^2) and subsequently annealed with 15 nanosecond pulses of a frequency doubled Nd:YAG laser at energy densities ranging from 0.1 to 0.75 J/cm^2 [75]. The characteristics of ion-damaged, laser annealed Si samples are listed in Table IV.

3.2 RAMAN SCATTERING SPECTROSCOPY

In this section we describe the general theory

(Sec.3.2.1) and experimental techniques of Raman spectroscopy (Sec.3.2.2) followed by discussion of our experimental results (Sec.3.2.3) and the interpretation of these results (Sec.3.2.4).

3.2.1 General description of Raman scattering

Raman scattering is the inelastic scattering of photons by a crystal. Photons of energy, $\hbar\omega$, are incident on a crystal and scattered to give photons up or down shipted by ~ 100 to ~ 1000 cm^{-1} from the incident laser line in first order Raman scattering. These shifts are due to the creation or annihilation of phonons (excitation or de-excitation of the crystal lattice vibrations). First order (one phonon) Raman scattering occurs at the frequencies of the phonons whose wave vectors are equal to the wavevectors transfer in the experiment. The stoke process is the one in which the light quanta lose energy in the scattering (phonon creation), and the anti-stokes process the one in which energy is gained by the light (phonon annihilation). The phonon wave vectors can have any value within the first Brillouin zone, the maximum being of order π/d, where d is the lattice constant. This maximum is typically of the order 3×10^{8} cm^{-1}. Incident light with a frequency of 20,000 cm^{-1} ($\sim$5000 Å) has a wave vector inside the crystaily of order 2×10^{5}

cm^{-1} (wave vector = 2 π x refractive index x wavenumber). For scattering of the light through $\pi/2$, wave vector conservation requires the wave vector of the phonon created or destroyed to be $2x2x10^5$ cm^{-1}. This is small compared to π/d, and hence for crystaline caterials, conservation of momentum dictates only optical phonons at $\vec{q}\approx 0$ give rise to 1st order Raman scattering. In addition, symmetry condition on the range of polarizability place further restrictions on Raman active lattice vibrational modes.

On the other hand, in a-materials, $\vec{q}$ is no longer an applicable quantum number; hence both optic and acoustic phonon at the zone boundries contribute to first order Raman scattering.

Specifically, the Raman scattering frequency may be respresented by the equations,

$$\hbar\omega_s = \hbar\omega_i \pm \hbar\omega_p \qquad \text{----------(3.2.1)}$$

$$\hbar\vec{k}_s = \hbar\vec{k}_i \pm \hbar\vec{q} \qquad \text{----------(3.2.2)}$$

where ω_i, $\vec{k}_i$ are the frequency and wave vector of incident photon. ω_s, $\vec{k}_s$ are the frequency and wave vector of the scattered photon. ω_p, $\vec{q}$ refer to the frequency and the wave vector of the absorbed or emitted phonons in the scattering process. The positive sign is due to the phonon absorption (anti-stoke line) and the nega-

tive sign is due to the phonon emission (stoke line) in the scattering process.

The diagram for the first order Raman process is shown in Fig.(3.2.1)[76] . The initial state, with photon ω_i shown at the left-hand side of the diagram, and the final state, with photon ω_s and phonon ω_p shown on the right. Since momenta are conserved at each vertex, the presence of crystallinity limits the range of $\vec{q}$ to the region of the zone center ($\vec{q} \approx 0$).

In order to calculate the intensity of the Raman scattering, following Born and Bradurn[77] , semi-classical radiation theory, the intensity of the scattered light is obtained by calculating the electric moment $\vec{M}$ set up in the crystal by the electric vector R_e $[\exp(-i\omega t)]$ of the incident light. If the polarizability tensor associated with the electrons in the crystal is $\alpha_{\rho\sigma}$ then

$$M_\rho = \sum_\sigma \alpha_{\rho\sigma} E_\sigma \qquad \text{----------(3.2.3)}$$

The scattered light is produced by re-radiation of energy by the oscillating dipole moment $\vec{M}$. The intensity of scattered light is proportional to $|\vec{M}|^2$ and inversly proportional to the fourth power of the wavelengh of the scattered light[76] . Because of the existence of the electron-lattice interaction H_{el} , the electronic eigenvalues and wave functions in a diatomic lattice

depend on the relative displacement amplitude $\vec{r}$ of the two sub-lattices, and the electronic polarizability tensor can be expanded in a power series in $\vec{r}$:

$$\alpha_{\rho\sigma} = \alpha_{\rho\alpha}^{(o)} + \sum_{\mu} \alpha_{\rho\sigma,\mu} r_{\mu} + \sum_{\mu\nu} \alpha_{\rho\sigma,\mu\nu} r_{\mu} r_{\mu} + O(r) \qquad \text{--------(3.2.4)}$$

where

$$\alpha_{\rho\sigma,\mu} = \left(\frac{\partial \alpha_{\rho\alpha}}{\partial r_{\mu}} \right)_{r=o} \quad \text{and} \quad \alpha_{\rho\alpha,\mu\nu} = \left(\frac{\partial^2 \alpha_{\rho\sigma}}{\partial r_{\mu} \partial r_{\nu}} \right)_{r=o}$$

The term linear in $\vec{r}$ gives rise to the first order Raman scattering, the quadratic term gives rise to the second-order Raman scattering, and so on. The Born and Bradburn method[77] has been applied to the first order Raman scattering in diamond by Smith[78]. The square of the relative displacement amplitude caused by a single optical phonon in diamond is given by

$$\langle r^2 \rangle = \frac{\hbar}{2M\omega_o} \qquad \text{----------(3.2.5)}$$

where ω_o is the optical phonon frequency.

Raman scattering is a sensitive probe of the vibrational modes of the solid. For most Raman measurements, the energy of the photons involved is a few eV. The wave vector of the photon is negligible compared to the maximum phonon wave vector in the first Brillouin zone. In an ideal crystalline solid, the momentum in the interaction is conserved. Therefore the momentum of

the phonon $\vec{q}$ involved is nearly zero and it is situated at the center of the Brillouin zone. The dispersion of phonon for c-Si is shown in Fig.(3.2.2a). There are six branches in the dispersion spectrum of the phonon having two atoms per unit cell consisting of three modes for the optical branch and three for the acoustic branch. The conservation law represented by Eq.(3.2.1) and Eq.(3.2.2) dictates a single Raman line near $\vec{q} \approx 0$.

However, since phonon states are not denumerated by momentum, the above mentioned conservation law has no meaning, resulting in the appearance of the whole phonon branch rather than a particular value of $\vec{q}$. It has been shown[79] that the Raman spectrum for an amorphous material may be closely corelated with the phonon density of states with its crystalline-counterpart. Raman data give essentially the phonon DOS. Fig.(3.2.2b) shows a schematic form of the Raman spectra of an a-Si and c-Si.

The first order Raman active scattering is one of the best tools to study materials which are ordered or disordered. Within the past few years several groups have reported that the Raman frequencies have an intermediate value between disorder (~480 cm^{-1}) and order (~ 522 cm^{-1}) in Si:H[13,80] or Si:F:H[26-28] alloys. They always involve a shift of the 522 cm^{-1} line towards lower energy that is accompanied by a broadening. Tsu et al.[81]

have observed downshift of to 7 cm^{-1} (to 515 cm^{-1}) on ion-damaged, laser-annealed Si. Morhange et al.[80] also obtained a similar results in the Raman spectrum of ion-damaged, laser-annealed Si. The Raman linewidth was~8 cm^{-1} . Tsu et al.[26-28] have also reported Raman frequencies that cover the range from 476 cm^{-1} to 520 cm^{-1} on n-type a-Si:F:H alloys. Again the linewidth increases with decreasing phonon energy. Iqbal et al.[82] reported that polycrystalline films with a measured grain size of the order of 100 Å has the Raman frequency 517 cm^{-1} and Raman width of 6 cm^{-1} .

Richter et al.[59] provided a detailed model which was based on a relaxation in the $\vec{q}$-vector selection rule for the excitation of the Raman active optical phonon. Tsu et al.[28] have used the particle size effect to interpret μc-Si. The downshift and the broadening of the Raman peak for heavily P- or As-doped a-Si:F:H can be interpreted by the finite size effects of the microcrystalline structure of Si. The size of microcrystallite ("particle size") can be calculated from the measured Raman frequency and Raman linewidth in Raman scattering. Tsu et al. also reported[27] two component phase (a-phase and uc-phase) in heavily P-doped Si:F:H alloys (P $\sim$1%). Two component for uc-Si:F:H alloys is shown in Fig.(3.2.2c).

Tsu et al.[28] also reported that the downshift of

Raman frequency to ~ 517 cm^{-1} associated with c-Si and the broadening linewidth around 16 cm^{-1} . The Raman linewidth of HTA-a:Si:H(B) sample is narrower than the heavily doped n-type a-Si:F:H alloys. They interpreted by Fano-shift due to the interaction of a continum, i.e., free carriers, with the phonons.

3.2.2 Experimental set up and details of Raman scattering

The functional block diagram of Raman scattering set up is shown in Fig.(3.2.3). The backscattering geometry was used for all the measurement. The excitation light source is a 6 watt Argon ion laser. The 4880 Å laser line is used in this measurement. The laser light is reflected off two mirrors and passes through one interference filter (I.F.), one pinhole collimator and is focused by a cylindrical lens onto the sample. The purpose of the cylindrical focusing lens is to avoid heating of the sample by focusing the light to a narrow line instead of a point. Typically the laser was used at a power level of about 0.5 watt so as to avoid annealing or damaging the thin film specimens. The scattering light from the sample is collected by a spherical focusing lens onto the entrance slit of double grating monochromator Spex model 1401/14018. (The entrance slit, the second and the exit slit are normal-

ly set at 200 μm corresponding to a spectral slit width of 1 cm^{-1}). We obtained a Raman line width of 4 cm^{-1} for c-Si with this resolution of the monochromator. The silt width was changed to 1000 μm (corresponds to a resolution of 5 cm^{-1}) for the a-Si samples because the spectra features are much broader than for c-Si.

Light leaving the final exit slit of the spectrometer is focused onto the cathode of a cooled photomultiplier tube (Product for Research, Inc. model 9498-31). The output signal of the photomultiplier tube is processed by a photon counting electronic system. The analog output signal of the photon counting system is connected to a strip chart recorder.

3.2.3 Experimental results of Raman scattering spectrum

We have carried out the Raman scattering experiment for the following samples:(a) unannealed B- or P-doped a-Si:H, (b) high temperature thermally annealed a-Si:H(B), (c) lightly doped n-type (P or As) a-Si:F:H, and (d) heavily doped n-type (P or As) a-Si:F:H alloys. The experimental results of Raman scattering and the characteristics of all samples are summarized in Figs. (3.2.4), (3.2.5), (3.2.6). and Tables I, II, III, we also listed the Raman peak and linewidth for the ion-damaged, laser-annealed silicon in Table IV. This

table was reported by Tsu et al.[75] and includes characteractization by transmission electron microscope (TEM), Channeling and Raman, etc.

In Fig. (3.2.4) we display the typical Raman spectra of the following samples: (a) unannealed a-Si:H, (b) undoped a-Si:F:H, (c) heavily As-doped a-Si:F:H (NOVA-101 and NOVA-103) samples. The Raman frequency for a-Si:H samples have a broad peak at $\sim$ 480 cm^{-1} , which is associated with the amorphous phase of silicon. Later we will explain why the Raman frequency in a-Si:H is at $\sim$480 cm^{-1} with linewidth $\sim$ 80 - 100 cm^{-1}.

For intrinsic and lightly P- or As-doped a-Si:F:H alloys, the Raman frequency is around 480 cm^{-1} with the Raman width between 75 cm^{-1} to 80 cm^{-1}. The structure of this alloy is also in an amorphous phase.

Heavily P- or As-doped a-Si:F:H alloys present a Raman frequency which have an intermediate range between 480 cm^{-1} (a-Si) and 522 cm^{-1} (c-Si).

Fig.(3.2.5) shows that the Raman frequency for these heavily As-doped a-Si:F:H alloys have shifted to higher energy position with narrower linewidth than a-Si. The spectral shape of the Raman spectrum for these alloy systems is asymmetric. Among many possible mechanisms for the asymmetry, imhomogenity and the presence of a two phase system, i.e. microcrystalline

and amorphous, plays important roles.

Fig. (3.2.6) shows the Raman spectrum for a high temperature thermally annealed a-Si:H(B) sample (44B in Table III). This spectrum exhits a Raman peak at $\sim$ 517 cm^{-1} with linewidth 17 cm^{-1} and a small shoulder at 495 cm (It is displyed in the insert). This small shoulder may be due to laser line.

In Table I we summarize the Raman features (Raman frequency and linewidth) of a number of unannealed a-Si:H samples. These samples were doped with either phorphous or boron. The results of Raman scattering for the a-Si:H(B) and a-Si:H(P) alloys listed in this table show that the Raman peaks occur at around 455 cm^{-1} to 486 cm^{-1} with linewidth around 71 cm^{-1} - 86 cm^{-1}.

The Raman features for lightly or heavily doped n-type a-Si:F:H alloys are summarized in Table II. All heavily P- or As-doped a-Si:F:H alloys show the Raman peaks between $\sim$508 cm^{-1} and $\sim$520 cm^{-1} with linewidth 40 cm^{-1} - 20 cm^{-1} whereas the lightly doped n-type or undoped a-Si:F:H has the Raman peak at $\sim$480 cm^{-1} with linewidth $\sim$80 cm^{-1}.

Table III shows the Raman features of HTA-a:Si:H(B) alloys, the Raman peak of all samples shift down to a narrow region of 516 - 517 cm^{-1}, and the linewidth decreases considerably to around $\sim$18 to 14 cm^{-1}.

Table IV lists the reported results[75] of electron emission microscope (TEM), Channeling, Raman scattering, our mesurements of EER experiments and the characteristics of ion-damaged, laser-annealed Si.

3.2.4 Interpretation of Raman scattering spectrum

Let us try to understand the Raman spectra of a-Si first. Typically, the structure related to the TO phonon DOS at the zone boundaries has a broad peak at $\sim$ 480 cm^{-1} with linewidth $\sim$ 80 cm^{-1}. In comparison, c-Si has a narrow peak at 522 cm^{-1} with linewidth $\sim$ 4 cm^{-1} at room temperature.

The broadening and down shift of the Raman peak in a-Si relative to c-Si can be attributed to its highly disordered states. In c-Si, the dispersion curves of phonons consists of the optic (TO, LO) and acoustic (TA, LA) branches, [see Fig.(3.3.2a)][83-84] . The optical phonons (TO, LO) near the zone center contribute to a sharp Raman peak ($\sim$ 522 cm^{-1}) and narrow linewidth ($\Delta\omega \sim 4$ cm^{-1}) in c-Si. On the other hand, for a-Si, because it is a disordered material, the relaxation of $\vec{q}$ vector (finite crystallite size) can be applied[28] .

In general, the highest DOS occurs near the zone-boundary. The DOS of TO and TA phonons at the zone boundaries usually represents the most prominant features in the Raman spectrum of a-Si [see

Fig.(3.2.2b)] . In a-Si the TO-peaks are down shifted to 480 cm^{-1} as contrasted to 522 cm^{-1} for c-Si. In addition the peaks are considerable broadened. The schematic drawing of Fig.(3.2.2b) illustrates these results can occur.

Because of the reciprocal relation between particle size and wave vector, finite size can give rise to a value for the $\vec{q}$ vector between $\vec{q}\approx 0$ and $\vec{q}_{B,Z}$, where $q_{B,Z}$ is a wave vector of phonon at the Brillouin zone boundaries. For a particle of size ℓ we have a fixed value of Δq which is determined by $\ell \cdot \Delta q \approx 2\pi$. For the "particle" size, ℓ, heaving a value abiut 40 Å - 60 Å (We have called this microcrystalline, μc), the corresponding $\vec{q}$ is of the order of $\Delta q \approx 2\pi/\ell$. From the phonon dispersion relation, we have obtained the frequency corresponding to Δq. Therefore, we found a downshift of the Raman frequency and broadening of the linewidth associated with c-Si for a μc-Si specimen. The broadening of the linewidth is due to the particle size effect. Fig.(3.2.2b) also illustrates the broadening effect. The Raman features (Raman frequency and width) are related to the size of crystallite of Si. The experimental results of Raman scattering for heavily doped n-type a-Si:F:H are intrepreted by this size effect.

In Fig.(3.2.2c) we show typical Raman features of

μc-Si:F:H alloys. It has a major peak of Raman frequency at around 519.5 cm^{-1} and shoulder peak at around 480 cm^{-1} . The 519.5 cm^{-1} Raman peak is due to micrystalline structure of Si and 480 cm^{-1} Raman peak is due to amorphous structure. This sample is a heavily P-doped (1 %) a-Si:F:H alloy. We have interpreted our result by the presence of a two phased material (μc- and a- phase)[28] . We deconvoluted the Raman spectrum of this sample into two components (μc- and a- component). $I_{\mu c}$ denotes the total area of the μc-phase and I_a denotes the total area of the a- phase. The ratio of ρ (= $I_{\mu c}$ /I_a) equals 0.29.

An ideal crystal behaves as a "particle" which has an infinite size (i.e. $\ell \to \infty$). From Fourier's transformations of $\vec{r}$ space and $\vec{q}$ space we have a relationship between dimension of "particle" size ℓ and wave vector $\Delta\vec{q}$, i.e. $\vec{\ell}\cdot\Delta\vec{q} \approx 2\pi$. Therefore, for a given ℓ , $\Delta\vec{q}$ is uniquely determined. We obtained a relationship between particle size ℓ and down shift of Raman frequency $(\omega_c-\omega)$, i.e. $\ell \sim 1/(\omega_c-\omega)$, from the phonon dispersin relation obtained by neutron scattering[83-84] . The symbol ω_c denotes the Raman frequency of c-Si. This relationship is illustrated by the dashed line in Fig.(3.2.7). Heavily doped n-type (P or As) a-Si:F:H alloys show the Raman peak in the range 508 - 520 cm^{-1} with linewidth in the range 48 - 20 cm^{-1} . The Raman

peak position and width for a number of these samples are listed in Table II. The experimentally determined value of Raman frequency vs. linewidth fall very nicely on the dashed curve. We therefore conclude that the particle size of this kind of alloy is in the 20-50 Å range. Consequently, those experiments show that heavily doped a-Si:F:H alloys have a microcrystalline structure.

On the other hand, HTA-a-Si:H(B) alloys displayed a Raman peak at ~ 517 cm^{-1} with linewidth ~ 18 cm^{-1} (see Table III). From Fig.(3.2.7) we find that Raman frequency linewidth of the HTA-a-Si:H(B) sample does not fall on either of the curve. The Raman features of the HTA-a:Si:H(B) alloys can be explained by Fano shift[85]. Fano shift is due to interaction of a continum, free carriers, with phonons[86].

3.3 ELECTROLYTE ELECTROREFLECTANCE EXPERIMENT

We give a general description of modulation spectroscopy and electrolyte electroreflectance (EER) technique in the first section. In Sec. (3.3.2) we describe the details of the experimental method and apparatus. The experimental results and interpretation are described in Sec. (3.3.3) and Sec. (3.3.4), respectively.

3.3.1 Electrolyte electroreflectance technique

In modulation spectroscopy some parameter of the sample being measured is varied so as to produce a change in the optical reflectance or transmittance of the solid. The optical properties may be modified directly by applying a periodic external perturbation such as electric or magnetic field, temperature, uniaxial stress, etc. or a repetitive internal modulation such as wavelength modulation[32-35] .

The periodic variation of the measurement parameters gives rise to sharp, differential-like spectra in the region of photon energies where optical excitation processes occur. Futhermore, modulation spectroscopy also suppresses uninteresting background effects and emphasizes relevent optical features. In this section we describe the electric field modulated reflectivity spectroscopy using the electrolyte technique (EER).

As with all external modulation techniques, the perturbation (electric field, $\vec{\mathcal{E}}$) changes the dielectric properties of the unperturbed solids. These changes are described in terms of a change , $\Delta\epsilon(\omega)$, of the complex dielectric function, $\epsilon(\omega)$. The fundamental quantity which describes the optical response of the material is the complex dielectric function $\epsilon(\omega) = \epsilon_1(\omega) + i\epsilon_2(\omega)$.

In this section we assume that (a) this dielectric function is uniformly changed by the modulation by amounts $\Delta\epsilon_1$ and $\Delta\epsilon_2$ and (b) that both ϵ and $\Delta\epsilon$ are

scalar quantities. The reflecting surface occurs at the discontinuous interface between two different, but homogeneous media (substrate - ambient). The Frenel reflection equation for near-normal incident light is

$$R = |(n-n_a)/(n+n_a)|^2 \qquad \text{----------(3.3.1)}$$

$$n^2 = \epsilon \ , \quad n_a^2 = \epsilon_a \qquad \text{----------(3.3.2)}$$

where n_a is the real refractive index of the ambient. It can be shown[32] that:

$$\frac{\Delta R}{R} = R_e[2n_a \Delta\epsilon/n(\epsilon - \epsilon_a) \qquad \text{----------(3.3.3)}$$

$$= R_e[(\alpha - i\beta)\Delta\epsilon] \qquad \text{----------(3.3.4)}$$

$$= \alpha(\epsilon_1, \epsilon_2, \epsilon_a)\Delta\epsilon_1 + \beta(\epsilon_1, \epsilon_2, \epsilon_a)\Delta\epsilon_2 \qquad \text{---(3.3.5)}$$

where α and β are the Seraphin coefficients. The Seraphin coefficients have a characteristic photon energy dependence for most semiconductors.

The quantity $\Delta\epsilon(\vec{\xi})$ is obtained by adding a perturbation term, H', to the Hamiltonian, H_o, of the unperturbation crystal, and $\epsilon(\vec{\xi})$ can be calculated approximately by first-order perturbation theory. In contrast to other forms of modulation spectroscopy, the perturbation term $e\vec{\xi}\cdot\vec{r}$ for the electric field is not lattice periodic. It represents a net force that accelerates the electron, and it therefore completely destroys the translational invariance of the Hamiltoni-

an in the field direction. Although this appears to be a trivial property of the field perturbation, it is in fact the central reason for the complexity of ER theory. It also accounts for the remarkable fact that EER spectra for low fields depends on the third derivative of the unperturbed dielectric function, in contrast to modulation where lattice periodicity is retaines and first derivatives are observed.

The fundamental importance of translational invariance in determining dielectric properties, in general, and in determining the gross features of modulation specrtra in particular, can be seen from a simple physical model. Consider first a free electron for which the Hamiltonian, $H = \vec{p}^{\,2}/2m$, is invariant to any translation, and therefore the electron momentum, $\vec{p}=\hbar\vec{k}$, is rigorously conserved. The first order optical transition is not allowed due to the conservation of momentum and energy. Therefore, the sum of allowed transitions for any finite photon energy is identically zero for the free electron.

If the electron is in a crystal, the Hamiltonian, $H = \vec{p}^{\,2}/2m + V(\vec{r})$, where $V(\vec{r})$ is invariant only to the class of translations that takes the crystal into itself. Consequently, momentum conservation is also weakened, and the momentum $\hbar\vec{k}$ is now a good quantum number only within a vector, $\vec{K}_n$, of the reciprocal lattice.

The free electron energy parabola breaks up into energy bands. Optical absorption is now possible in first order by ultizing a reciprocal lattice vector to obtain momentum conservation. For a three dimensional fundamental absorption edge, the imaginary part of the dielectric function assumes the well-known square root threshold form. If the crystal is now perturbed, its Hamiltonian, $H = \vec{p}^2/2m + V(\vec{r}) + H'$ will generally have known symmetry depending on the form of H'. If periodicity is retained, the momentum is still a good quantum number to within a reciprocal lattice vector. Optical transitions remain vertical as shown in Fig.(3.3.1a). Consequently, the dominant changes appear directly as small shifts in energy gaps or amplitude of momentum matrix elements. Since these shifts are generally small on the scale of energy gaps, the perturbation induced changes in $\epsilon_2(\omega)$ are of first order and are approximately first derivative lineshape, as shown schematically in this figures.

If the perturbation is an electric field, $H' = e\vec{\mathcal{E}} \cdot \vec{r}$ than the translational invariance is lost. The electron accelerates, and momentum is no longer a good quantum number in the field direction. Consequently, the one electron Bloch functions of the unperturbed crystal become mixed. This is equivalent to spreading the formerly sharp vertical translations over a finite

range of initial and final momentum, as shown in Fig.(3.3.1b). If the field is not too large, the mixing will be restricted to those wavefunctions near the originally vertical allowed transition. This will smear out structure in the unperturbed dielectric function, yielding a more complicated difference spectrum having change in sign. The difference can be approximated only by higher derivatives of the unperturbed dielectric function. These effects are illustrated in Fig. (3.3.1b). The two zero crossing in this figure are characteristic of the third derivative.

Recently, Aspnes [34] has found that low values of electric field give invariant lineshapes, determined by the internal parameters of the crystal, and amplitudes that scale quadratically with applied field. Low field ER spectra are obtained only in the range of externally applied fields where both intraband and interband mechanisms can be treated adequately by first order perturbation theory. Perturbation theory implies the existence of two energies per mechanism: the characteristic energy of the perturbation, and a charateristic energy of the system. The perturbation and system energies for the interband mechanism in EER are $e\mathcal{E}a_o$ and E_g. The term $e\mathcal{E}a_o$ is the potential drop across the unit cell, a_o is the lattice constant and E_g is the energy separation between the pair of bands under con-

sideration. Clearly, perturbation theory applies here whenever $e\mathcal{E}a_o << E_g$. Perturbation theory will also apply to the intraband mechanism whenever $|\hbar\Omega| << \Gamma$. The energy $\hbar\Omega$ is the characteristic energy obtained in the quantum mechanical solution of a particle of mass $\mu_{\parallel}$ hich is accelerated in a uniform field of force, $e\vec{\mathcal{E}}$ and Γ is the broadening paramerer. The energy $\hbar\Omega$ can be expressed as

$$\hbar\Omega = \left(\frac{e^2\mathcal{E}^2\hbar^2}{8\mu_{\parallel}} \right)^{1/3} \qquad \text{----------(3.3.6)}$$

$$= \left[e^2(\vec{\mathcal{E}}\cdot\nabla_{\vec{k}})^2 E_{cv}(\vec{k})/8\right]^{1/3} \qquad \text{----------(3.3.7)}$$

where $\mu_{\parallel}$ is the interband reduced mass of the electron in bands c and v evauated in the field direction, and $E_{cv}(\vec{k})$ is the interband energy at $\vec{k}$. Therefore, it is possible to determine interband energies , lifetime broadening and interband reduced masses from ER specrta without the necessity of complicated analysis.

The application of an electric field tilts the bands in a solid so the electron can tunnel through the bands, with an exponentially decreasing transition probability below the interband energy. While an exponential lower energy tail is characteristic of all ER spectra, the oscillations on the higher energy side — the Franz-Keldysh cscillations—— are not evident until intermediate fields are reached.

We now describe the theory associated with the low and the intermediate field cases of electroreflectance. Analytical expression are calculated in these two limits. In both these case the band structure of the solid remains unchanged due to the perturbed electric field. The high field case is defined as one in which the band structure gets modified and there are stark shifts and changes in selection rules. We shall not deal with this case.

The low field limit is found to apply for $|\hbar\Omega| < \Gamma/3$, where $\hbar\Omega$ is the characteristic energy which is defined in Eqs.(3.3.6) and (3.3.7), and Γ is the broadening parameter. The Franz-Keldysh (intermedate field) case occur when $|\hbar\Omega| \approx \Gamma$. In both cases the band structure is unchanged.

Experimentally, the determination of the low field limit is simple, since the following two conditions apply : the linewidth should not change, and the amplitude of the signal should scale linearly with the applied voltage (quadratically with field). If these low field spectra are obtained in a fully depleted space charge region, the spectra are independent of DC bias , modulation waveform or field imhomogenity effects.

The derivation for the expression for $\Delta\epsilon(\vec{\xi},\omega)$ is described in the literature [33] . By means of a standard

time dependent perturbation approach it is possible to describe ER spectra to be nearly proportional to the third derivative of the unperturbed dielectric function. This perturbation approach is used to calculate the dominant resonant term in the third order nonlinear optical susceptibility caused by a uniform electric field. A one electron approximation is used.

The Bloch function satisfies the time dependent Schrodinger equation:

$$H_o \phi_{nk} e^{-i\omega_{n\vec{k}} t} = i\hbar \frac{\partial}{\partial t}(\phi_{n\vec{k}} e^{-i\omega_{n\vec{k}} t}) \quad \text{----------(3.3.8)}$$

where H_o is the unperturbed Hamiltonian and $E_{n\vec{k}} = \hbar \omega_{n\vec{k}}$ is the energy of the state $\phi_{n\vec{k}}(r)$. The spatially uniform field is described by a time dependent perturbation term

$$H_1 = e\vec{\mathcal{E}}.\vec{r}e^{\eta t} \quad \text{----------(3.3.9)}$$

and the photon field by the terms

$$H_+ + H_- = e\vec{\mathcal{E}}_1 \cdot \vec{r}(e^{-i\omega_+ t} + e^{-i\omega_- t}) \quad \text{---------(3.3.10)}$$

where $E_\pm = \hbar \omega_\pm$, $\mathcal{E}$ and $\mathcal{E}_1$ are amplitude vectors of the electric fields involved; η is the (positive) " turn on " parameter that enable the evolution of the one electron wavefunctions to be calculated with the unperturbed crystal at $t = -\infty$. The theory uses the scalar potential guage and the dipole approximation.

The time dependent wavefunction $\psi_{n\vec{k}}(\vec{r},t)$, describing the evolution of $\phi_{n\vec{k}} e^{-i\omega_{n\vec{k}}t}$ is defined by

$$H\psi_{n\vec{k}}(\vec{r},t) = (H_0 + H_1 + H_+ + H_-)\psi_{n\vec{k}}(\vec{r},t) \quad ---(3.3.11)$$

$$= i\hbar\frac{\partial}{\partial t}\psi_{n\vec{k}}(\vec{r},t) \quad ----------(3.3.12)$$

$$\lim_{t\to\infty}\psi_{n\vec{k}}(\vec{r},t) = \phi_{n\vec{k}}e^{-i\omega_{n\vec{k}}t} \quad ----------(3.3.13)$$

The wavefunction $\psi_{nk}(\vec{r},t)$ is evaluated as a power series expansion in the perturbation terms by a Green's function technique to third order. The dielectric tensor ϵ_{ij} can be calculated from the polarization $\vec{P} = \{\vec{p}_i\}$ according to

$$D_i = \epsilon_{ij}\mathcal{E}_j = \delta_{ij}\mathcal{E}_j + 4\pi P_i \quad ----------(3.3.14)$$

where

$$\vec{P} = -\frac{e}{V}\sum_{n,k}\langle\psi_{n\vec{k}}(t)|\vec{r}|\psi_{n\vec{k}}(t)\rangle$$

Choosing terms of the proper time dependence, i.e. $H_+ \sim e^{-i\omega t}$, and only terms that have a dominant contribution to the polarization term due to the perturbation, $\Delta\vec{P}$, the change in the dielectric constant due to the electric field may be calculated to be

$$\Delta\epsilon_{cv}(\omega,\Gamma,\vec{\mathcal{E}}) = -\frac{4\pi e^3\hbar^2}{m^2V}\sum_k\frac{(\hat{\epsilon}\cdot\hat{P}^*_{cv})}{E_{cv}}\frac{1}{\omega}\vec{\mathcal{E}}\cdot\nabla_{\vec{k}}\left[\frac{1}{\omega}\hat{\epsilon}\cdot\frac{\vec{P}_{cv}}{E_{cv}}\right]$$

$$+\frac{4\pi e^4\hbar^2}{m^2V}\sum_k\frac{(\hat{\epsilon}\cdot\hat{P}^*_{cv})}{E_{cv}}\left[\frac{1}{\omega}\hat{\mathcal{E}}\cdot\nabla_{\vec{k}}\left(\frac{1}{\omega}\frac{\hat{\epsilon}\cdot\vec{P}_{cv}}{E_{cv}}\right)\right] \quad --(3.3.15)$$

where

$$\vec{P}_{cv}(\vec{k}) = \frac{1}{E_+ - E_{cv}(\vec{k})}$$

$$E_{cv} = E_c - E_v$$

$$\hat{\epsilon} = \frac{\vec{\mathcal{E}}_1}{|\mathcal{E}_1|}$$

The Eq.(3.3.15) gives the dominant second and third order field induced correction to the dielectric function, varying linearly and quadratically respectively, with DC field $\vec{\mathcal{E}}$. If the crystal has inversion symmetry ($\vec{P}_{cv} = \vec{P}^*_{cv}$) or if $\vec{P}_{cv}$ does not depend on $\vec{k}$, which is usually the case , even in the absence of inversion symmetry , the second order term vanishes. The third order term may be simplified by noting that $1/\omega_{cv}(\vec{k})$ depends more strongly on $\vec{k}$ then either $\vec{P}_{cv}(\vec{k})$ or $E(\vec{k})$. Again, since the range of the resonant denominator ω_{cv} is of the order of Γ , the nonresonant denominator ϵ_{cv} may be replaced by $\hbar\omega$, introducing errors of order $\Gamma/\hbar\omega$ only. The sum over $\vec{k}$ may be replaced by integrals to simplify to

$$\Delta\epsilon_{cv}(\omega,\Gamma,\vec{\mathcal{E}}) = \frac{2Q}{\pi\omega^2}\int d^3\vec{k}\frac{(\hbar\omega)^3}{[E_+ - E_{cv}(\vec{k})^4]} \quad \text{----(3.3.16)}$$

where

$$Q = \frac{2}{(2\pi)^3}\frac{4\pi^2 e^2|\hat{\epsilon}\cdot\vec{P}_{cv}|^2}{m^2} \quad \text{----------(3.3.17)}$$

$$(\hbar\Omega)^3 = \frac{e^2}{8}(\vec{\mathcal{E}}\cdot\nabla_{\vec{k}})^2 E_{cv}(\vec{k}) \quad \text{----------(3.3.18)}$$

$$= e^2\mathcal{E}^2\hbar^2/8\mu_{||} \quad \text{----------(3.3.19)}$$

The linear dielectric constant is (for a photon field of time dependence $e^{-i\omega_+ t}$),

$$\epsilon_{cv}(\omega,\Gamma) = -\frac{Q}{\pi\omega^2}\int d^3\vec{k}\ \frac{1}{E_+ - E_{cv}(k)} \qquad \text{---------(3.3.20)}$$

If $\hbar\Omega$ is linearly independent of $\vec{k}$ in a given energy range,

$$\Delta\epsilon_{cv}(E,\Gamma,\vec{\mathcal{E}}) = \frac{1}{3E^2}(\hbar\Omega\frac{\partial}{\partial E})^3[E^2\epsilon_{cv}(E,\Gamma)] \qquad \text{----(3.3.21)}$$

Thus the third order correction is closely related to the third derivative of the unperturbed dielectric function. We also note that the relative change in reflectivity

$$\frac{\Delta R}{R} \sim R_e(\frac{\Delta\epsilon_{cv}}{\epsilon}) \sim \mathcal{E}^2 \qquad \text{----------(3.3.22)}$$

i.e. the amplitude of the observed electroreflectance signal is proportional to the square of the applied electric field, and is linear in voltage V by Poisson's equation in the space charge region. The first Brillouin zone for a face centered cubic crystal and the high symmetry points and lines are labeled in Fig.(3.3.2). In the reduced zone scheme, the optical transition will appear as a vertical line in an energy band structure diagram as indicated schematically in Fig.(3.3.3)[87].

The EER spectrum of c-Si is shown[88] in Fig.(3.3.4). It displays two very sharp energy

features at about 3.4 eV and 4.5 eV can be associated with band structure of c-Si. The 3.4 energy peak corresponds to E_1 and E_o' optical transitions of c-Si ($L_{3',v} - L_{1,c}$ and $\Gamma_{25',v} - \Gamma_{15,c}$ optical transitions [see Fig.(3.3.3)] . The 4.5 eV energy peak corresponds to the E_2 transition of c-Si ($\Sigma_{2,v} - \Sigma_{3,c}$ and $X_{4,v} - X_{1,c}$ transition). Fig.(3.3.4) also shows more fine structure in the 4.5 eV energy peak.

3.3.2 EER experimental method and setup

In this section we describe in detail the experimental apparatus and method in EER spectroscopy. In these modulated optical studies we have used the electric field modulation technique via electrolyte. This electric field modulation is a transverse surface Schottky barrier type [32] . The modulating voltage is applied between the sample, whose surface is in contact with the electrolyte, and a counter platinum electrode, The electrolyte is a 0.001 M KCl solutions. The sample was covered with micro-stop. A small area is exposed to the monochromatic incident light. The electrical contact on the sample was made by silver paint. The schematic drawing of experimental apparatus for EER system is shown in Fig.(3.3.5).

The light from the 150 watt Xenon arc lamp pass through the monochromator (GCA model EU 700-56) and the

filter. Normally the exit slit is focused onto the sample by means of a spherical focusing mirror. The sample was immersed in an electrolyte that is contained in a fused quartz cell which has an optically high quality front window. The modulated voltage (a square wave with a frequency of 200 Hz) is applied between the sample and the Pt electrode by means of a function generator (HP model 3311Å), which also provides a reference signal to the lock-in amplifier (PAR model 5204 or Ithaca model 391Å). The reference light is collected by the photomultiplier tube (PMT S-1 or S-20).

The reflected light collected by the PMT contains two signals: a DC part, $I_o R$ and a modulated AC part, $I_o \Delta R$, which varies with the modulated frequency f_m . The symbol I_o denotes the intensity of incident light, R denotes the reflectivity of sample. ΔR is the variation of reflectivity. It is desirable to eliminate the common factor I_o in order to obtain the modulated spectrum $\Delta R/R$. The DC output $I_o R$ of the PMT is applied to a mechanical servo amplifier (or an electronic servo amplifier) which adjusts the high voltage on the PMT in order to keep the DC output, $I_o R$, constant. The AC component of the output signal, $I_o \Delta R$, is detected by the lock-in amplifier. The output signal of the lock-in amplifier is proportional to $\Delta R/R$, the relative change in reflectance. The output signal from the lock-in am-

plifier is connected to a chart recorder.

The above normalization procedure is important since it not only yields the most useful experimental quantity $\Delta R/R$ but also automatically corrects for any fluctuations in the reflected intensity due to (a) changes in the incident light intensity (a common problem in high pressure arcs) or (b) variations on the surface of the sample. Thus in normalized modulated spectra, it is not necessary to collect the entire reflected light intensity from the sample since the common factor I_o is eliminated.

For the visible and near ultraviolet light regions of the spectrum the light source is a 150 watt Xenon arc lamp. For the infrared regions of the spectrum the light source is a 75 watt tungstan lamp. We used a S-20 PMT for the wavelength region from 2000 to 8000 Å, and S-1 PMT for wavelength in the region 8000 to 12000 Å.

3.3.3 Experimental results of EER

We show a summary of EER measurement for intrinsic , lightly or heavily P- or As-doped a-Si:F:H alloys in Table V. HTA-a-Si:H (B) alloy results are listed in Table VI. The EER reaults for laser-annealed Si have been included in Table IV, where the detailed specifications of these alloys are also displayed.

We found that there are no EER features in 50 ppm B-doped HTA-a-Si:H(44B) and intrinsic or lightly doped Si:F:H(P) alloys. The otheer materials we have studied are heavily doped n-type (P or As) a-Si:F:H, HTA-a-Si:H(B) alloys (NOVA-51A and NOVA-51B) and ion-damaged, laser-annealed Si samples whose latter materials exhibited EER features.

Let us look at the details of the EER features of heavily doped n-type (P or As) a-Si:F:H alloys. Fig.(3.3.6) to Fig. (3.3.10) show the EER features of alloys such as SPIN-137, SPIN-138, GLAD 35AB, GLAD 35B, FN6#6, FN10#3, FN13#4, FN14#2, NOVA-101, NOVA-102, NOVA-103, NOVA-190 NOVA-191. EER spectra for all heavily doped n-type (P or As) a-Si:F:H alloys show two energy features at 3.4 eV and 4.5 eV, which can be associated with the optical transitions of c-Si [see Fig.(3.3.4)][87-88].

These features are insensitive to the doping element, as can be seen from Fig.(3.3.8) and Fig.(3.3.9). In Fig.(3.3.8) shows that there is very little shift in the peak positions for the As-doped sample NOVA-190 and P-doped sample GLAD 35AB, and GLAD 35B. This is futher confirmed in Fig. (3.3.11), which again shows the EER features of the P-doped samples SPIN-138 and the As-doped sample NOVA-190 to be very similar. Figure (3.3.6), which shows the EER features for the P-doped

a-Si:F:H alloys, SPIN-137 and SPIN-138 are very similar, although SPIN-137 has twice the doping concentration of SPIN-138.

We display the detail EER feature of HTA-a-Si:H(B) alloys (NOVA-51A and NOVA-51B) in Fig.(3.3.12). The samples are similar in all repects except that NOVA-51A is annealed at 900 °C whereas NOVA-51B is annealed at 1000 °C. The EER features are vey similar, except NOVA-51 has considerably narrower peak at 3.4 eV and 4.5 eV, and the peak values shift closer to c-Si values. The comparison of EER spectra for HTA-a-Si:H(B) and μc-Si:F:H(P) are shown in Fig.(3.3.13). We found that there are no signals in sample 44B.

For comparison, we also performed EER measurements for ion-damaged, annealed Si with different laser energy densities. The detailed charateristics of these samples are listed in Table IV. Fig.(3.3.14) shows that the EER features of two of these samples annealed with energy density 0.1 (x4) J/cm^2 and 0.5 J/cm^2 . The symbol x4 in the parathesis denote laser annealed on the sample four times with power densities 0.1 J/cm^2 . First of all, it has narrower peaks at 3.4 eV and 4.5 eV, and the peak values have lower energies. Secondly, it has more structure in the 4.5 peak. This shows that ion-damaged, Si annealed at high energy density has more crystallinity than those with lower energy densi-

ty. The comparison of EER spectra for the samples HTA-a-Si:H(B) and ion-damaged, laser-annealed Si with laser power density 0.5 J/cm^2 is shown in Fig.(3.3.15).

3.3.4 Interpretations of EER spectra

Let us now interpret the EER results in terms of the band structure[87] of the crystalline silicon. c-Si has sharp peaks at 3.4 eV and 4.5 eV [see Fig.(3.3.4)] . The 3.4 eV peak is produced by E_1 transitions primarily (from $L_{3,v}' - L_{1,c}$) along with a small contribution from E_o' transition ($\Gamma_{25,v}' - \Gamma_{15,c}$) [Fig.(3.3.3)] . The 4.5 eV peak corresponds to the E transition from $X_{4,v} - X_{1,c}$ and $\Sigma_{2,v} - \Sigma_{3,c}$ [Fig.(3.3.3)]. This feature is washed out in going from crystalline to amorphous materials[59] . Thus it is to be associated with long range order.

Unannealed Si:H(B), intrinsic or lightly P-doped a-Si:F:H samples show no EER features (Table IV, V). Because it is a amorphous phase rather than μc- phase or c- phase.

However, all heavily P- or As-doped a-Si:F:H alloys show very similar EER features at both 3.4 eV and 4.5 eV [see Fig.(3.3.6) - (3.3.10)] . In the EER spectra of c-Si sharp structure has been reported in the vicinity of 3.4 eV and 4.5 eV. Therefore, the peaks at these energies in Fig.(3.3.6) - Fig.(3.3.10), even

through they are broader, can be associated with c-Si, i.e. they originate from the μc-Si sections of the Si:F:H materials.

High temperature thermally annealed (HTA) a-Si:H(B) samples showed EER features at 3.4 eV and 4.5 eV. In Fig.(3.3.12) showed the EER spectra of NOVA-51A and NOVA-51B samples. Both samples are HTA-a-Si:H(B) alloys but NOVA-51B is annealed at higher temperature than NOVA-51A. The EER features of NOVA-51B is sharper than NOVA-51A. It also has more fine structure at 4.5 eV for NOVA-51B samples. However, the EER spectra of HTA-a-Si:H(B) and heavily P- or As-doped a-Si:F:H alloys are different [see Fig.(3.3.13)]. The 3.4 eV feature of HTA-a-Si:H(B) is sharper than the corresponding peak of highly P-doped a-Si:F:H (for example GLAD 55AB). In addition, the 4.5 eV feature for sample NOVA-51A in Fig.(3.3.13) is begining to show some structure similar to that of c-Si.

The peaks in this figure (for sample NOVA-51A) below about 2.5 eV are clearly due to interference effects.

Fig.(3.3.15) shows the EER features for ion-damaged, laser-annealed Si with energy density 0.5 J/cm^2 is much sharper than HTA-a-Si:H(B) and heavily P- or As-doped samples. The 4.5 eV peak of the ion-damaged, laser-annealed Si also has better fine structure than

HTA-a-Si:H(B).

3.4 OPTICAL PROPERTIES OF SI:H AND SI:F:H ALLOYS

The optical properties of c-Si have been studied in detail by several authors[89-91]. The optical reflectance spectra of a-Si and a-Si:H alloy have also been investigated by several groups[89-94] . Jan et al.[95] have investigated the optical properties of HTA-a-Si:H(B) alloys as well as unannealed a-Si:H(B) and heavily doped n-type a-Si:F:H alloys systems. During the past year μc-Si has received a considerable amount of attention. It has been reported that uc-Si films can be prepared by a number of different conditions in Si:H and Si:F:H alloys[26-28] . Therefore it is quite interesting from both a basic and an applied point of view to investigate the optical properties of a-Si:H(B), HTA-a-Si:H(B) and μc-Si:F:H alloys which are prepared by plasma glow discharge decomposition method and under various controllable μc-deposition parameters. In this section we will study the opticlal properties of the μc-Si:F:H and HTA-a-Si:H(B) as well as unannealed a-Si:H(B) alloy systems.

In the first section we will describe the general review of optical properties of semiconductors. In section (3.4.2) we describe a rotating light pipe reflectometer which we have used to measure the reflectance

spectra of our samples.

Section (3.4.3) explains the methods to get the optical constants from experimentally measurable quantities such as reflectivity using Kramers-Kronig (K.K.) analysis. The experimental results of the optical investigation for the Si:H and Si:F:H alloys will be presented in section (3.4.4). The last part of this section will interpret the experimental results of optical studies of Si:H and Si:F:H alloy systems.

3.4.1 General description of optical properties studies

The linear optical behavior of a solid (nonmagnetic) is determined by the $\vec{k}$ and ω dependent dielectric tensor $\in(\vec{k},\omega)$, which relates the Fourier transforms in time and space of the electric displacement and the electric field.

$$\vec{D}(\vec{k},\omega) = \overleftrightarrow{\epsilon}(\vec{k},\omega)\cdot\vec{E}(\vec{k},\omega) \qquad \text{----------(3.4.1)}$$

$$\vec{D}(\vec{k},\omega) \sim e^{i(\vec{k}\cdot\vec{r}-\omega t)} \qquad \text{----------(3.4.2)}$$

The dielectric tensor is related to the conductivity tensor $\overleftrightarrow{\sigma}$ by the relationship $\overleftrightarrow{\epsilon} = 1 + i\frac{4\pi\overleftrightarrow{\sigma}}{\omega}$. In general the components of $\overleftrightarrow{\sigma}$ and $\overleftrightarrow{\epsilon}$ are complex numbers. Thermodynamics requires that these tensor be symmetric in the absence of an external DC magnetic field. Thus the nine

components of $\overleftrightarrow{\epsilon}$ (or $\overleftrightarrow{\sigma}$) are not all independent. $\vec{\kappa}$ can be assumed equal to zero in the dielectric function because the wavelength of the incident photon is much larger than any characteristics atomic dimensions (lattice constants). We only consider the frequency dependence of the dielectric constants. We also assume that the medium is isotropic. Then the dielectric tensor is reduced to a scalar. The relationship between $\vec{D}$ and $\vec{E}$ can be written as $\vec{D} = \epsilon \vec{E}$.

We obtain the wave equation from Maxwell's equation, eliminating the magnetic field. Thus

$$\nabla^2 E = \frac{\epsilon}{c^2}\frac{\partial^2 E}{\partial t^2} + \frac{4\pi\sigma}{c^2}\frac{\partial^2 E}{\partial t^2} \qquad \text{----------(3.4.3)}$$

The frequency-dependent complex dielectric function can be expressed as

$$\epsilon(\omega) = \epsilon_1(\omega) + i\epsilon_2(\omega) \qquad \text{----------(3.4.4)}$$

where ϵ_1, ϵ_2 are real and imaginary parts of the dielectric constant. Let us define the complex refractive index $N=\sqrt{\epsilon}$. The real and imaginary parts of N are related to ϵ_1 and ϵ_2 by

$$n^2 - k^2 = \epsilon_1 \qquad \text{----------(3.4.5)}$$

$$2nk = \epsilon_2 \qquad \text{----------(3.4.6)}$$

where $N=n+ik$ and n is called the index of refraction ,

k is called the extinction coefficient. A plane wave solution of Eq.(3.4.3) has the form

$$E = E_0 e^{-i\omega(t-\frac{n}{c}x)} e^{-\frac{\alpha}{2}x} \quad \text{----------(3.4.7)}$$

where the absorption coefficient α is related to k by

$$\alpha = \frac{2\omega k}{c} \quad \text{or} \quad \alpha = \frac{4\pi k}{\lambda_0} \quad \text{----------(3.4.8)}$$

where λ_0 is the wavelength of the incident light in vaccum.

For normal incident light in vacuum, the reflectance of an opaque sample is

$$R = \frac{(n-1)^2 + k^2}{(n+1)^2 + k^2} \quad \text{----------(3.4.9)}$$

The generalization of these for non-normal incidence may be found in the literature[96] .

In the above equations, the quantities R can be measured. We obtain the real and imaginary parts of the dielectric constants (ϵ_1 , ϵ_2) using a K.K. analysis. The experimental technique most frequently employed is to measure R over as wide a frequency range as possible and use K.K. analaysis to obtain two optical constants n, k or ϵ_1, ϵ_2. The K.K. analysis be described in the next section.

3.4.2 Optical constants and Kramers-Kronig analysis

The linear response of a non-magnetic solid

i.e. $\mu=1$) with isotropic or cubic symmetry to incident electromagnetic radiation can be described in terms of two optical constants. We only have two optical constants for non-magnetic materials. These two optical constants (ϵ_1, ϵ_2) or (n, k) are related by the dispersion relations. These two pairs of constants also are related as follows

$$\epsilon(\omega) = \epsilon_1(\omega) + i\epsilon_2(\omega) = [n(\omega) + i k(\omega)]^2 \quad --(3.4.10)$$

Let R be the reflectivity at normal incidence of a solid of sufficient thickness so that there is negligible reflection from the rear surface of the solid, then R can be expressed in terms of n and k as following

$$R = \frac{(n-n_s)^2 + k^2}{(n-n_s)^2 + k^2} \quad \text{----------(3.4.11)}$$

generally, the solid is either in air or in a vaccum where $n_s = 1$. n_s is the index refraction of the surrounding media.

In the above equation, n and k are used to relate the experimentally measurable quantities, but it is actually the imaginary part of the dielectric constant, $\epsilon_2(\omega)$, that comes out most directly from the derivation of the optical properties of the solid from its band structure. The relationship between the real and imaginary part of the dielectric constant in the following form we know as the Kramers-Kronig relations which al-

low dispersion and absorption to be related. They are derived by means of the theory of complex variable and application of the causality principle which says that no response can occur until the field is applied.

$$\epsilon_1(\omega) = 1 + \frac{2}{\pi} P\int_0^\infty \frac{\omega' \epsilon_2(\omega')}{\omega'^2 - \omega^2} d\omega' \quad \text{----------(3.4.12)}$$

$$\epsilon_2(\omega) = -\frac{2\omega}{\pi} P\int_0^\infty \frac{\epsilon_1(\omega')}{\omega'^2 - \omega^2} d\omega' + \frac{\sigma_0}{\omega} \quad \text{--------(3.4.13)}$$

where P means the Cauchy principal value of the integral. σ_0 is the conductivity as $\omega \to 0$. Since experimentally we are measuring reflectivity R, it is more useful to express the dispersion relation between r, the magnitude of R, and the phase angle $\theta(\omega)$:

$$r = R(\omega)\exp[i\theta(\omega)] \quad \text{----------(3.4.14)}$$

$$\theta(\omega) = \frac{\omega}{\pi} P\int_0^\infty \frac{[\ln R(\omega') - \ln R(\omega)]}{\omega^2 - \omega'^2} d\omega' \quad \text{------(3.4.15)}$$

where r is a complex reflection coefficient and $\theta(\omega)$ is the phase angle. The two optical constants n and k can be obtained from $R(\omega)$ and $\theta(\omega)$ by the following relations

$$n(\omega) = \frac{1 - R}{1 + R - 2\sqrt{R}\cos\theta} \quad \text{----------(3.4.16)}$$

and

$$k(\omega) = \frac{2\sqrt{R}\sin\theta}{1 + R - 2\sqrt{R}\cos\theta} \quad \text{----------(3.4.17)}$$

If the reflectivity spectrum $R(\omega)$ is measured over

the entire spectral region, then from Eq.(3.4.15), $\theta(\omega)$ can be calculated for all the spectral range. Once the value of $\theta(\omega)$ is obtained, two optical constants n, k can be calculated by Eqs.(3.4.16) and (3.4.17). This method which is used to calculate the optical constants is called K.K. analysis.

The numerical analysis of the K.K. relation is obtained by the integration of the Eq.(3.4.15) and several assumptions. Eq.(3.4.15) can be rewritten as the following:

$$\theta(\omega) = -\frac{1}{2\pi}\int_0^{\infty} \ln R(\omega') \frac{d}{d\omega'}\left[\ln\frac{\omega'-\omega}{\omega'+\omega}\right] d\omega' \quad \text{---(3.4.18)}$$

If we integrate the above equation by parts, then we obtain

$$\theta(\omega) = -\frac{1}{2\pi}\left[\ln R(\omega')\ln\left|\frac{\omega'-\omega}{\omega'+\omega}\right|\right]_0^{\infty} + \frac{1}{2\pi}\int_0^{\infty}\frac{d}{d\omega'}\left[\ln R(\omega')\ln\left|\frac{\omega'-\omega}{\omega'+\omega}\right|\right] d\omega$$

----------(3.4.19)

R is measured only in a limited range of energies from 1.2 to 9.5 eV. In order to get the reflectivity R(E) at lower energy (<1.2 eV) and higher energy (above 9.5 eV), the following extrapolation methods were used in this analysis. In the case of a semiconductor, the reflectivity for photon energy E_i below the fundamental band gap E_g (because k=0 and ϵ_2 =0) is

$$R = \frac{(n-1)^2}{(n+1)^2} \quad \text{for } E_i < E_g \text{ ----------(3.4.20)}$$

For the extrapolation R(E) at the higher energy region the following formula is used:

$$R(E) \approx R_1 \left(\frac{E_1}{E}\right)^{\gamma} \text{----------(3.4.21)}$$

where E_1 is the upper energy limit of the measurement, and R_1 is the reflectivity at energy E_1, in our case the measured highest energy is 9.5 eV, that is E_1 =9.5 eV. The parameter γ is varied in order to obtain values of n and k such that $k \approx 0$ for $E_i < E_g$.

For K.K. analysis Eqs.(3.4.15), (3.4.16) and (3.4.17) were used. The integral in Eq.(3.4.15) was evaluated at each descrete photon energy, E_i, for which the measured reflectivity value, $R(E_i)$, was available. The integral was approximated by multiplying the average value of the integrand between each adjacent pair of energies by the difference ΔE between the energies, and then summing the results (using the trapezoidal rule).

Above the energy E_1, where the reflectivity data were not available, the reflectance spectrum was aproximated by $R_1 (E_1/E)^{\gamma}$. The integration of the phase integral from E_1 to ∞ was

$$\frac{1}{2\pi} \ln\frac{R(E)}{R(E_1)} \ln\left|\frac{E_1+E}{E_1-E}\right| + \frac{\gamma}{n}\sum \frac{1}{n(2n+1)^2} \left(\frac{E}{E_1}\right)^{2n+1} \text{---------(3.4.22)}$$

This sum was compute to 50 terms in the program. The value of γ was varied from 0.0 to 5.0. We chose the value of γ such that $k \approx 0$ (or $\epsilon_2 \approx 0$) for $E_i < E_g$.

The microscopic expression for the diagonal component of $\epsilon(\omega)$ for a direct interband transition from an initial occupied valence state v to a final unoccupied conduction state c in atomic unit ($e=\hbar=m=1$) may be calculated to be

$$\epsilon_{jj} = 1 + \frac{1}{\pi^2} P\int_{\omega_{cv}} \int_{s_{cv}} \frac{F_{jj}^{cv}}{\omega_{cv}^2 - \omega^2} \cdot \frac{ds_{cv} d\omega_{cv}}{|\nabla_{\vec{k}} \omega_{cv}|} + \frac{i}{2\pi\omega} \int \frac{F_{jj}^{cv} ds_{cv}}{|\nabla_{\vec{k}} \omega_{cv}|}$$

----------(3.4.23)

where $\omega_{cv} = \omega_c - \omega_v$, ds_{cv} is the element of surface area on the constant energy surface described by s , at $\omega_{cv} = \omega$, F_{jj}^{cv} is the oscillator strength

$$F_{jj}^{cv} = \frac{2\langle c|P_j|v\rangle\langle v|P_j|c\rangle}{\omega_{cv}} \qquad \text{----------(3.4.24)}$$

where P_j is the j-component of the momentum $\vec{P}$. In most case, the oscillator strength is usually a smooth function of $\vec{k}$, and this is borne out by several calculations. For cubic materials $\epsilon(\omega)$ becomes a scalar, and F_{jj}^{cv} may be replaced by

$$F^{cv} = \frac{1}{3} \sum_j F_{jj}^{cv} = \frac{2}{3} \frac{|\langle c|\vec{P}|v\rangle|^2}{\omega_{cv}} \qquad \text{----------(3.4.25)}$$

We assume that F^{cv} is independent of $\vec{k}$. Therefore, the imaginary part of the dielectric constant $\epsilon_2(\omega)$ may be written as

$$\epsilon_2(\omega) = \frac{2\pi^2}{\omega} F^{cv} \int \frac{1}{4\pi^3} \frac{ds_{cv}}{|\nabla_{\vec{k}} \omega_{cv}|} \qquad \text{----------(3.4.26)}$$

$$= \frac{2\pi^2}{\omega} F^{cv} N_d(\omega_{cv} = \omega) + \text{smooth background}$$

----------(3.4.27)

where N_d is the joint density of states.

Maxima appear in $\epsilon_2(\omega)$ when two conditions are satisfied. The first is that the energy of the exciting radiation be the difference in energy between the two bands, i.e. $\omega_{cv} = \omega_c - \omega_v$. The second condition comes from the joint density of states N_d . The probability of transition will be maximum when

$$\nabla_{\vec{k}} \omega_{cv}(\vec{k}) = 0 \quad \text{----------(3.4.28)}$$

$$\nabla_{\vec{k}} E_c(\vec{k}) = \nabla_{\vec{k}} E_v(\vec{k}) \quad \text{or} \quad \nabla_{\vec{k}} [E_c(\vec{k}) - E_v(\vec{k})] = 0 \quad \text{-----(3.4.29)}$$

These two conditions imply that either the slopes of the two bands are both zero, or that they are equal. The first case occurs at high symmetry points such as Γ, X, L and related transitions exist, for example the E_0' transition occurs at Γ for several diamond and zincblende (DZB) type semiconductors such as Si or Ge. The second case usually occurs along a high symmetry direction such as Λ and leads to, for example, the E_1 set of transitions in the DZB semiconductors see Fig.(3.3.3) . Point in k space where Eq.(3.4.30) is fulfilled are called critical points or Van Hove singularities. At such points, where interband transitions take place, there is a energy peak in $\epsilon_2(\omega)$.

The real part of the dielectric constant $\epsilon_1(\omega)$ goes through a sharp maximum at $\omega = \omega_{cv}$. The real part

of dielectric constant equals the static dielectric constant at low frequencies, i.e. $\epsilon_1(\omega) = \epsilon_1(0)$ as $\omega \rightarrow 0$. As the frequency increses and we approach $\omega = \omega_{cv}$, with $\omega < \omega_{cv}$, $\epsilon_1(\omega)$ increases rapidly both due to the gradient term and $\omega_{cv}^2 - \omega^2$ in the denominator. At $\omega = \omega_{cv}$, the magnitude of $\epsilon_1(\omega)$ is in principle infinite, provided that $F^{cv} \neq 0$. Just above the transition, $\omega_{cv}^2 - \omega^2$ is negative, but large due to the gradient term. As we move away from ω_{cv}, the magnitude of $\epsilon_1(\omega)$ drops and goes positive again, as we approach the next critical point.

In principle one never sees an infinitely sharp line because of line are broadening effects due to lifetime effects, impurities, etc.. This broadening is included phenomenologically by inserting a decay factor Γ in $\epsilon_2(\omega)$ so that

$$\epsilon_2(\omega) = 1 + \frac{1}{\pi^2}\int_{\omega_{cv}}\int_{s_{cv}} \frac{F^{cv}}{\omega_{cv}^2 - (\omega + i\Gamma)^2} \frac{ds_{cv} d\omega_{cv}}{|\nabla_{\vec{k}} \omega_{cv}|} \qquad \text{----------(3.4.30)}$$

Critical points may be described and classified by certain typical lineshape.

3.4.3 Optical reflectance experiment

In this part we describe the measurement of reflectance spectra to investigate the optical properties of Si:H and Si:F:H alloys. The optical reflectance spectrum of Si:H and Si:F:H alloys were measured at

near-normal incidence, by a rotating light pipe reflectometer over an energy range of 1.2 eV to 9.5 eV.

The details about the rotating light pipe reflectometer apparatus are found in the literature . The schematic functional block diagram of the rotating light pipe reflectometer (RLPR) apparatus is shown in Fig.(3.4.1). The light source in the visible light and near infrared light is a 150 watt Xenon arc lamp. The monochromator and predisperser used are GCA model 218 and model 608/218, respectivily. Two blaze wavelength of diffraction grating (1500 Å and 5000 Å) are used in this reflectometer.The number of grooves of the diffraction grating are 1200 grooves/mm and 600 grooves/mm, respectively. We used the diffraction grating of blaze wavelength 1500 Å for ultraviolet light and 5000 Å for infrared light as well as visible light. The S-20 photomultiplier tube (PMT) is used over the energy range of 1.5eV to 5.5 eV and an S-1 PMT is used for energy range lower than 1.5 eV. The light source used for the energy range between 3.2 eV to 9.5 eV was a hydrogen arc lamp. In this energy range the rotating light pipe (supersil #1 fused quartz) was coated with the phosphor (using Sodium Salicylate phosphors) and S-20 PMT was used. The rotating light pipe was mounted inside the working chamber. The chamber was pumped down to 4×10^{-6} torr for vacuum ultraviolet

(VUV) spectra. The absolute accuracy of reflectivity R in the reflectance spectrum is around 2% but the relative accuracy of R is around 0.3%.

3.4.4 Experimental results of reflectance spectroscopy

In this section we will discuss the results of the optical reflectance measurement of Si:H and Si:F:H alloys which were carried out by a high precision rotating light pipe reflectometer at room temperature. The reflectance spectra of all the Si:H and Si:F:H specimens and calculated imaginary part of the dielectric function is presented in this section. The chacteristics of all measured Si:H and Si:F:H specimens are summaried in Table VII. The structure of those alloys which were investigated by Raman scattering, EER modulation and optical techniques are shown in the next to the last column of this table. The interpretation of this optical investigation is presented in the next section.

We have measured the reflectance spectrum over an energy range of 1.2 eV to 9.5 eV of the incident photon for the c-Si, heavily doped n-type (P or As) a-Si:F:H alloys, HTA-a-Si:H(B) and unannealed a-Si:H(B) alloys. In order to check the measuring system of the reflectometer intruments and the computer programs of

Kramers-Kronig analysis we have performed the experiment using a sample of c-Si. The results are shown in Fig.(3.4.2) and Fig.(3.4.3). The insert in the upper-right hand corner of the imaginary part of dielectric function spectrum [Fig.(3.4.3)] displays an expanded plot in the range 6.5 - 8.0 eV. The reflectance spectrum and dielectric functions (real and imaginary parts) of the c-Si agree closely with Philip's results[91]. The reflectance spectrum and ϵ_2 spectrum are shown in the following figures: The results for a-Si:F:H alloys are displayed in Figs.(3.4.4) and (3.4.5). For HTA-a-Si:H(B) alloys the curves are displayed in Figs.(3.4.6) to (3.4.9). For comparison, the reflectance and ϵ_2 spectra of c-Si are included in all the above mentioned figures. The n-type specimens were: (a) one heavily As-doped (NOVA-191) and (b) two P-doped (SPIN-137 and SPIN-138) Si:F:H alloys which had microcrystalline structure as determined by EER and Raman scattering. All of these samples were unannealed Si:F:H alloys. However, they show the properties of microcrystalline structure in optical investigation. The reflectance spectra of these specimens are shown in Fig.(3.4.4). They have energy peaks at 3.4 eV, 4.4 eV and 5.5 eV in the reflectance spectrum. The imaginary part of dielectric function ϵ_2 of these specimens are shown in Fig.(3.4.5). From the figure it is clear that heavily

doped n-type (P or As) Si:F:H alloy presents neither amorphous phase nor single crystalline phase but rather a microcrystalline phase.

The reflectance and ϵ_2 spectra of samples 44A and 44B are shown in Fig.(3.4.6) - (3.4.7). The reflectivity spectrum of 44A (see Fig. 3.4.6) is a typical of that reported for amorphous silicon prepared by either glow discharge[94,98-100], evaporation[91-92,98-100], or chemical vapor deposition[94] . The curve consists of a rather broad, featureless bump with its peak at 4 eV. The Raman spectra of sample 44A is also typical of amorphous silicon (see Table VII).

The effects of high temperature annealing are clearly evident in the reflectivity of sample 44B. These HTA-effects are also displayed in the reflectivity of samples NOVA-51A and NOVA-51B (Fig. 3.4.8). The ϵ_2 spectrum of samples NOVA-51A and NOVA-51B is shown in Fig.(3.4.9). Structures similar to c-Si, i.e. E_1, E_o', E_2, E_1', E_o'' are now clearly discernable. Even though these structure are clearly seen, the reflectance above 3 eV is significant lower than in c-Si. Unlike the observations in HTA-a-Si:H(B) alloys, a study of temperature annealing (350 °C) of glow discharge Si revealed no structure in the reflectivity (or ϵ_2) curves [94] . In the region above $\sim$ 3 eV the Si:H material has a reflectivity lower than c-Si. Hence the HTA-a-Si:H(B)

samples are neither completely crystalline nor completely amorphous. An interpretation of the observations follows in the next section.

3.4.5 Interpretation of optical reflectance spectra

(a) c-Si

For c-Si it has been shown the main contribution to the 3,4 eV peak comes from transitions between the upper valence band along the Λ -axis to the first conduction band (denote E_1) with a small contribution from $\Gamma_{25',v} - \Gamma_{15,c}$ transitions (denote E_o'), where v and c is valence and conduction bands, respectively[101]. The E_2 feature is somewhat more complex. It is due to transitions from an extended region of the Brillouin zone including the X point ($X_{4,v} - X_{1,c}$) and Σ regions ($\Sigma_{2,v} - \Sigma_{3,c}$)[101]. The E_1' feature is associated with transitions from the upper valence band along the Λ -axis to the second conduction band. The E_o'' features displayed in the insert of Fig.(3.4.3) has never before been resolved in the reflectivity spectrum of Si and based on band-structure calculations can be identified with $\Gamma_{25',v} - \Gamma_{15,c}$ transitions[101]. The ϵ_2 spectra of c-Si is quite similar to others of the diamond and zincblende type-materials (DZB) although in some of the other materials of this family E_1 and E_1' are spin-orbit split[102]

(b) unannealed a-Si:H(B) alloys

The ϵ_2 spectra of sample 44A is similar to that observed for various types of a-Si[91-93,94,103] as well as other tetrahedrally bonded amorphous semiconductors[102]. It exhibits a single-bump, asymmetric spectral shape. All the features related to the long range order, e.g. E_2, etc. are absent. The energy of the peak in the amorphous ϵ_2 curve generally is close to that of the E_1 feature of the crystalline material. The relationship is discussed in Refs.(98-100, 103). It is a consequence of the fact that E_1 is due transition along Λ. Such amorphous curves can not be derived from the corresponding crystalline ones simply by smearing out the sharp structures (e.g. E_2, etc.) associated with the long range order.

(c) Heavily doped n-type (P or As) alloys

The ϵ_2 spectra for heavily doped n-type (P or As) a-Si:F:H samples, as well as c-Si, are plotted in Fig.(3.4.5). All heavily doped n-type samples have structure associated with the E_2 and E_1' features of c-Si. The energy position of E_1' for the glow-discharge samples is somewhat higher than that of c-Si. In addition to these peaks, sample SPIN-137 also has a small peak in the vicinity of the E_1 (small contribution from E_o') structure. It does not display an E_o'' feature in

smples SPIN-137 and SPIN-138 (see insert). Below ~ 3 eV these three samples have an ϵ_2 larger than c-Si with that of sample of SPIN-137 being greater than that of samples SPIN-138.

(d) HTA-a-Si:H(B) alloys

The effects of the HTA-a-Si:H(B) alloys (44B, NOVA-51A and NOVA-51B) can be seen in the ϵ_2 spectra of these samples (see Fig.3.4.7 and Fig.3.4.9). The sample 44B exhibits a sharp peak at E_1 (small contribution from E_o''), E_1' and E_o'' associated with c-Si structure. The E_2 peak in ϵ_2 spectra is not as clear and sharp as in c Si. The energy of the E_o feature in sample 44B ($\sim$ 7.2 eV) is also lower than that of c-Si (7.6 eV). The samples of NOVA-51A and NOVA-51B clearly have spectal features corresponding to c-Si. In particular NOVA-51B has a well defined E_2 peak. The energy of the E_o'' feature (see insert) for sample NOVA-51A ($\sim$ 7 eV) is somewhat lower than that of c-Si ($\sim$ 7.6 eV). One of the main differences between the ϵ_2 of the annealed samples and c-Si is the lack of a sharp E_1 (small contribution from E_o'') feature in the former materials. Note that below ~ 3 eV (a) The NOVA-51A and NOVA-51B samples have a large ϵ_2 than c-Si and (b) NOVA-51A has a higher absorption in relation to NOVA-51B.

(e) calculation of n_{eff}

In order to understand the alternations of the optical matrix elements due to the change of the short range order, we consider the effective number n_{eff} (E) of electrons per Si atom which have been excited at a given energy E (or $\hbar\omega$). The calculated results are ploted in Fig.(3.4.10). The curve 1 - 8 in this figure corresponds to the sample 44A, 44B, NOVA-51A, NOVA-51B, NOVA-190, SPIN-138, SPIN-137 and c-Si.

For a-Si (cure 1) it showed the high value of n_{eff} below 4 eV and the low value above 4 eV comparing the other samples except the sample 44B (curve 2) as photon energy above 6 eV.

The curves 2 - 4 are the HTA-a-Si:H(B) sample but curve 1 is the unannealed a-Si:H(B). The effects of the high temperature annealing increase the effective number of electrons n_{eff} per Si atom contirbuting to the optical transitions above the gap $\sim$3 eV. It also reduces the value of n_{eff} below the gap $\sim$3 eV. From the EER and Raman scattering experiments, it improve the crystallinity of Si rather than produce a microcrystalline structure. Curve 5 is a heavily As-doped a-Si:F:H alloy. The curves 6 - 7 are heavily P-doped a-Si:F:H alloys. The value of n_{eff} above the gap $\sim$4.5 ev is higher than HTA-a-Si:H(B) samples (except NOVA-51B, curve 4). The n_{eff} value of heavily doped n-type (P or As) below the gap $\sim$3.4 eV is lower than unan-

nealed a-Si:H(B) alloys and higher than c-Si. The slight downshift of the Raman peaks of heavily doped n-type a-Si:F:H alloys compared to c-Si is probably due to structural effects rather than the Fano-shift[28]. This interpretation is consistent with linewidth considerations.

In c-Si (curve 8) n_{eff} rises steeply above the gap near 3 eV and saturates outside the range ploted here between 16 and 20 eV at a value of 4 corresponding to the 4 valence electron of silicon. The total matrix element between the valence states and the lowest conduction bands therefore must be close to unity. The n of the curve 4, 6 and 7 above 6 eV is higher than c-Si.

CHAPTER VI DISCUSSION AND CONCLUSIONS

In this chapter we would like to summarize the results of the optical,modulated optical and Raman scattering studies in a-Si:H and a-Si:F:H alloys systems. We have investigated the nature of order of a-Si materials. These materials are divided into three categories of (a) HTA-a-Si:H(B) alloys as well as unannealed a-Si:H(B) and a-Si:H(P), (b) heavily doped n-type (P or As) a-Si:F:H alloys with microcrystalline structure and (c) lightly doped n-type (P or As) a-Si:F:H alloys. This investigation provide the information about degree of disorder for Si alloy systems.

For the undoped or lightly doped n-type (P or As) a-Si:F:H alloys show no E (small contribution from E) feature in EER spectra and a broad peak at $\sim$480 cm^{-1} with linewidth $\sim$80 cm^{-1} . These kind of samples present a amorphous phase.

We have carried out the experiment of Raman scattering for unannealed a-Si:H(B) and a-Si:H(P) alloys. These samples show a typical Raman features of amorphous silicon materials ($\sim$ 480 cm^{-1} and $\sim$ 80 cm^{-1}). We also performed the measurement of the reflectance spectra for one unannealed a-Si::H(B) samples (44A). The ϵ_2 spectra feature of this sample exhitbits a single bump, characteristics of the amorphous materials.

Both of experimental results show that these specimens have a disordering structure.

We have performed the measurement of Raman scattering, EER and optical reflectance for heavily doped n-type (P or As) a-Si:F:H alloys. The downshift of the Raman peaks of this samples associated with c-Si is probably due to structure effects[28] rather than the Fano-shift[31] . This interpretation is consistent with linewidth consideration. The 3.4 eV and 4.5 eV peaks of EER spectral feature for heavily doped n-type (P or As) a-Si:F:H look being a very similar spectral shape. The features in the spectra for the heavily doped n-type a-Si:F:H samples indicate that the degree of crystallization is not as good as for the HTA-a-Si:H(B) samples. The EER results are consistent with the reflectivity measurement concerning the lower degre of crystallization of samples heavily doped n-type (P or As) a-Si:F:H alloys in relation to samples HTA-a-Si:H(B).

We did not carry out a systematic studies for the heavily doped n-type (P or As) a-Si:F:H samples in the measurement of reflectance spectra. We only measured the reflectance spectra for three heavily doped n-type (P or As) a-Si:F:H samples (SPIN-137, SPIN-138 and NOVA-191). It is difficult to analyze the ϵ_2 spectra for different doping types. However, two heavily P-doped a-Si:F:H samples with different doping concentra-

tion (SPIN-137, 110 ppm; SPIN-138, 55 ppm) have been measured the reflectance spectra. The ϵ_2 spectra showed that the sample SPIN-137 has a somethat better crystallinity than the sample SPIN-138 even the absorption below 3 eV for the former material is higher than the latter sample. This may be related to the higher degree of doping level [95]. Therefore, the heavily doped n-type (P or As) a-Si:F:H will form a microcrystalline structure of silicon. Three experimental techniques showed that the results are consistent.

The general similarity in ϵ_2 spectra between the HTA-a-Si:H(B) alloys and c-Si (see Fig.3.4.9) is indicative of the crystallinity. For example, both samples NOVA-51A and NOVA-51B exhibit the E_2, E_1' and even E_o'' features (for sample NOVA-51A E is observed at about 7 eV). The experimental results of optical study plus our measurements of the EER spectra of these samples indicates that HTA (900-1100 °C) is sufficient to obtain a high degree of structural order.

The main difference between samples NOVA-51A, NOVA-51B and c-Si is the E_1 (small contribution from E_o') feature which is greatly depressed in the former materials. This effect is probably related to the presence of a large number of free carriers. Aspnes has also noted a depression of the 3.4 eV structure relative to E_1 in heavily doped Si . Evidence for the

presence of these free carriers may be deduced from the downshift of the Raman peak of these samples from 522 cm^{-1} (c-Si) to the values listed in Table VII. This difference can be accounted for the interaction of the phonons with free carriers, i.e. the Fano-shift[31] . We rule out structure effects, i.e. microcrystallinity[28, 31], as the origin of the downshift since samples NOVA-51A and NOVA-51B exhibits such a high degree of crystallinity and because of the narrow linewidth of the Raman peak in relation to its Raman frequency[28] .

In conclusion, our studies show that the use of optical, modulated optical and Raman scattering provides us to gain information about the nature of disorder. In particular, we may discern the difference between structure disorder abnd that induced by a random distribution of heavily doping.

Table I : Summary of characteristics and Raman spectrum features of a number of unannealed a-Si:H samples. The number listed in the square brackets in the Raman Feature Column is the linewidth in cm^{-1}. Glass material is 7059 Corning glass.

Sample	Doping		Sample Thickness (μm)	Substrate Material	Raman Feature (cm^{-1})
	Type	Concentration (ppm)			
P:Si-20A[a]	P	5×10^{-5} (b)	2	NiCr	455
P:Si-18A[a]	P	1×10^{-3} (b)	2.7	NiCr	475
P:Si-19A[a]	P	1×10^{-3} (b)	1.3	NiCr	470
SUN 901,902[c]	P	1000			486 [86]
Pe 285[c]	P	3×10^{-2} (b)	0.3	glass	480 [71]
44A [c]	B	50			480 [81]
63 [c]	B	500			480 [80]
B:Si-13C[a]	B	1×10^{-4} (c)	2	NiCr	475
176A [a]	Intrinsic		2	NiCr	479
176C[a]	Intrinsic		2	NiCr	475 [75]

(a) Sample supplied by Prof. H. Fritzsche.
(b) Quantity is [x] gas / [SiH_4] gas.
(c) Sample supplied by ECD.

Table II : Summary of characteristics and Raman spectrum features of a number of n-type (P or As) a-Si:F:H samples. The number listed in square brackets in the Raman Feature Column is the linewidth in cm^{-1}. The listed resistivity is that measured in the light, i.e. not dark resistivity. The glass subtrate material is 7059 Corning glass.

Sample	Doping		Sample thickness(μm)	Resistivity $(\Omega\text{-cm})^{-1}$	Substrate material	Raman Feature(cm^{-1})
	type	concent.(ppm)				
GLAD 57B	Intrinsic		0.2	10^{-4}	c-Si	478
GLAD 83B	Intrinsic		0.58	10^{-5}	glass(Cr)	478 96
GLAD 62A	P	1000	0.05	13	glass	480 85
GLAD 84A	P	2	0.5	2×10^{-4}	SnO_2/glass	480 85
SUN 860,861	P	1000			glass	482 74
NOVA-101	As				glass	508[a]
NOVA-103	As					512[a]
NOVA-190	As	20	0.4	3	c-Si	517[a] 48
NOVA-191	As	500	0.4		glass	516[b] 30
SPIN-138	P	55	0.25		glass(Mo)	520[a] 23
SPIN-137	P	110	0.25		glass(Mo)	520[a] 20
SUN 1354	P	500	0.3		glass	516[a] 42

(a) Not yet examined for small shoulder at 495 cm^{-1}.

(b) Snows two-phase behavior-small but well-resolved peak at 480 cm^{-1}.

Table III : Summary of characteristics and Raman spectrum features of a number of high temperature thermally annealed (HTA) a-Si:H(B) samples. The number listed in the square brackets in the Raman Feature Column in the linewidth in cm^{-1}. Glass subtrate material is 7059 Corning glass.

Sample	Doping		Anneal. Temp. (°C)	Raman Feature
	Type	Concentration (ppm)		
46	B	50	1000	516.6(a) [18]
44B	B	50	1100	517(a) [14]
NOVA-51A	B	500	900	517(a) [17.5]
NOVA-51B	B	500	1000	516(a) [15.5]

(a) Small shoulder at 495 cm^{-1}.

Table IV : Summary of characterization by TEM, Channeling, Raman spectrum features and the characteristics of 100 keV Si ion-damaged, laser-annealed silicon samples (Ref. 75).

Laser energy density(J/cm^2)	TEM	Channeling	Raman Peak (cm^{-1})	EER Features	
				E_1 (3.4ev)	E_2 (4.5ev)
<0.1	amorphous	amorphous	very bread peak 465	NO	
0.1	polycrystalline & amorphous	almost no channeling	broad, small 513	yes	yes
0.15	more poly., less amorphous	10% - 20% channeling	520 peak width ≃10	yes	yes
0.35	single crystal defect & dislocation	90% channeling	522 peak width ≃6	yes	yes
0.5	defect free single crystal	pefect channeling	522 peak width ≃5	yes	yes
0.75	defect free single crystal	pefect channeling	522 peak width ≃4	yes	yes

Table V : Summary of EER (Electrolyte Electroreflectance) features and characteristics of n-type (P or As) a-Si:F:H samples.

Sample	Doping		Sample Thickness (μm)	Resistivity (Ω-cm^{-1})	Substrate	Mod. Freq. (Hz)	AC (volt)	EER Features	
	type	concent. (ppm)						E_1, E_0' (3.4ev)	E_2 (4.5ev)
GLAD 57B	Intrinsic		0.2	10^{-4}	C-Si	220	20	No EER	
GLAD 84A	P	2	0.5	2×10^{-4}	SnO_2/glass	220	20	No EER	
FN10 #5	P	2%		10^{-4}	Glass	36	70	No EER	
NOVA-101	As		0.1	4×10^{-3}	Glass+Moly.	220	5	yes	yes
NOVA-102	As		0.05	4	Glass+Moly.	220	5	yes	yes
NOVA-103	As		0.2	25	Glass	220	5	yes	yes
NOVA-190	As	20	0.4	3	C-Si	36	1	yes	yes
NOVA-191	As	500	0.4		Glass	220	10	yes	yes
SPIN-138	P	55	0.25		Glass(Mo)	220	8	yes	yes
SPIN-137	P	110	0.25		Glass(Mo)	220	3	yes	yes
GLAD 35AB	P	0.3	0.3	10	C-Si	220	0.4	yes	yes
GLAD 35B	P	0.15	0.15	10	SnO_2/glass	220	0.4	yes	yes
FN6 #6	P	2%		20	Glass	36	20	yes	yes
FN13 #4	P	2%		3×10^{-2}	Glass	17	70	yes	yes
FN14 #2	P	2%		10^{-2}	Stain. St.	36	2	yes	yes
FN10 #3	P	2%		4×10^{-2}	Stain. St.	36	4	yes	yes

Table VI : Summary of Raman spectrum and EER features of a number of high temperature thermally annealed as well as unannealed Si:H(B) samples. The number listed in the square brackets in the Raman Feature Column in the linewidth in cm^{-1}. Glass substrate material is 7059 Corning glass.

Sample	Doping		Annealing temperature ($^{\circ}C$)	Raman Feature (cm^{-1})		EER Feature	
	type	concentration (ppm)		peak	linewidth	E_1 & E_0' (3.4ev)	E_2 (4.5ev)
44A	B	50	unannealed	480	80	No	No
44B	B	50	1000	517(a)	14	No	No
NOVA-51A	B	500	900	517(a)	17.5	Yes	Yes
NOVA-51B	B	500	1000	516(a)	15.5	Yes	Yes

(a) Small shoulder at 495 cm^{-1}.

Table VII : Summary of EER and Raman spectrum features of a number of (heavily doped n-type) a-Si:F:H, high temperature thermally annealed as well as unannealed a-Si:H(B) and c-Si samples.

Samples		Doping		Annealing temp. (°C)	Substrate material	EER	Structures	Raman peak(cm^{-1})
		type	concent.(ppm)					
c-Si	Si				Bulk	Yes	Crystalline	522
NOVA-191	Si:F:H	As	500	Unannealed	c-Si	Yes	Microcrystalline	516
SPIN-138	Si:F:H	P	50	Unannealed	Glass(Mo)	Yes	Microcrystalline	520
SPIN-137	Si:F:H	P	110	Unannealed	Glass(Mo)	Yes	Microcrystalline	520
44A	Si:H	B	50	Unannealed	Glass	No	Amorphous	480
44B	Si:H	B	50	1000	Glass	Yes	Improve crystallinity	517
NOVA-51A	Si:H	B	500	1000	Glass	Yes	Improve crystallinity	517
NOVA-51B	Si:H	B	500	900	Glass	Yes	Improve crystallinity	516

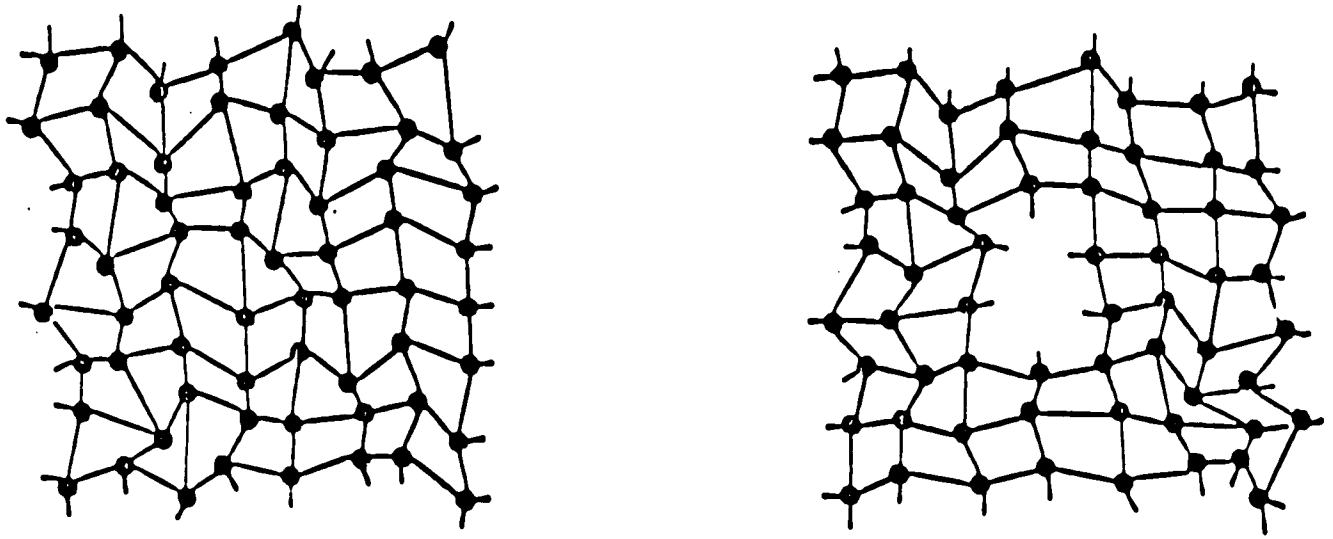

Fig.(2.1) Schematic drawing of continuous random network (CRN) model.
(Ref. 52)

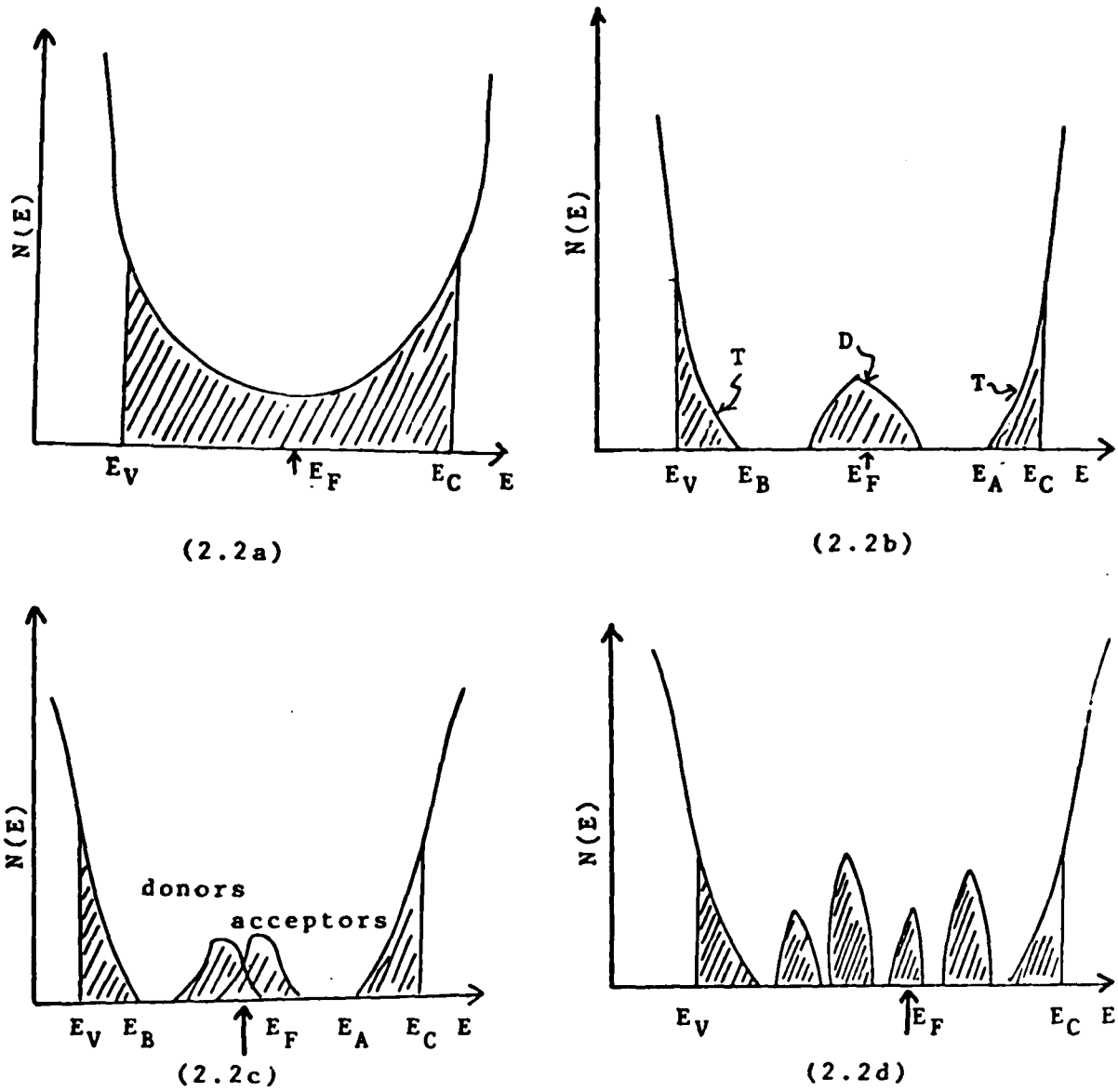

Fig.(2.2) Drawing of density of states (DOS) versus energy of amorphous semiconductors. (Ref. 53)

(2.2a) Density of states of Cohen-Fritzsche-Ovshinsky (CFO) model.

(2.2b) Density of states of Davis-Mott model.

(2.2c) Density of states of modified Davis-Mott model.

(2.2d) Density of states for a real glass with defect states.

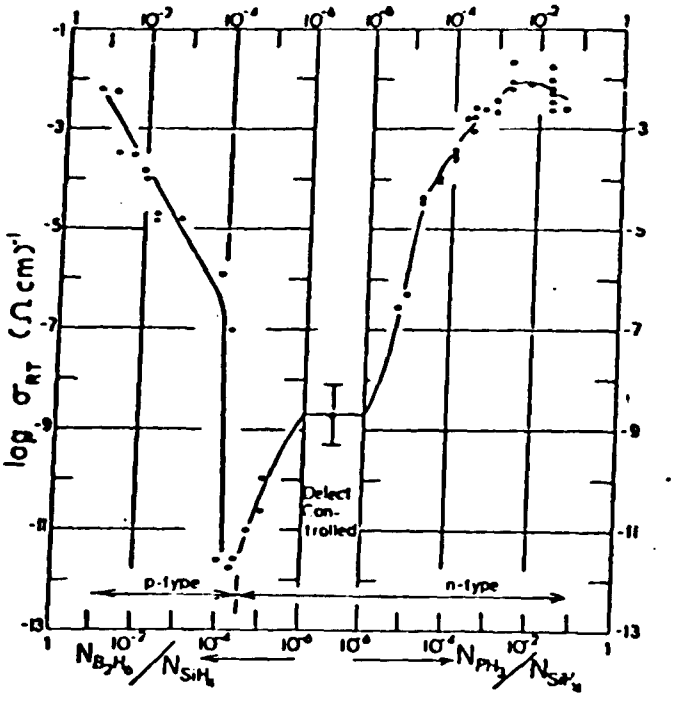

Fig.(2.3) Room temperature conductivity σ_{RT} of n- and p-type a-Si specimens, ploted as a function of the gaseous impurity ratio. For the right-hand curve, this is the number of phosphine to silane molecules in the gas mixture used for specimen preparations. On the left it is the corresponding diborane to silane ratio. The centre refer to undoped specimens. (Ref. 63)

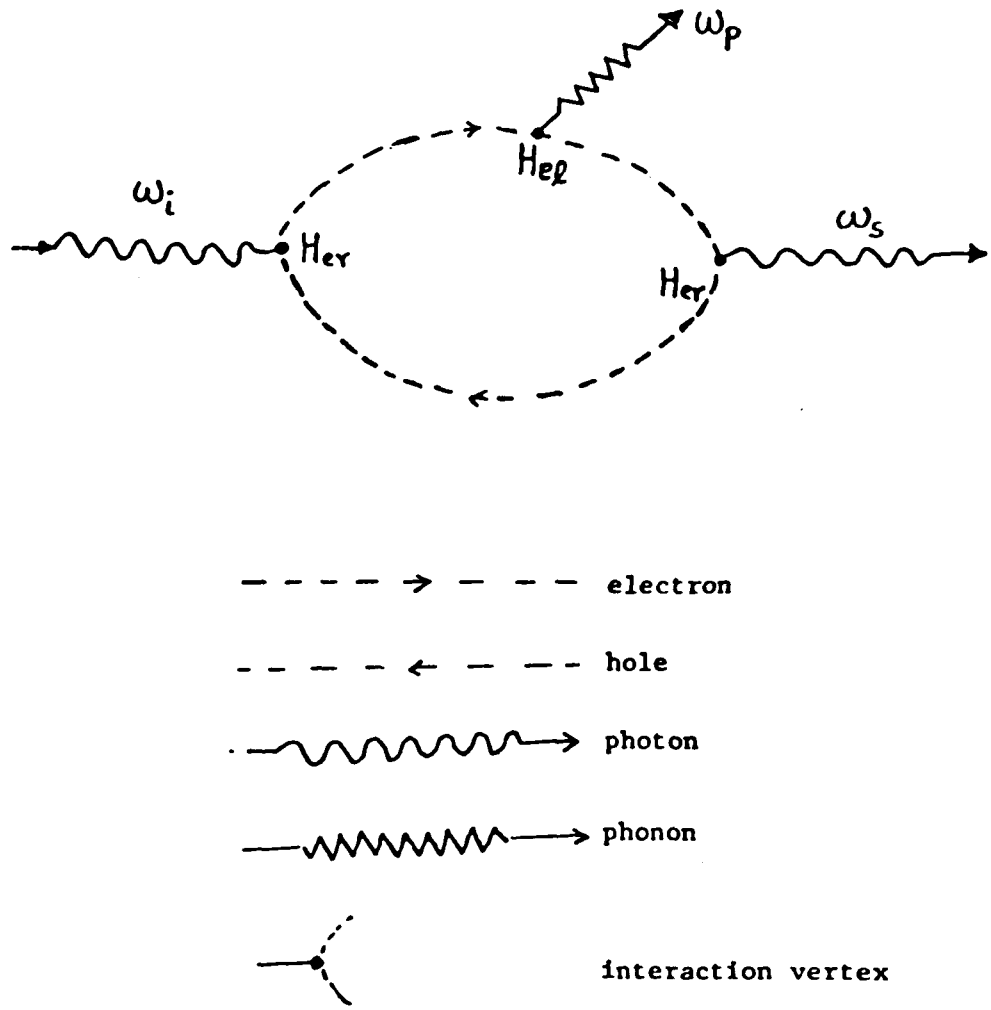

Fig.(3.2.1) The schematics of the elementary Raman scattering process.

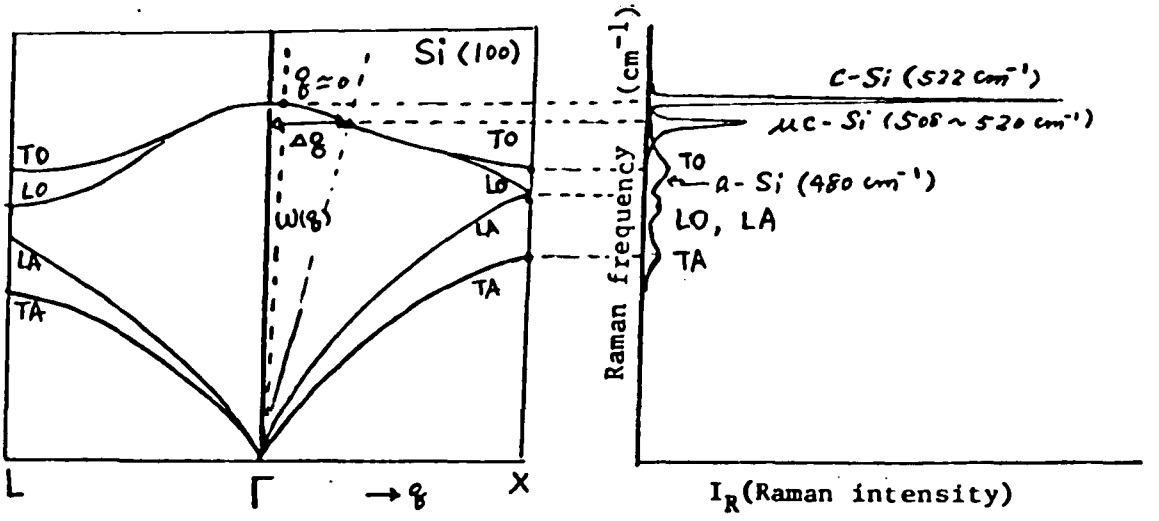

Fig.(3.2.2a) Dispersion curves of phonon $\omega(q)$ for single crystal silicon.

Fig.(3.2.2b) Schematic Raman scattering spectra for a-Si, μc-Si, c-Si.

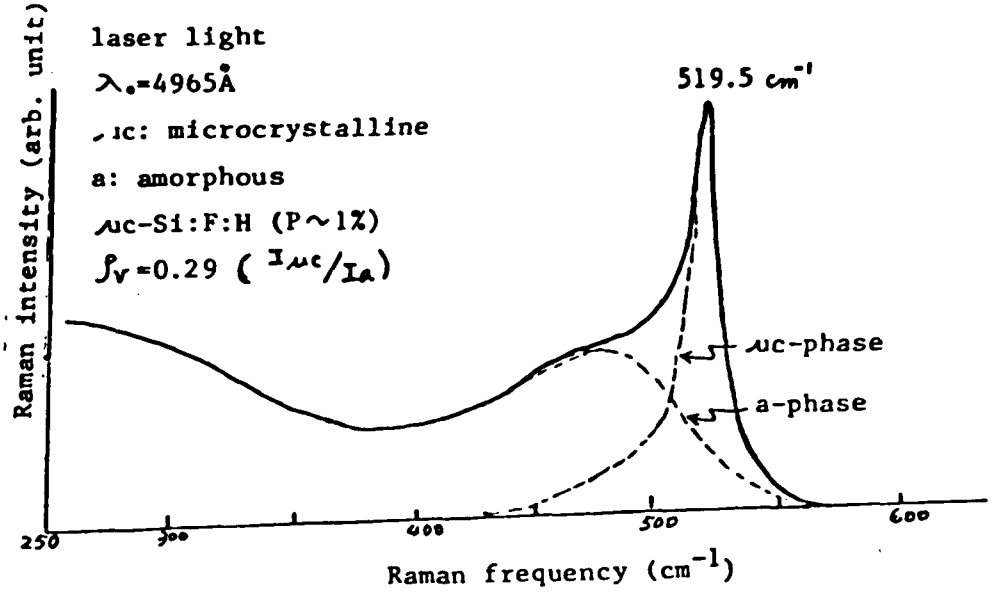

Fig.(3.2.2c) Two component deconvolution of Raman spectrum for μc-Si:F:H alloys. (Ref.27)

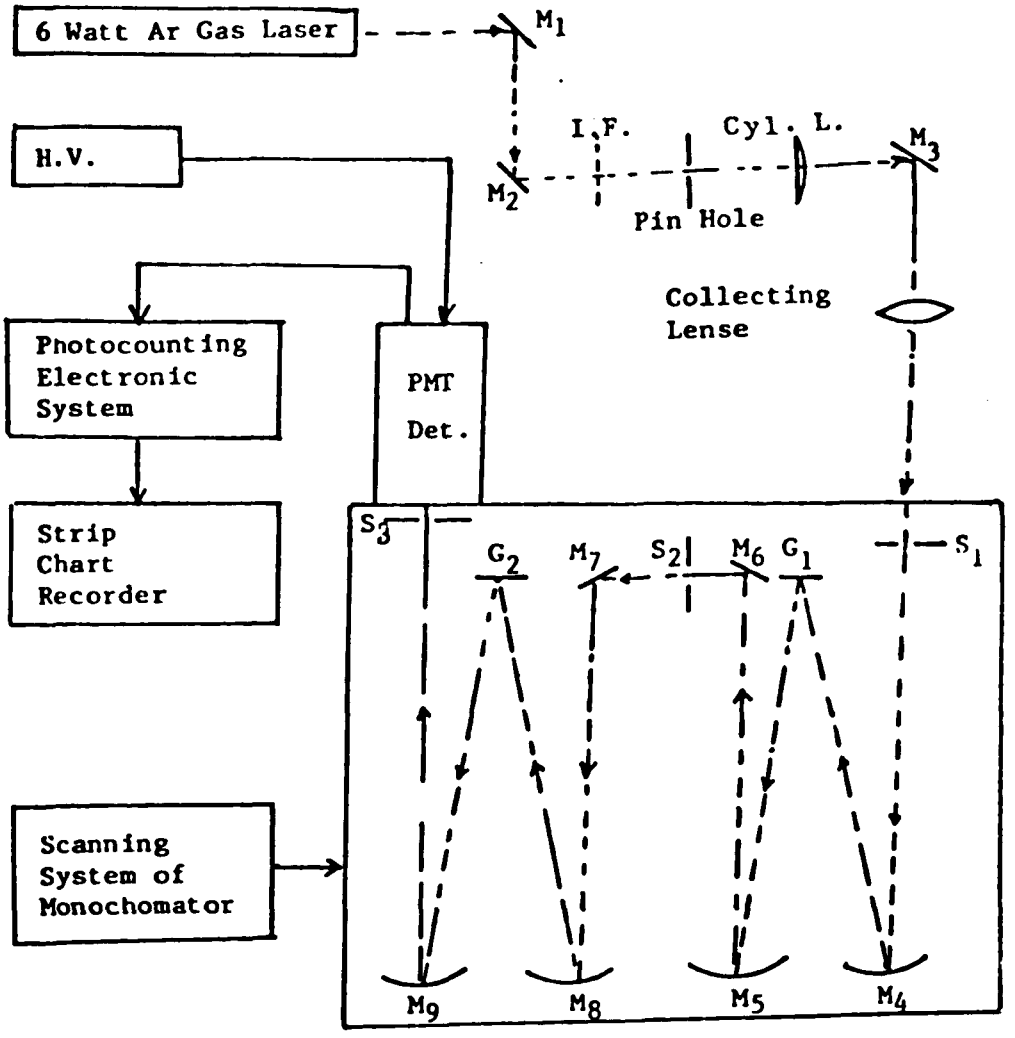

Double Grating Spectrometer

Fig.(3.2.3) Schematic functional block diagram of Raman scattering apparatus.

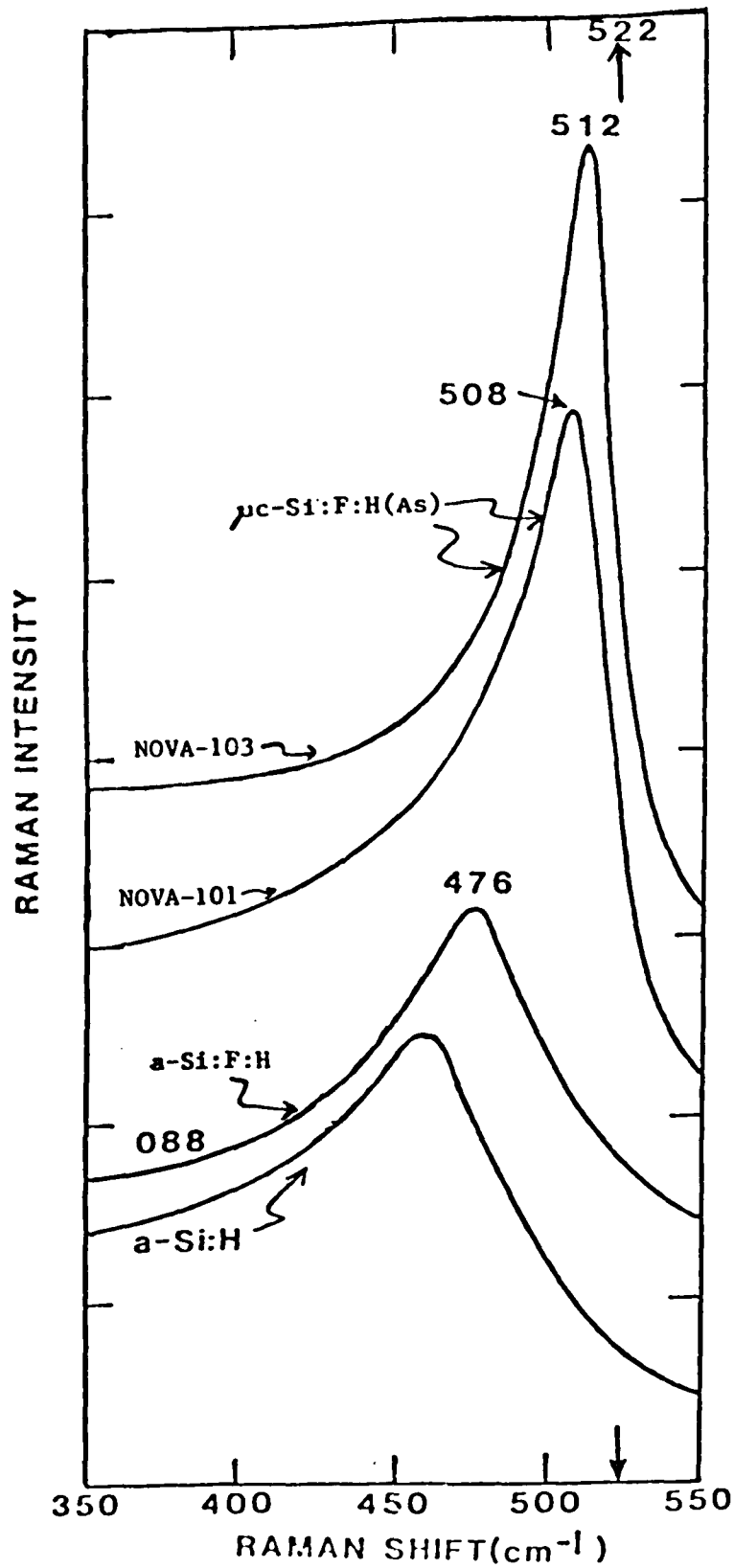

Fig.(3.2.4) Raman spectra of a-Si:H and μc-Si:F:H alloys.

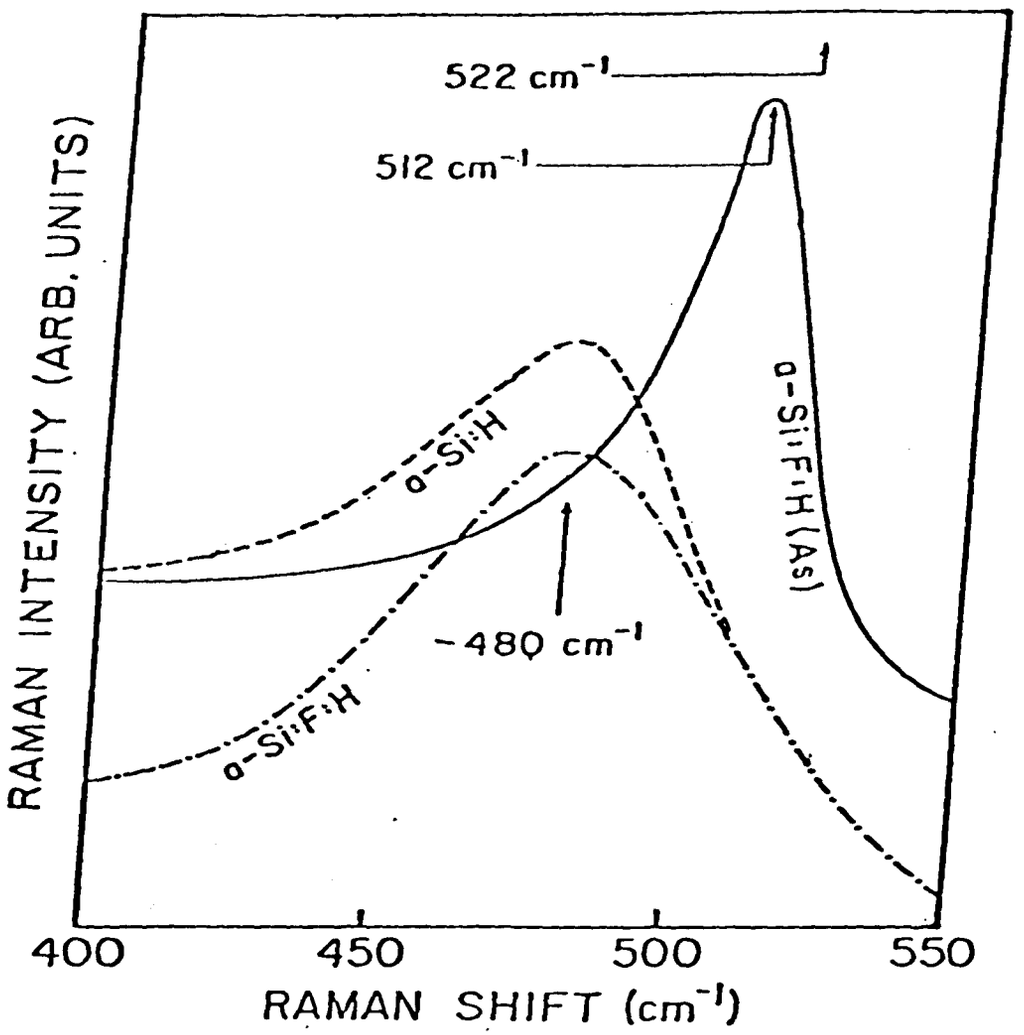

Fig.(3.2.5) Experimental Raman scattering spectra for the specimen a-Si:H, a-Si:F:H and a-Si:F:H(As). (Ref. 27)

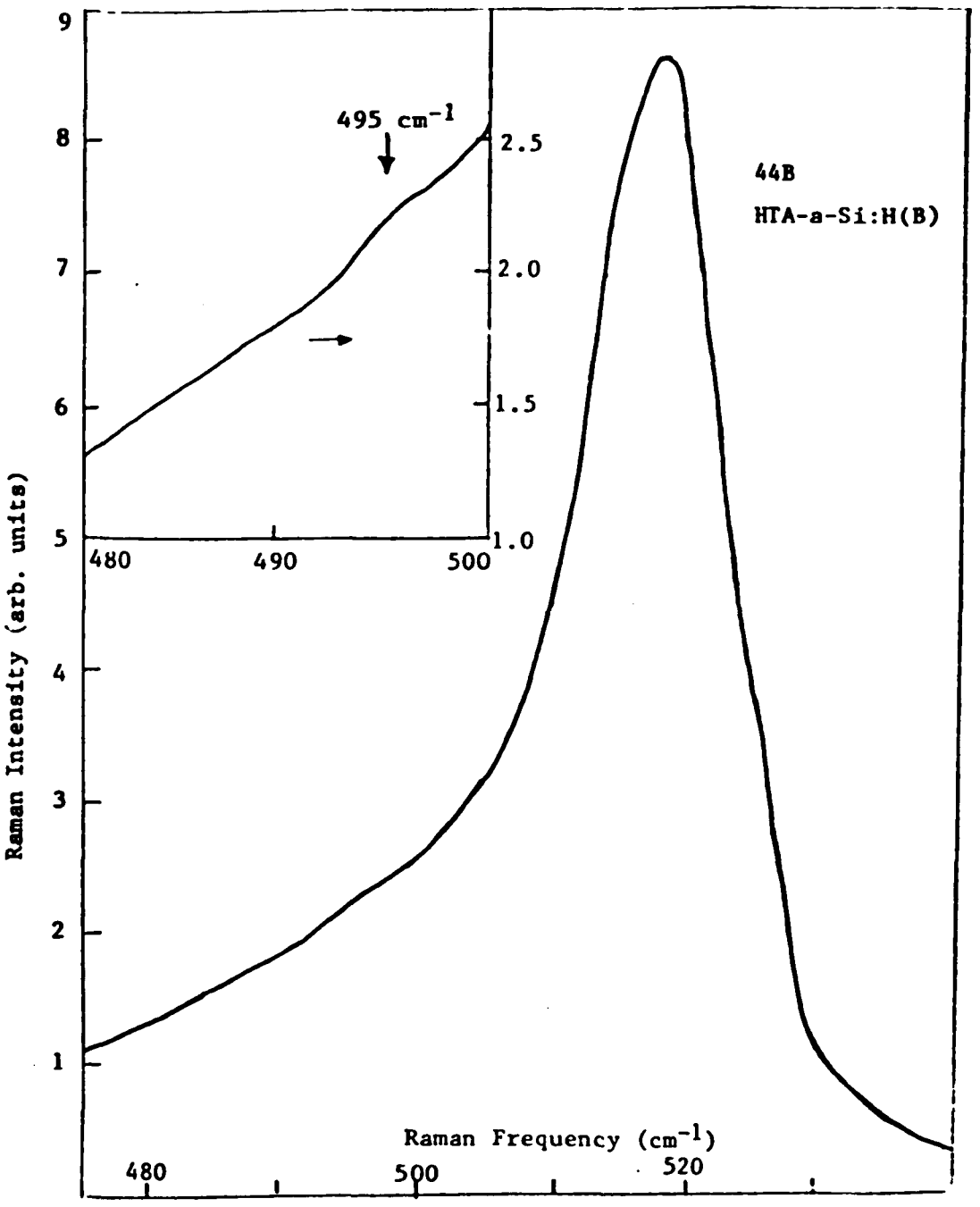

Fig.(3.2.6) Raman spectra of high temperature thermally annealed a-Si:H(B) sample. HTA-a-Si:H(B) sample with 50 ppm Boron is annealed at temperature 1100 °C about 10 min.. Peak position is at 517 cm^{-1}. Details of the spectra in the region between 480 - 500 cm^{-1}, which shows a small shoulder around 495 cm^{-1}, is displayed in the insert.

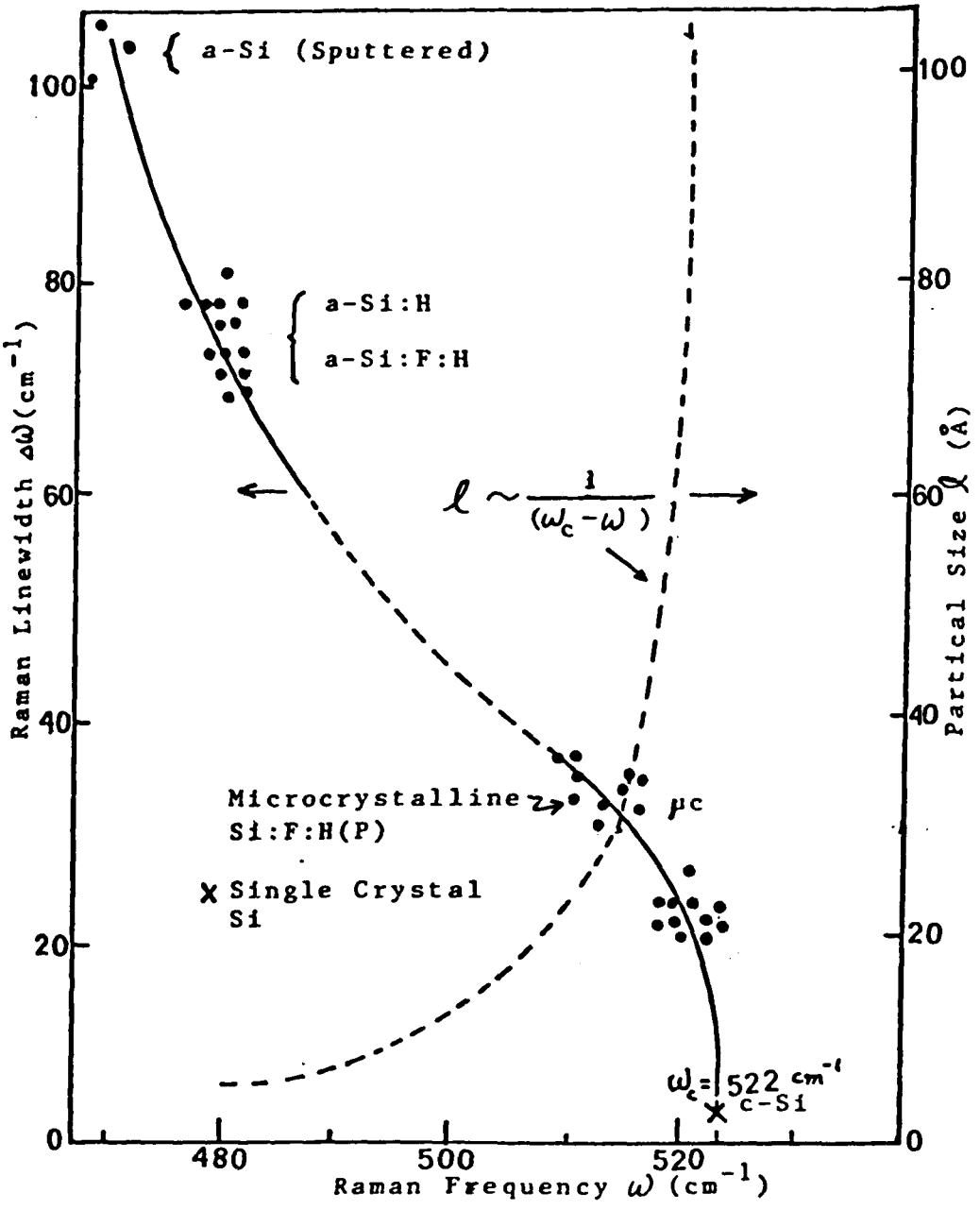

Fig.(3.2.7) Raman width and particle size (dashed) versus Raman frequency for μc-Si (including a-Si). (Ref.28)

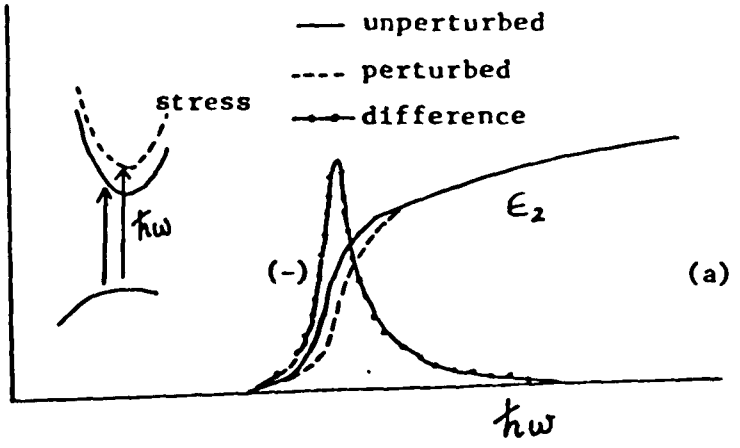

Fig.(3.3.1a) A schematic diagram of the change in the imaginary part of the dielectric function expected for first-derivative modulation process.

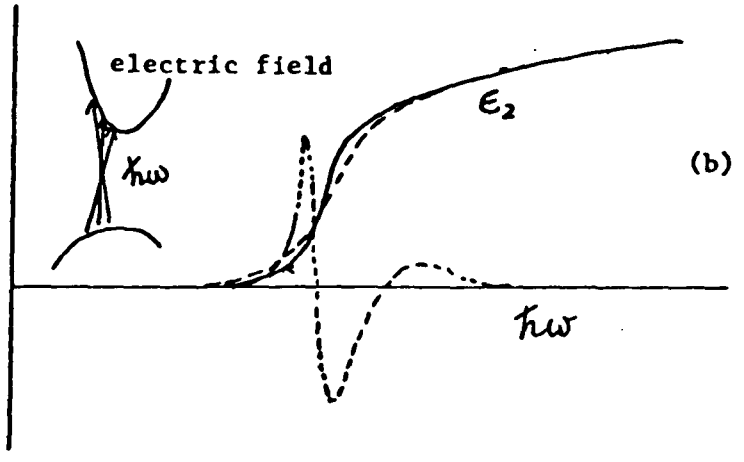

Fig.(3.3.1b) A schematic diagram of the change in the imaginary part of the dielectric function expected for electric field modulation. (Ref. 34)

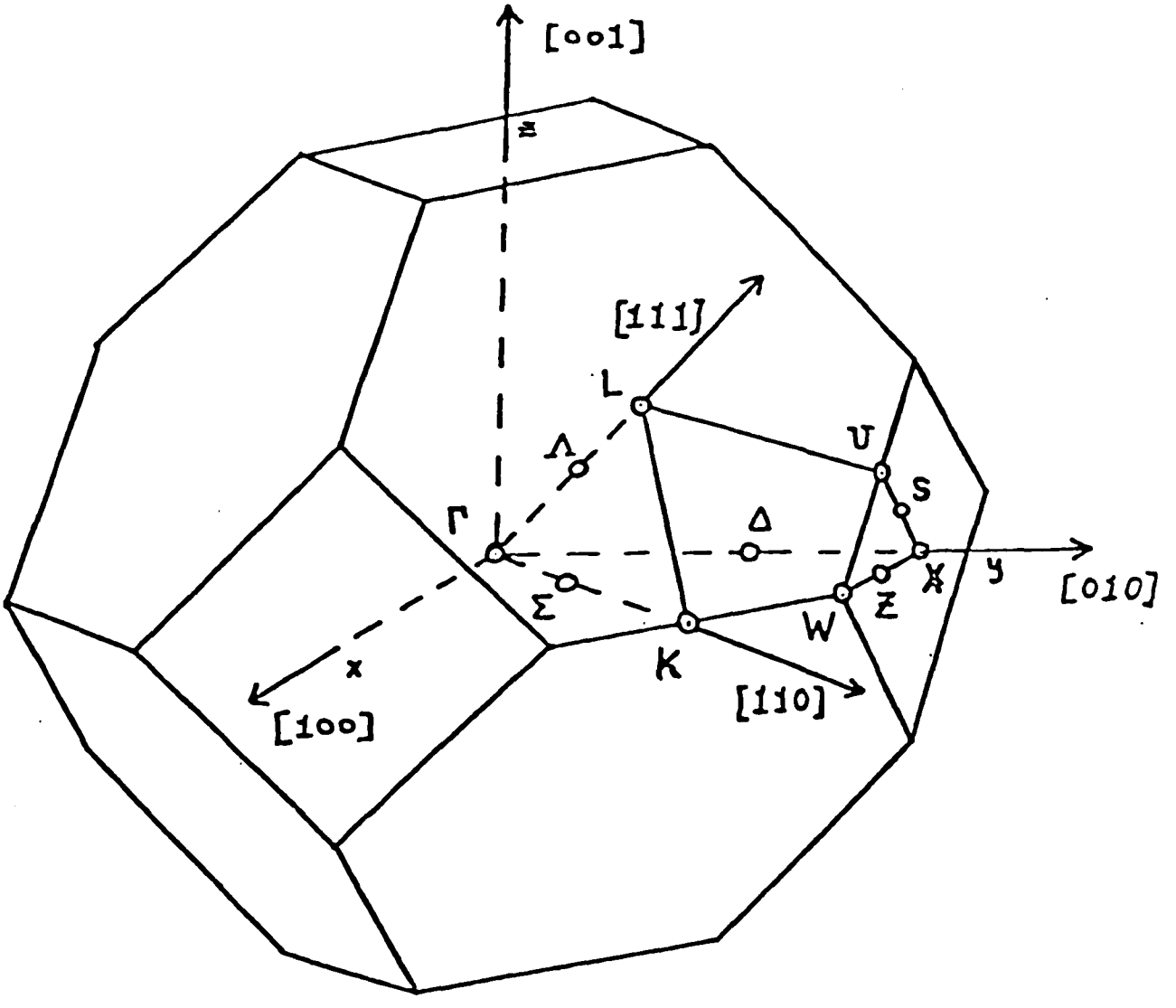

Fig.(3.3.2) First Brillouin zone for a face centered cubic crystal. The high symmetry lines and points are labeled.

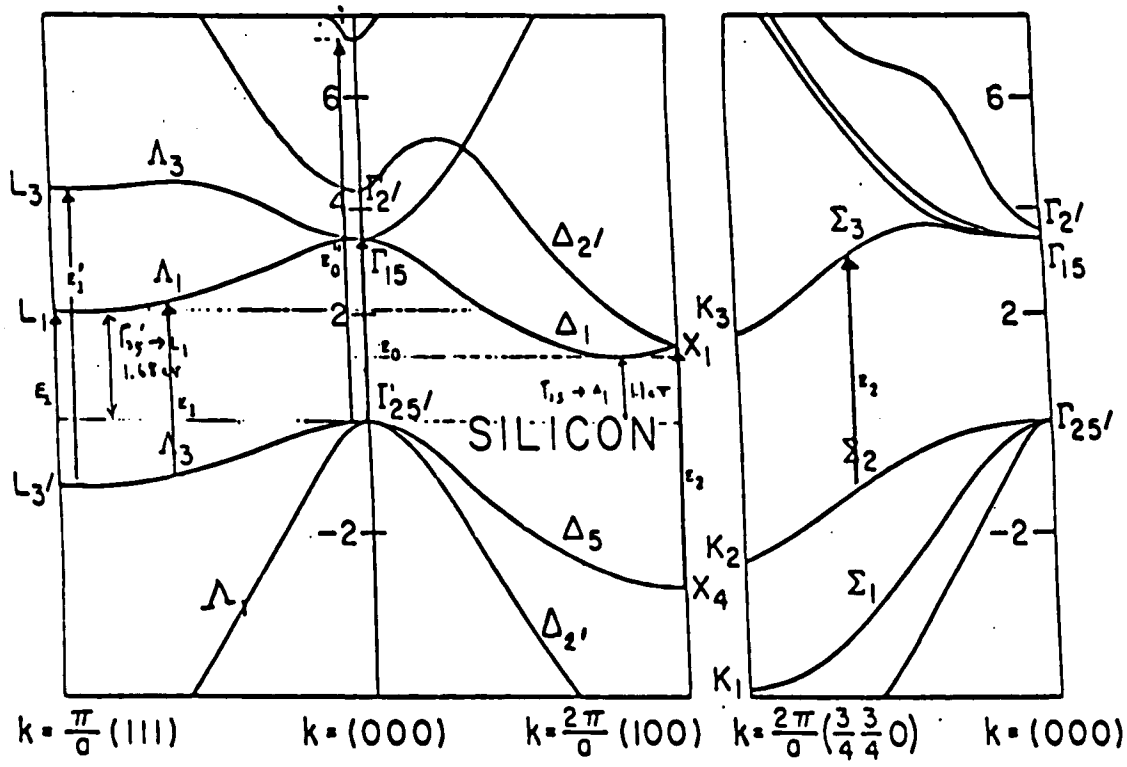

Fig.(3.3.3) Band structure of crystalline silicon.
(Ref. 87)

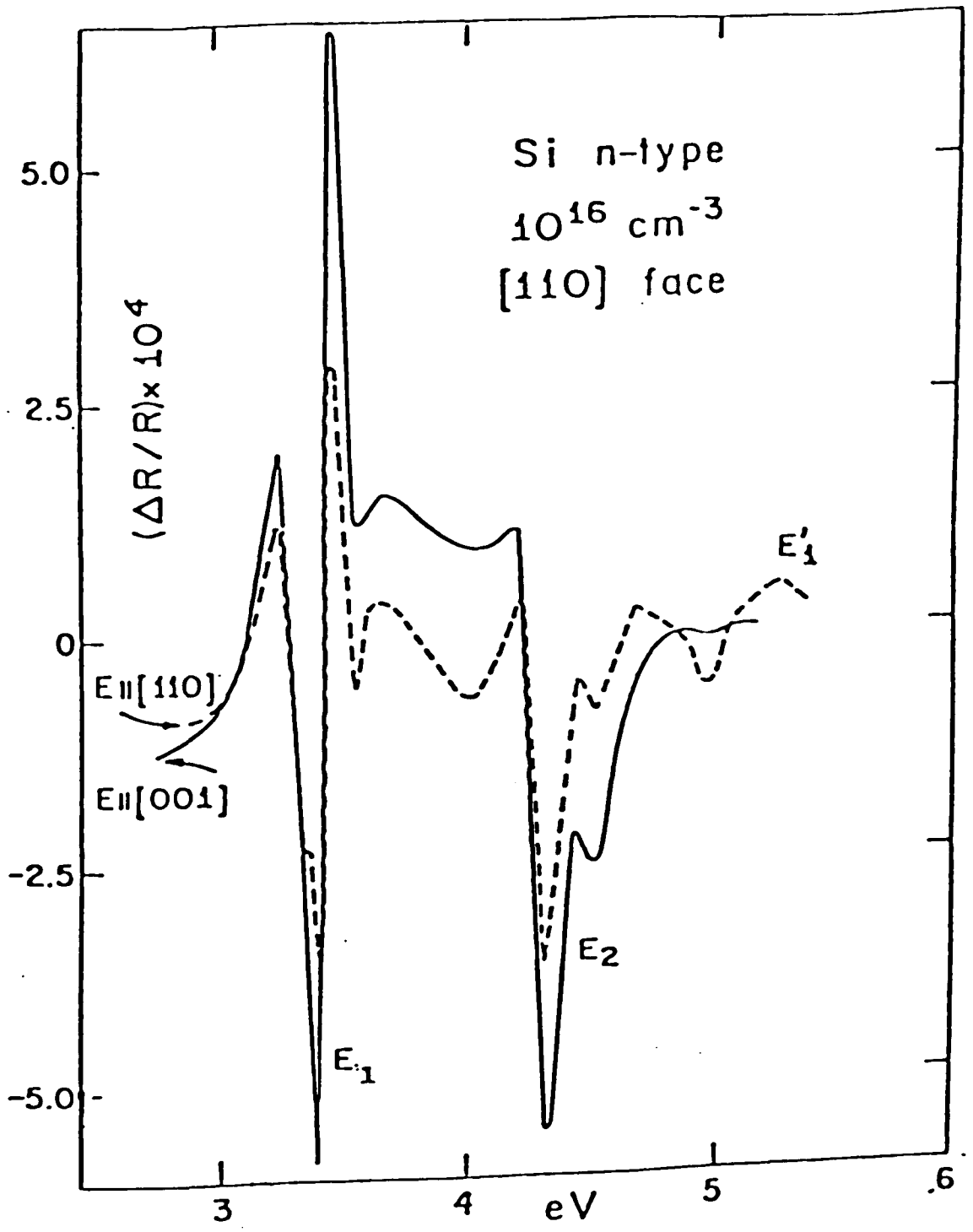

Fig.(3.3.4) Typical EER (Electrolyte Electroreflectance) spectrum of n-type c-Si. (Ref. 88)

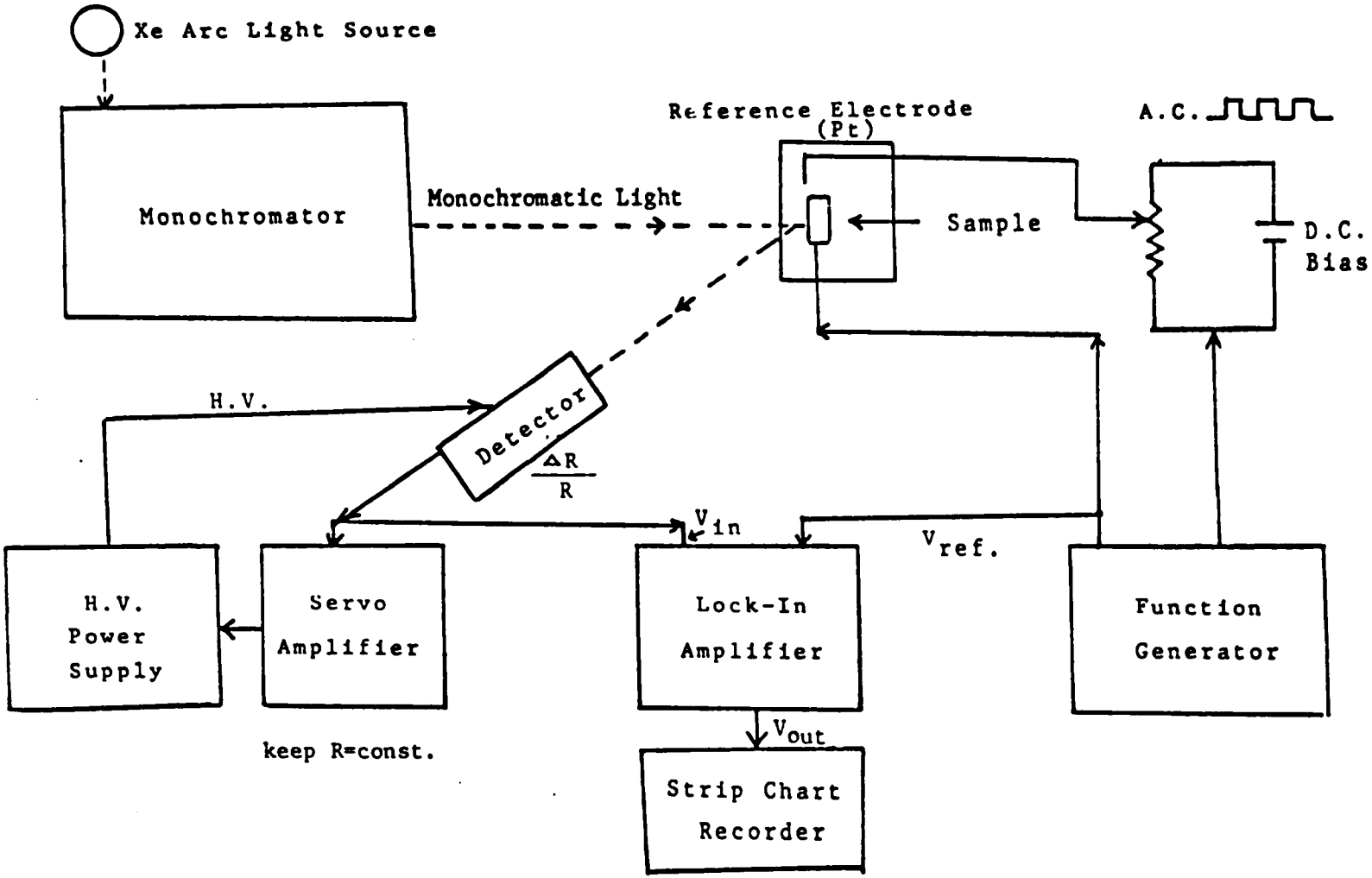

Fig.(3.3.5) Schematic functional block diagram of EER set up.

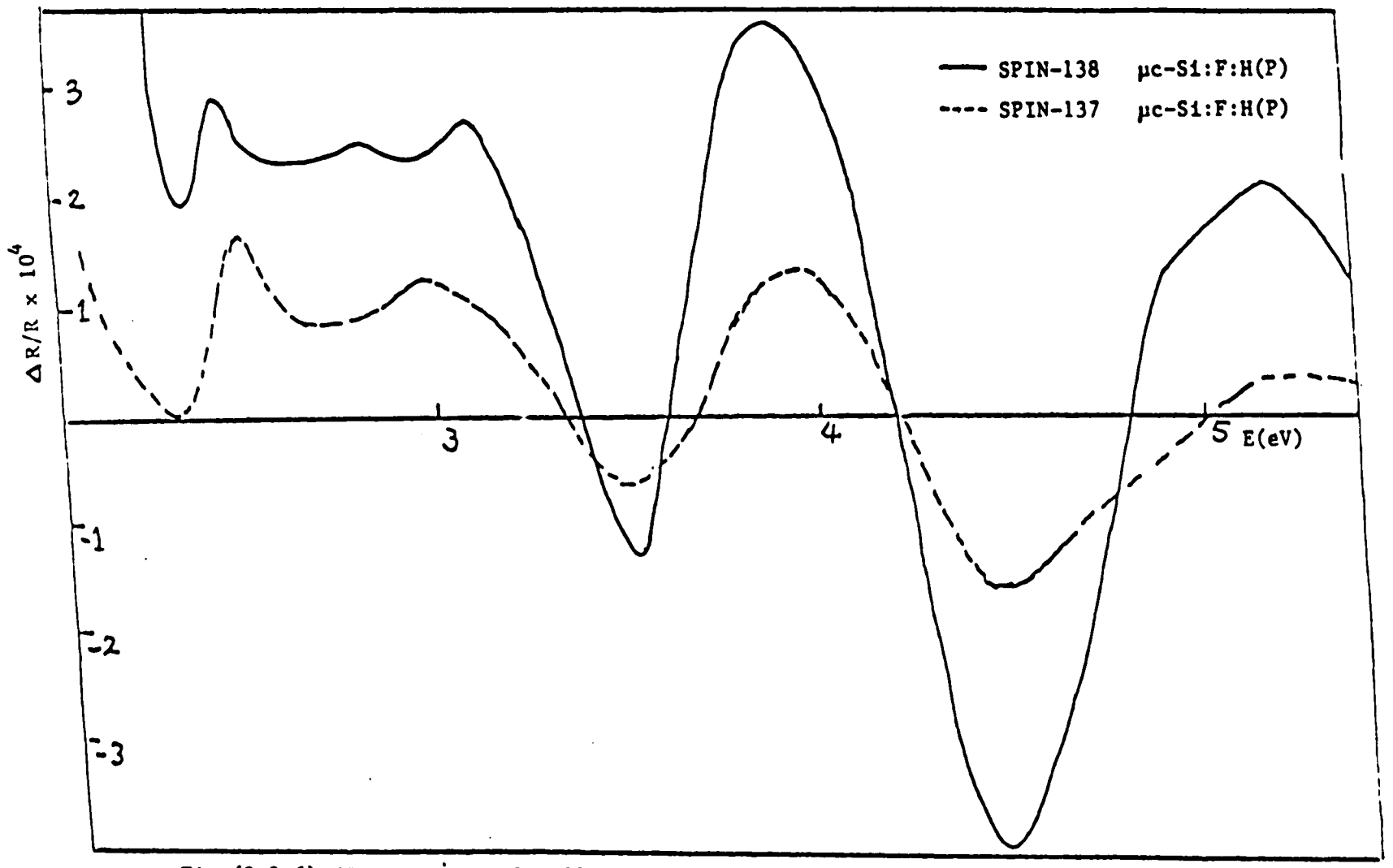

Fig.(3.3.6) EER spectrum of different concertration of P-doped μc-Si:F:H alloys.

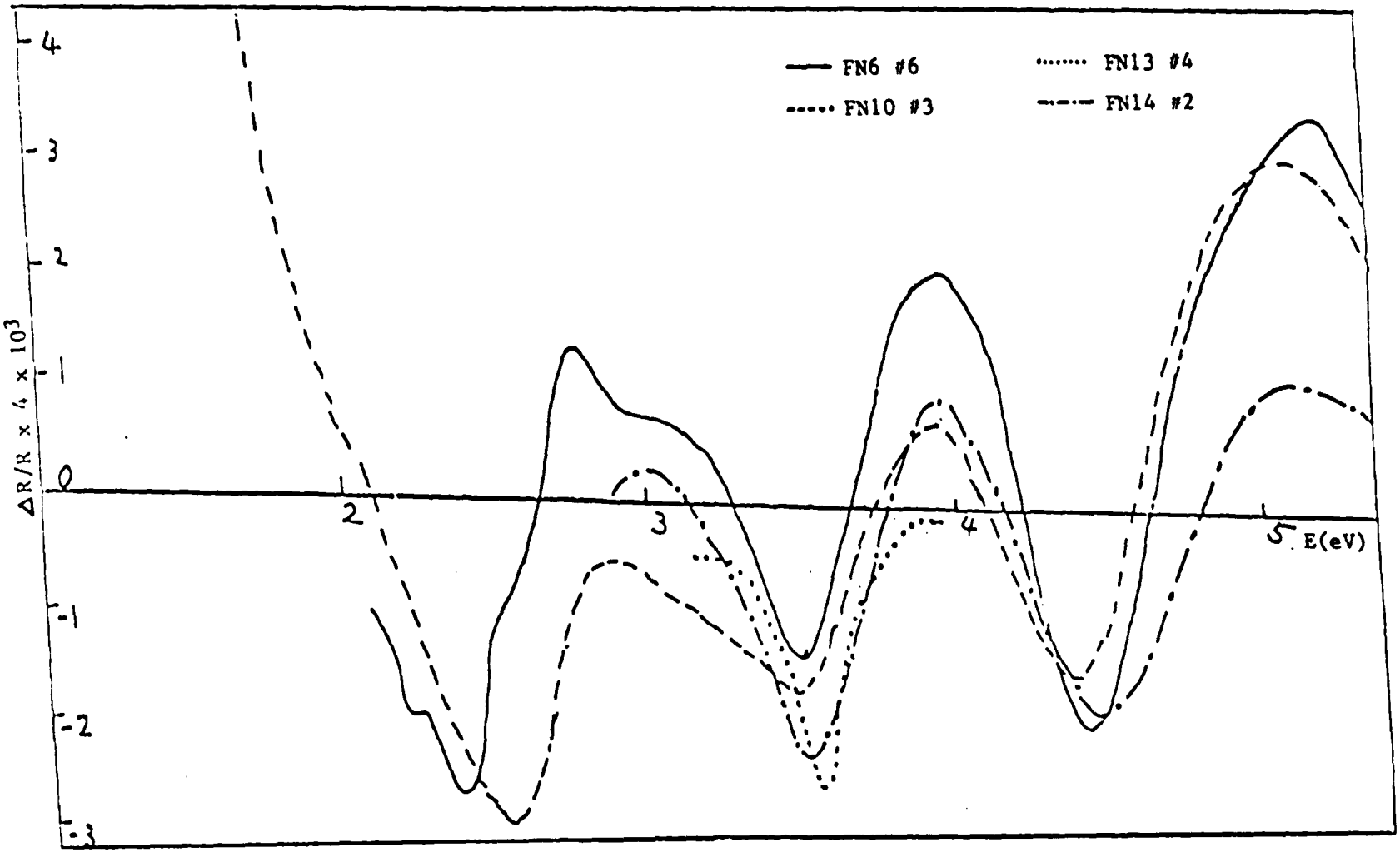

Fig.(3.3.7) EER spectra of heavily P-doped uc-Si:F:H alloys which was deposited on stainless steel or glass substrate. (Ref. 28)

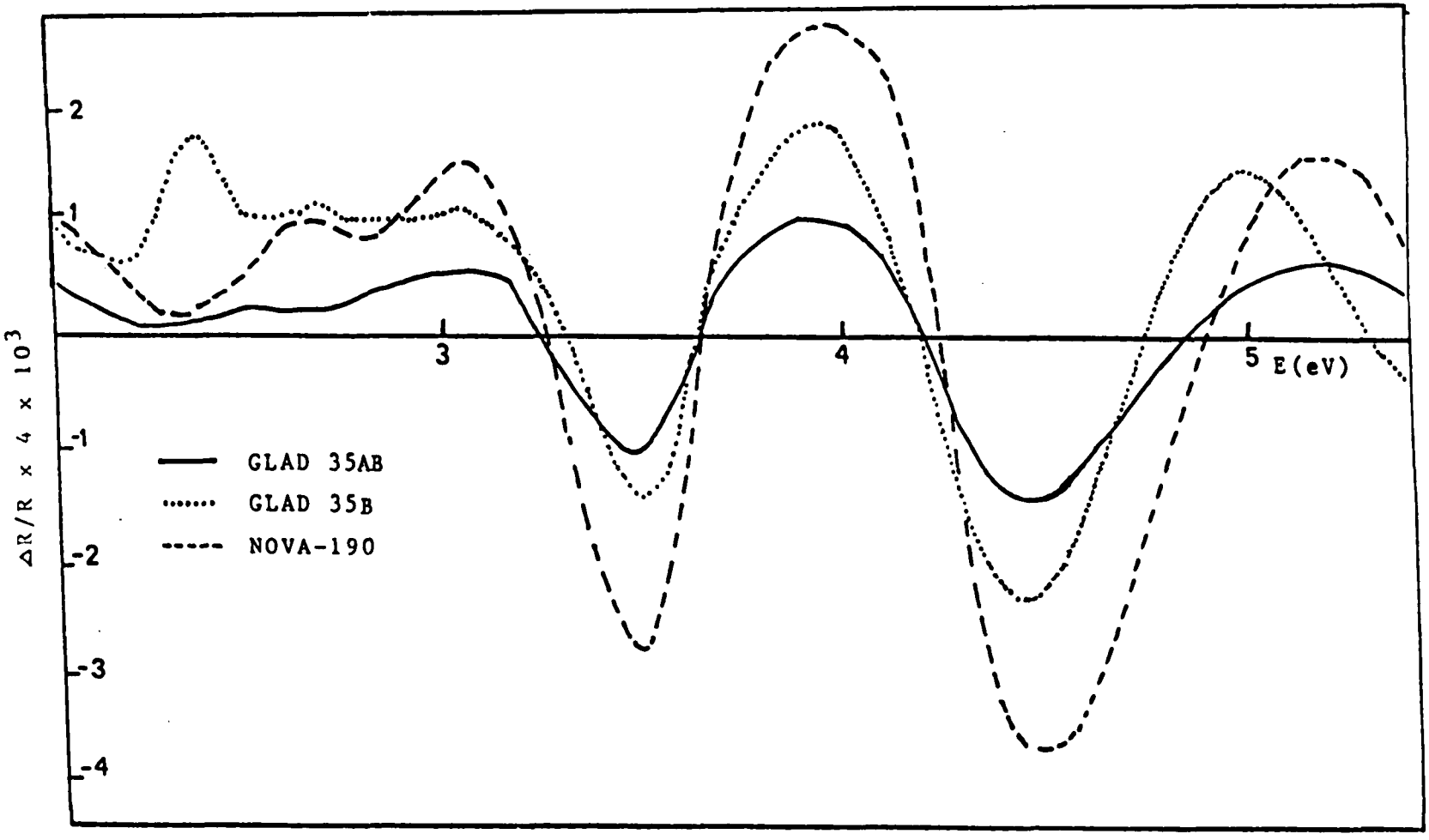

Fig.(3.3.8) EER spectra of P-doped μc-Si:F:H and As-doped μc-Si:F:H alloys. (Ref. 27)

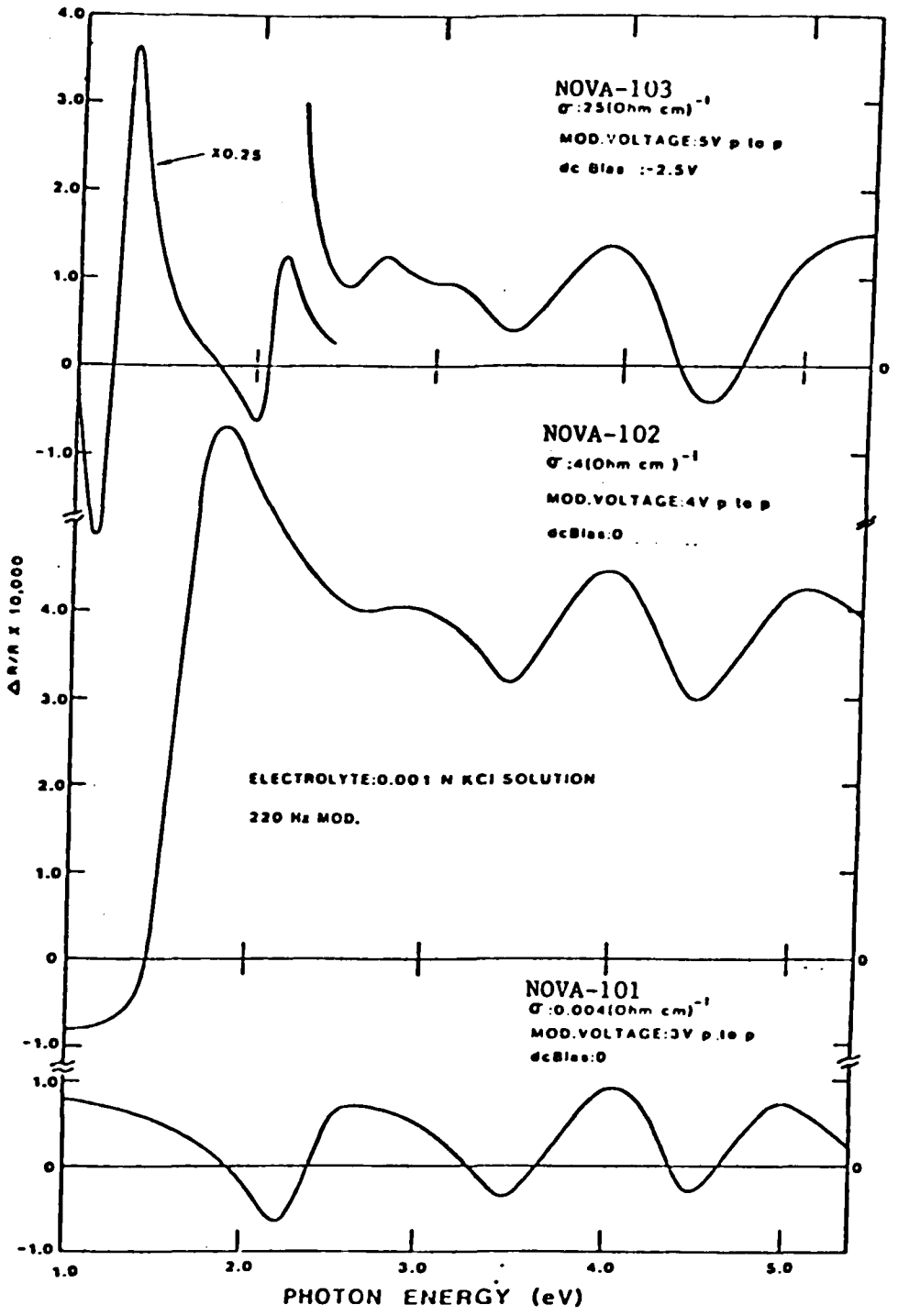

Fig.(3.3.9) EER spectra of different concentration of As-doped μc-Si:F:H alloys (NOVA-101, NOVA-102, NOVA-103). (Ref. 26)

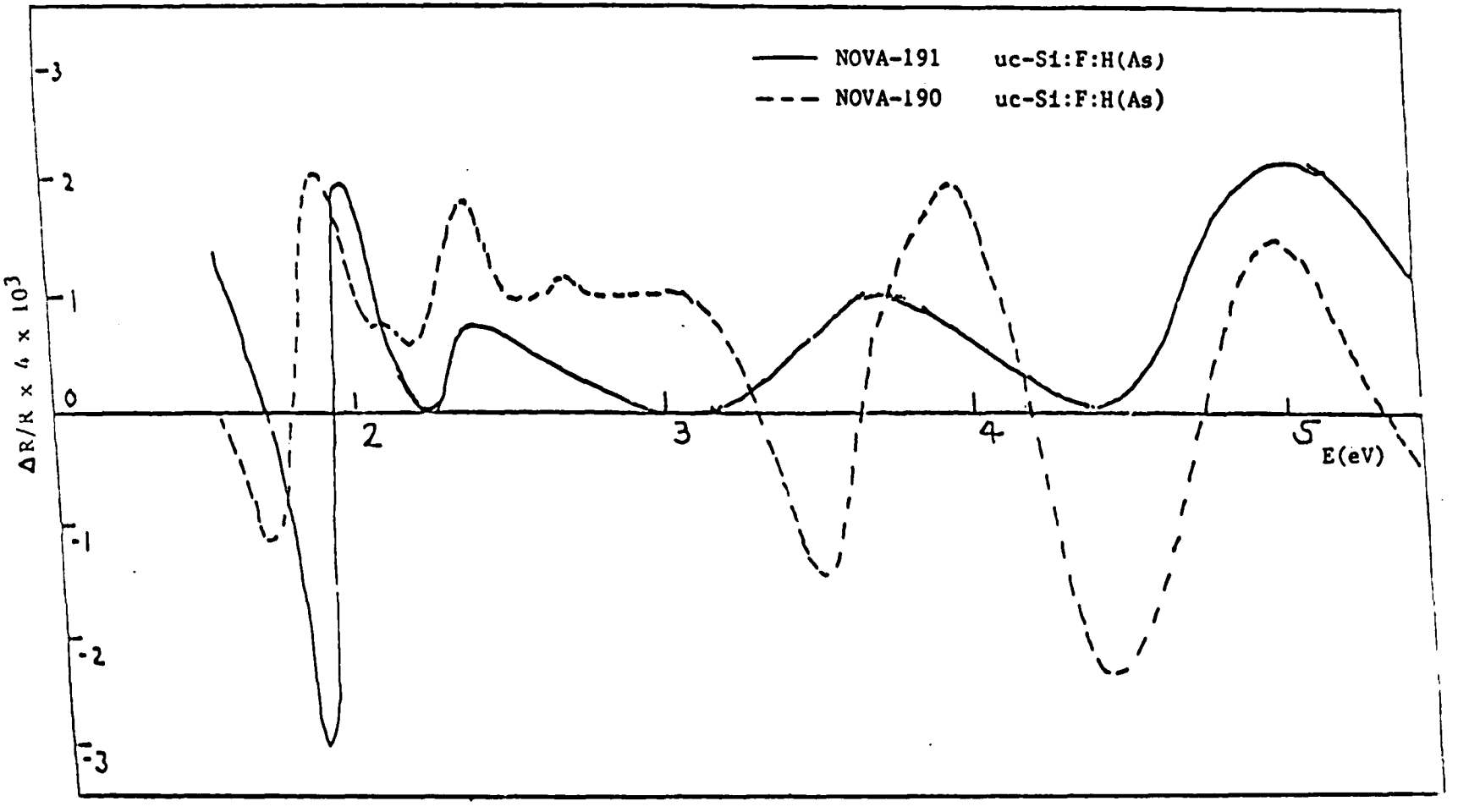

Fig.(3.3.10) EER spectra of different cincentration of As-doped uc-Si:F:H alloys (NOVA-190 and NOVA-191).

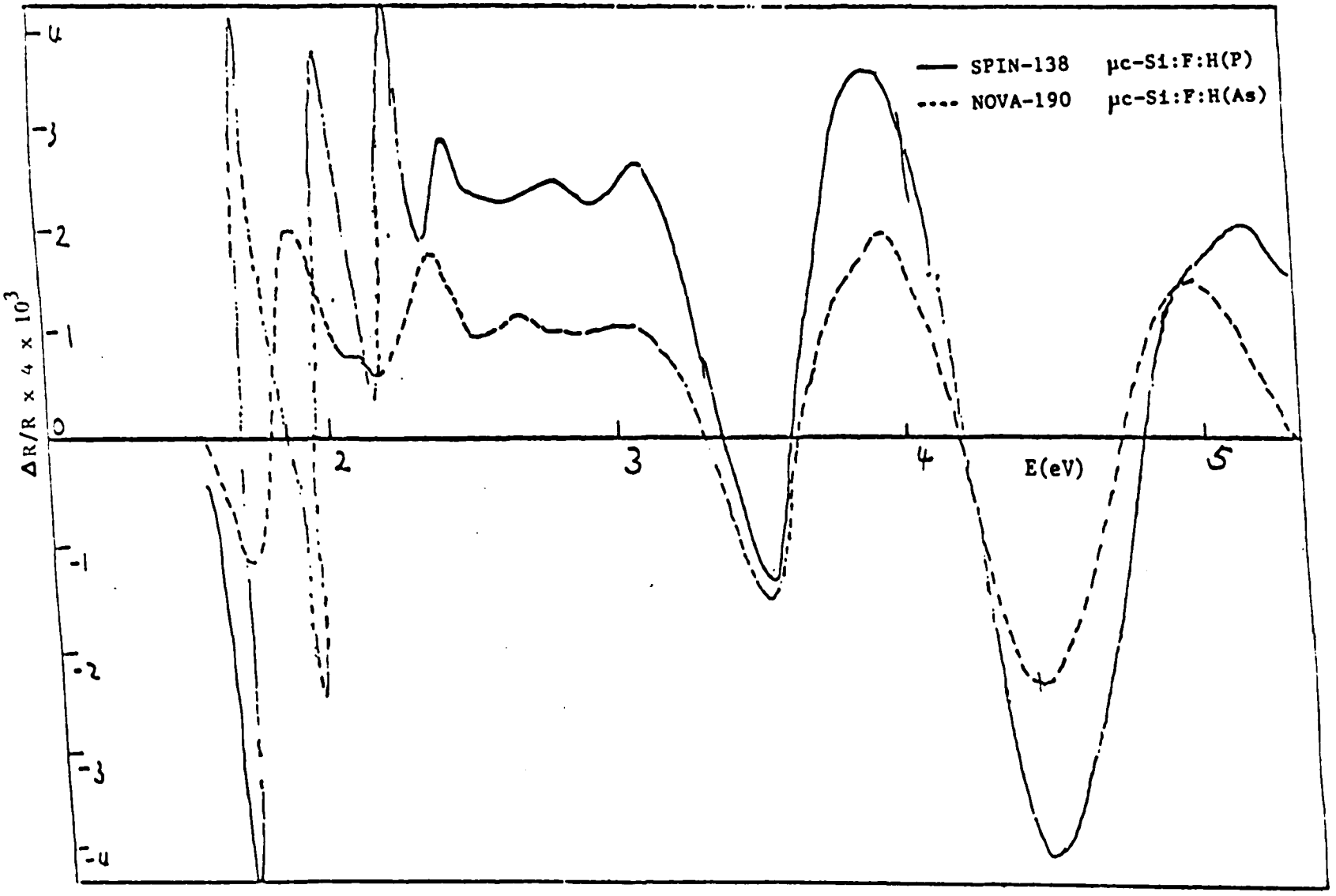

Fig.(3.3.11) Comparision of EER spectra for P-doped and As-doped uc-As:F:H alloys.

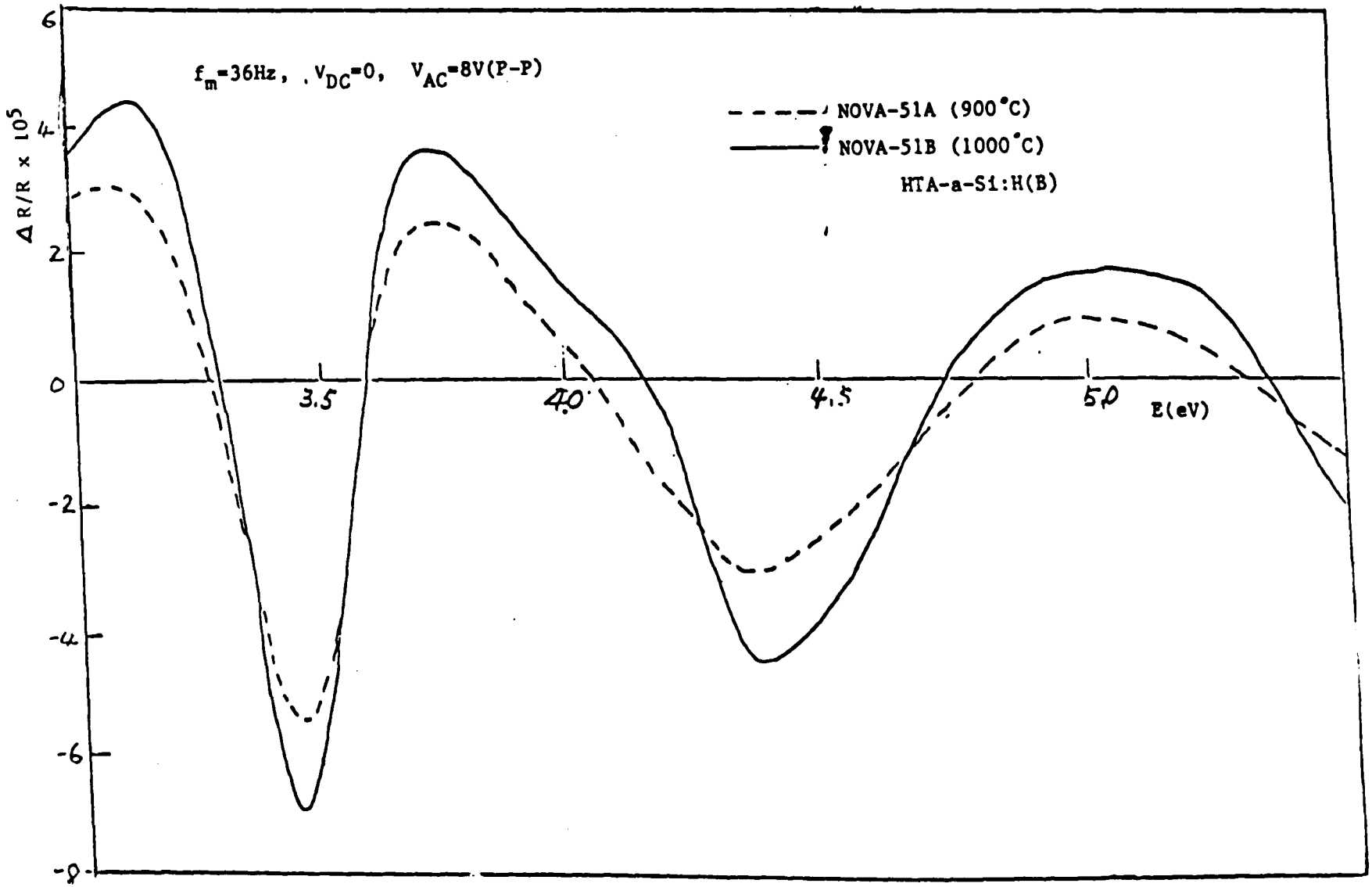

Fig.(3.3.12) EER spectra of HTA-a-Si:H(B) samples with different annealing temperatyre.

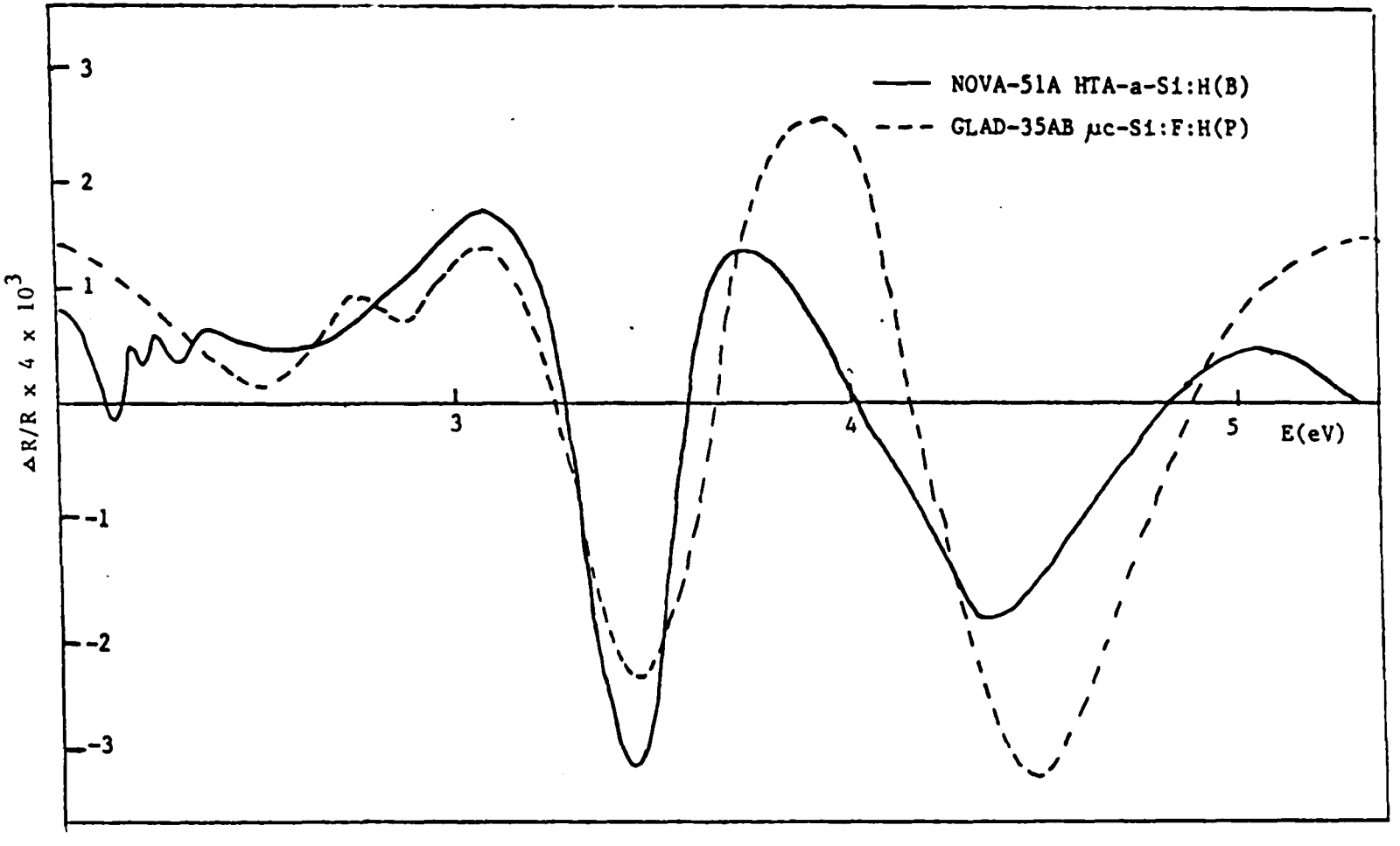

Fig.(3.3.13) Comparision of EER spectra of HTA-a-Si:H(B) and μc-Si:F:H(P) samples.

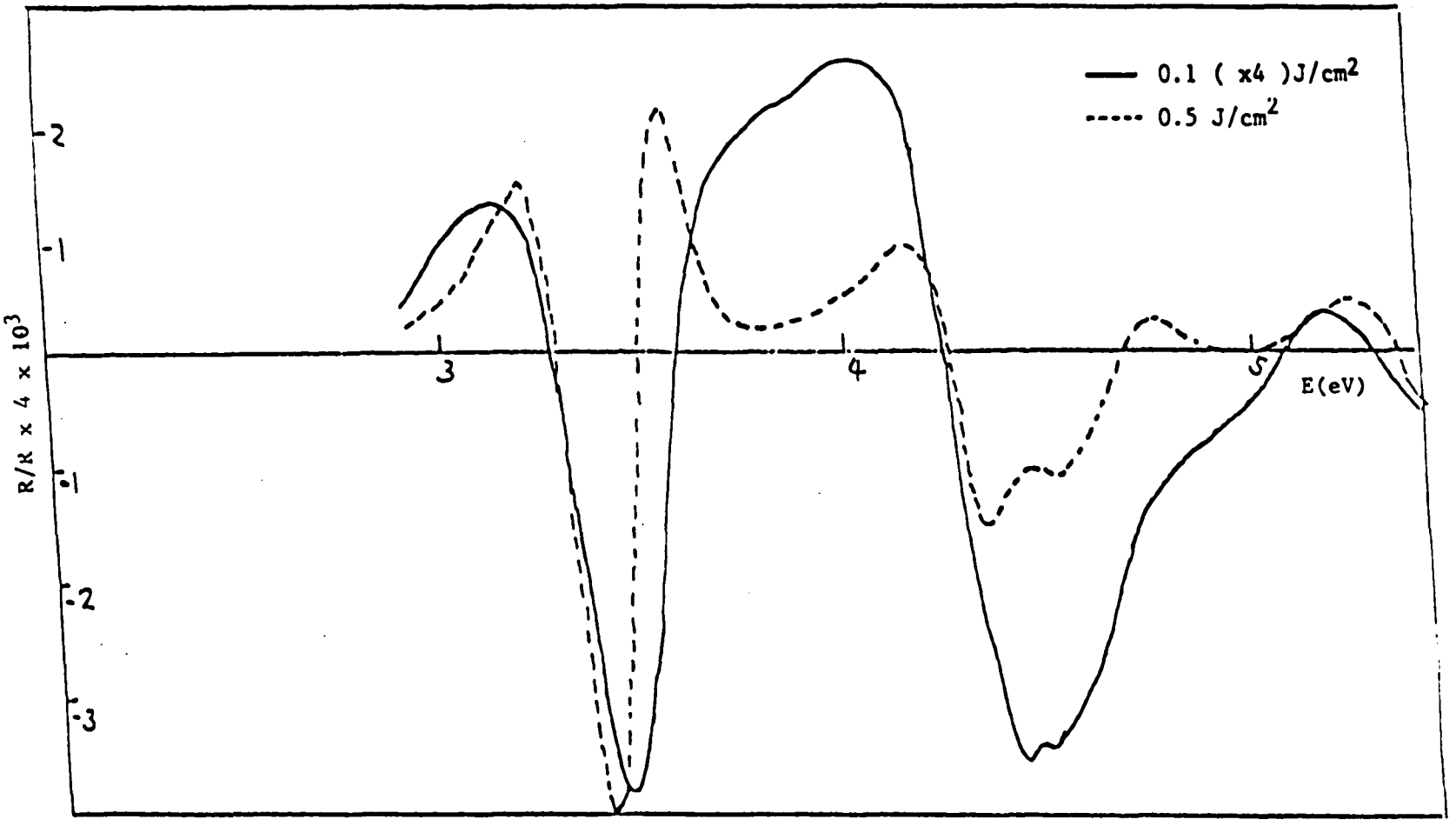

Fig.(3.3.14) EER spectra of ion demaged (100 Kev Si), laser annealed Si with different energy density.

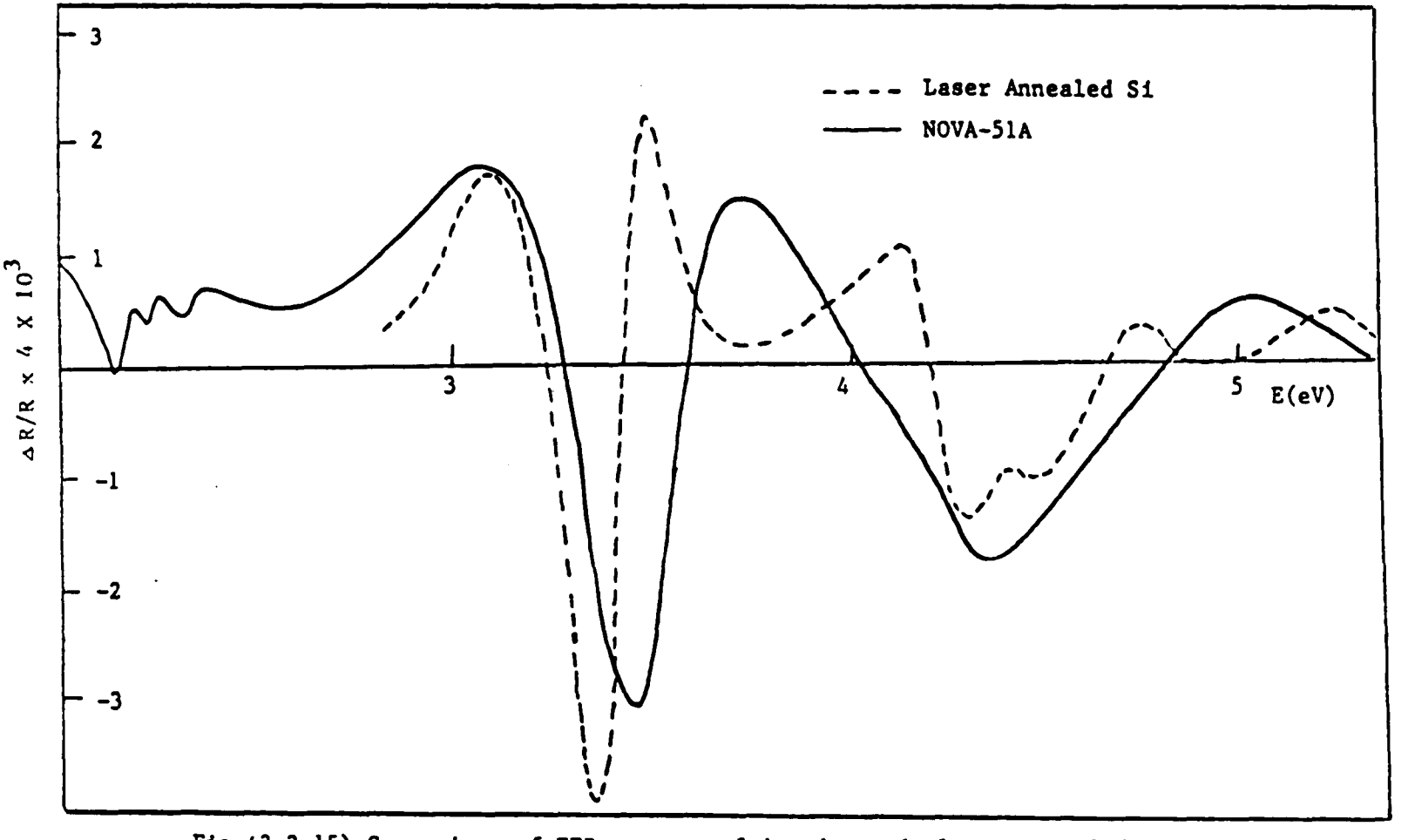

Fig.(3.3.15) Comparison of EER spectra of ion-damaged, laser-annealed Si with laser energy density 0.5 J/cm^2 and HTA-a-Si:H(B) samples.

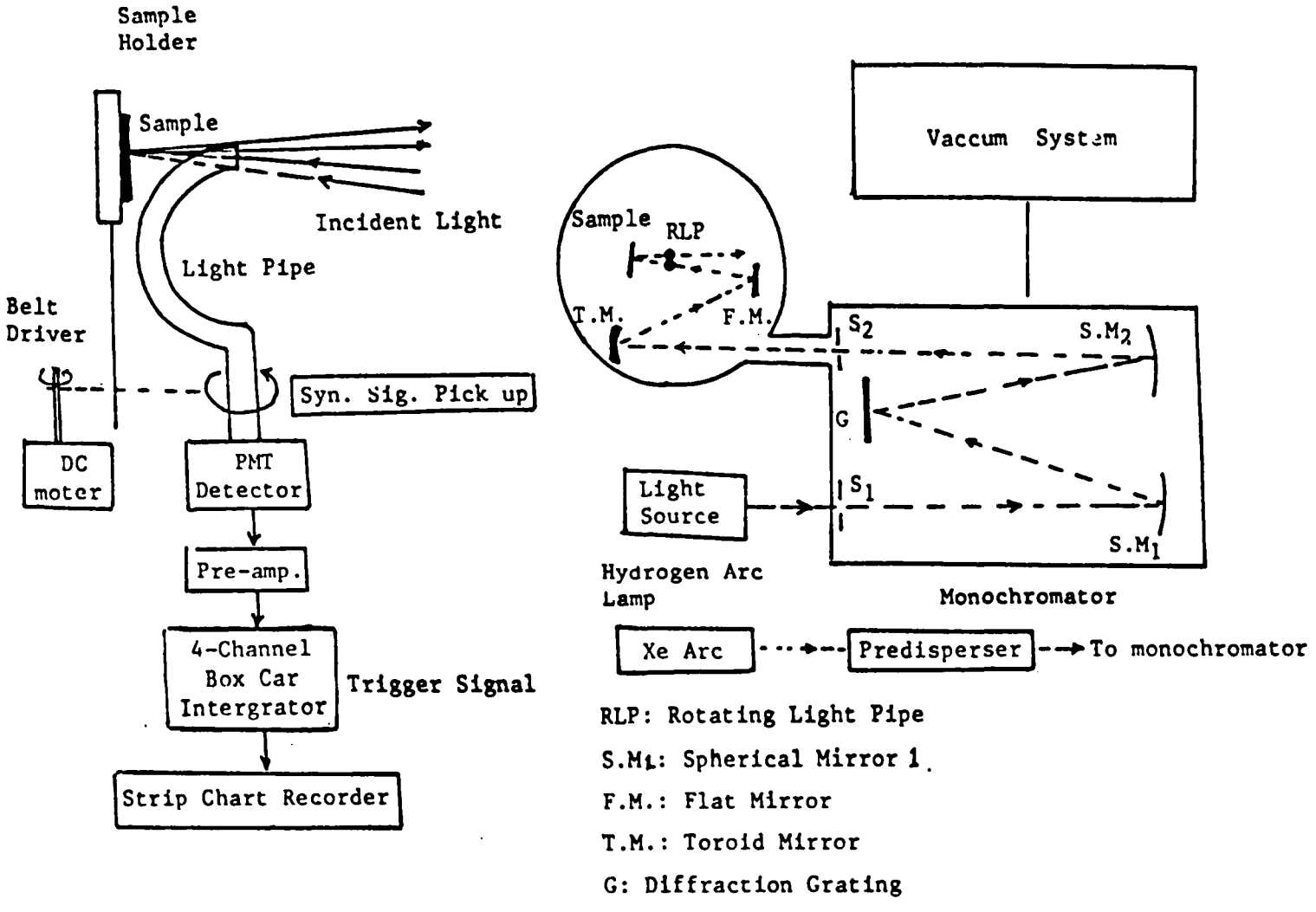

Fig.(3.4.1) Schematic functional block diagram of rotating light pipe reflectometer. (Ref. 41)

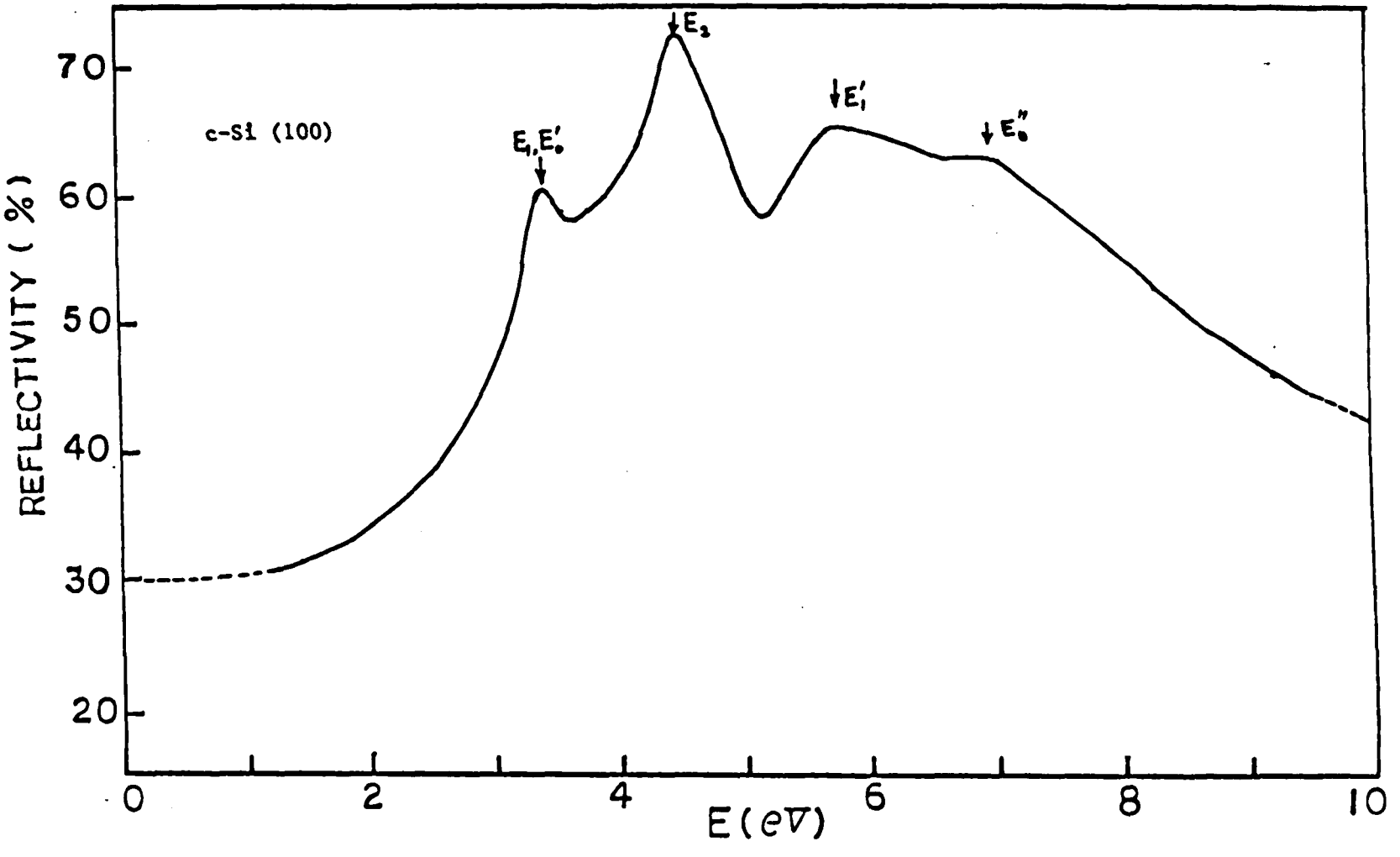

Fig.(3.4.2) The reflectance spectra of c-Si from 1 eV to 10 eV using rotating light pipe reflectometer at near normal incidence.

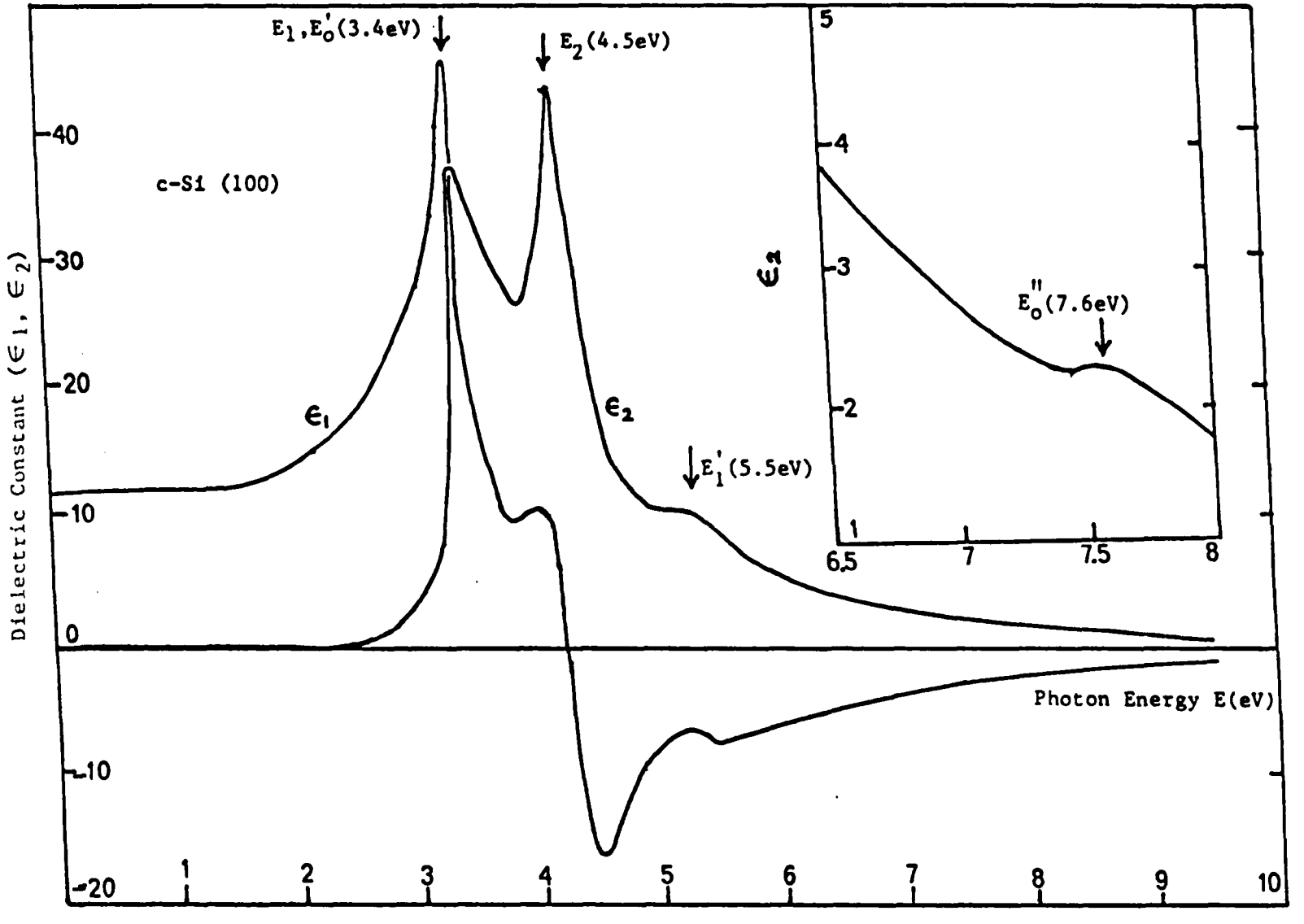

Fig.(3.4.3) The real part $\epsilon_1(\omega)$ and the imaginary part $\epsilon_2(\omega)$ of the dielectric function of c-Si.

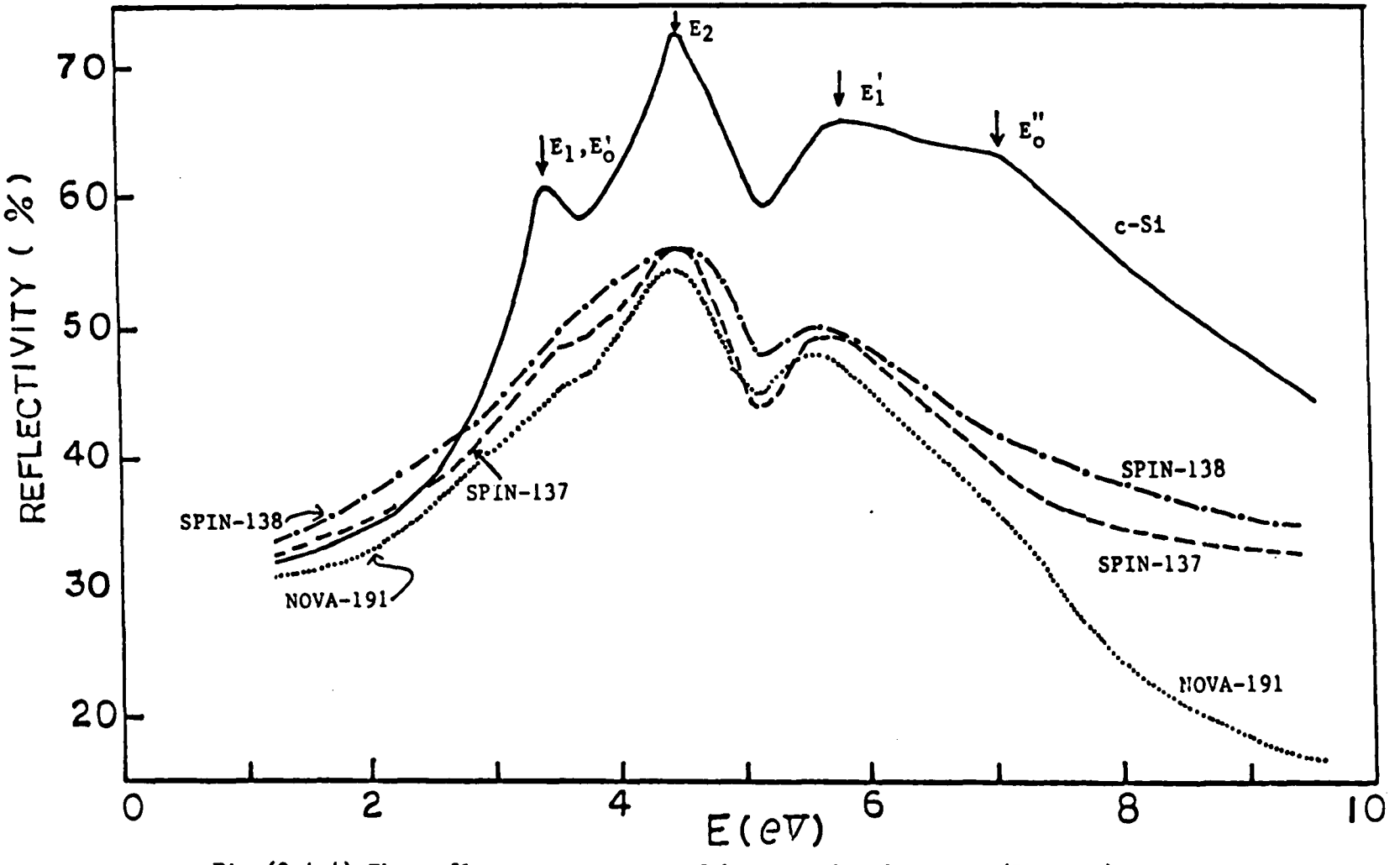

Fig.(3.4.4) The reflectance spectra of heavily doped n-type (P or As) μc-Si:F:H alloys and c-Si.

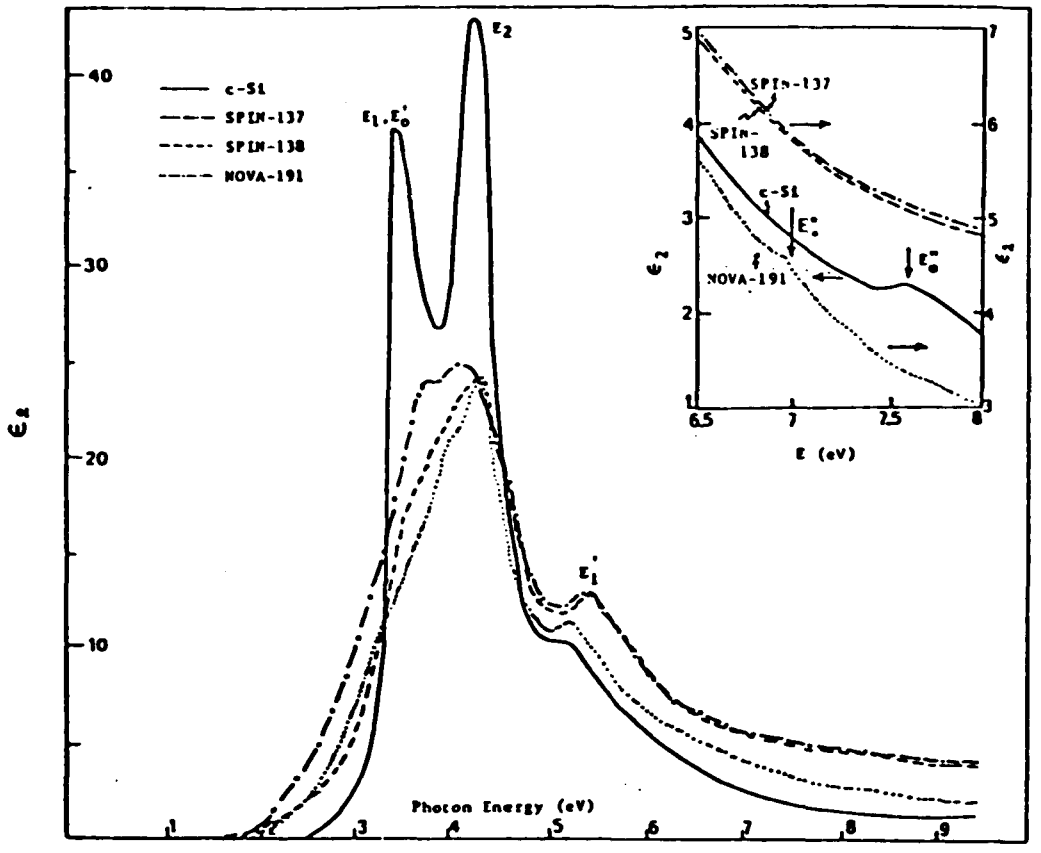

Fig.(3.4.5) The imaginary part $\epsilon_2(\omega)$ of the dielectric function for heavily doped n-type a-Si:F:H alloys.

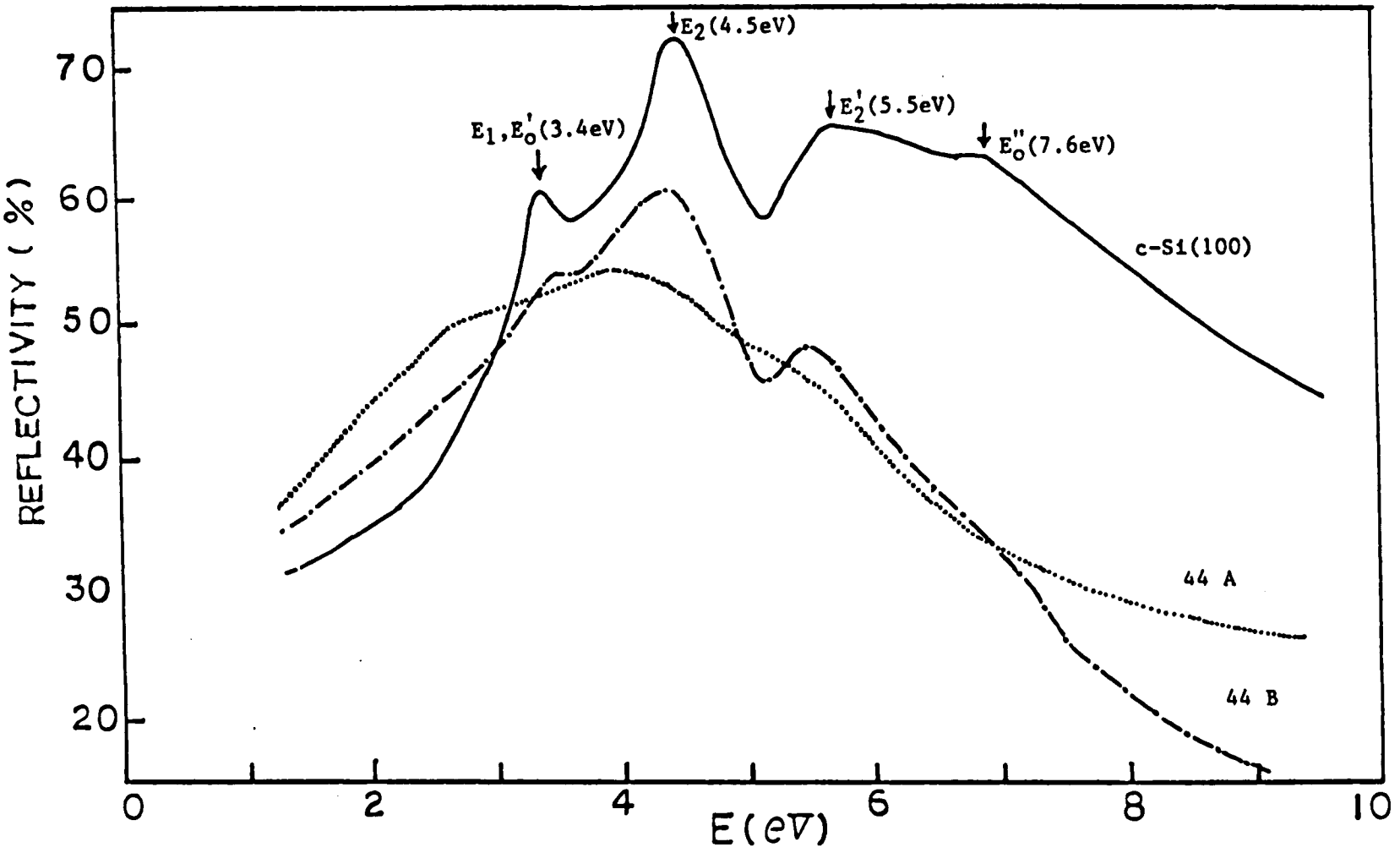

Fig.(3.4.6) The reflectance spectra for HTA-a-Si:H(B), unannealed Si:H(B) and c-Si.

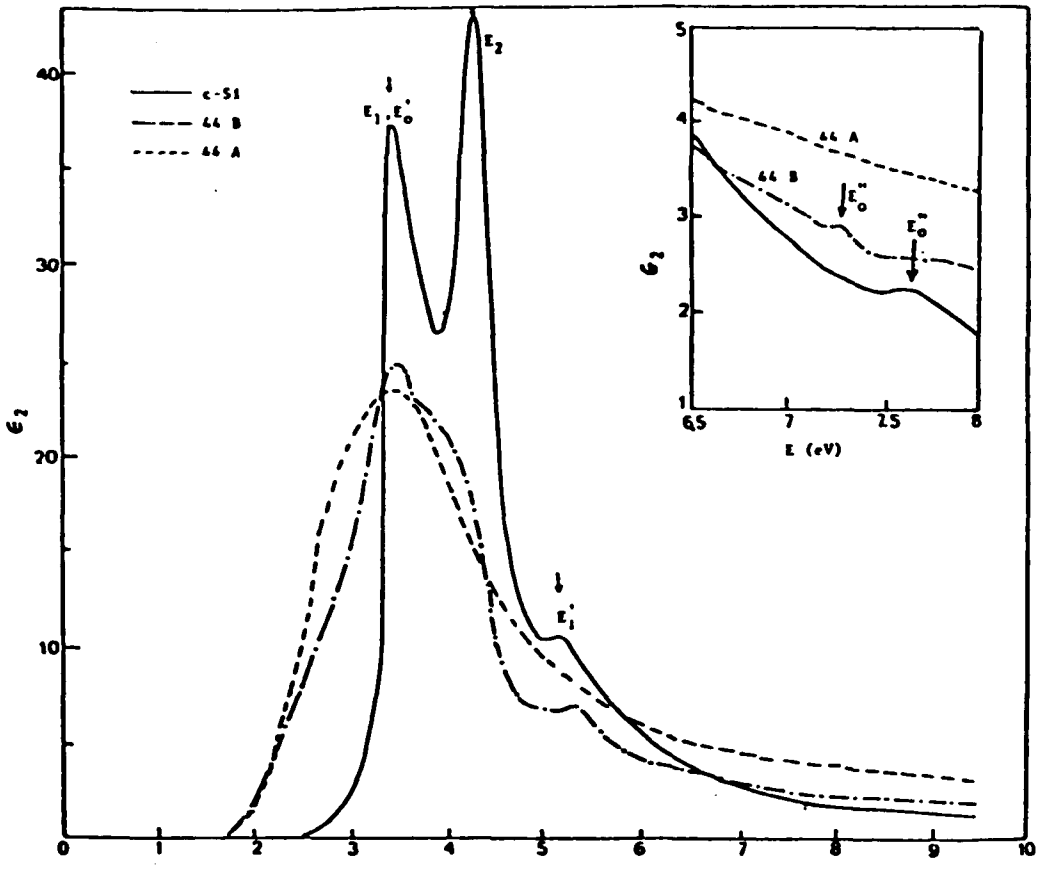

Fig.(3.4.7) The imaginary part $\epsilon_2(\omega)$ of the dielectric function for HTA-a-Si:H(B), unannealed Si:H(B) and c-Si.

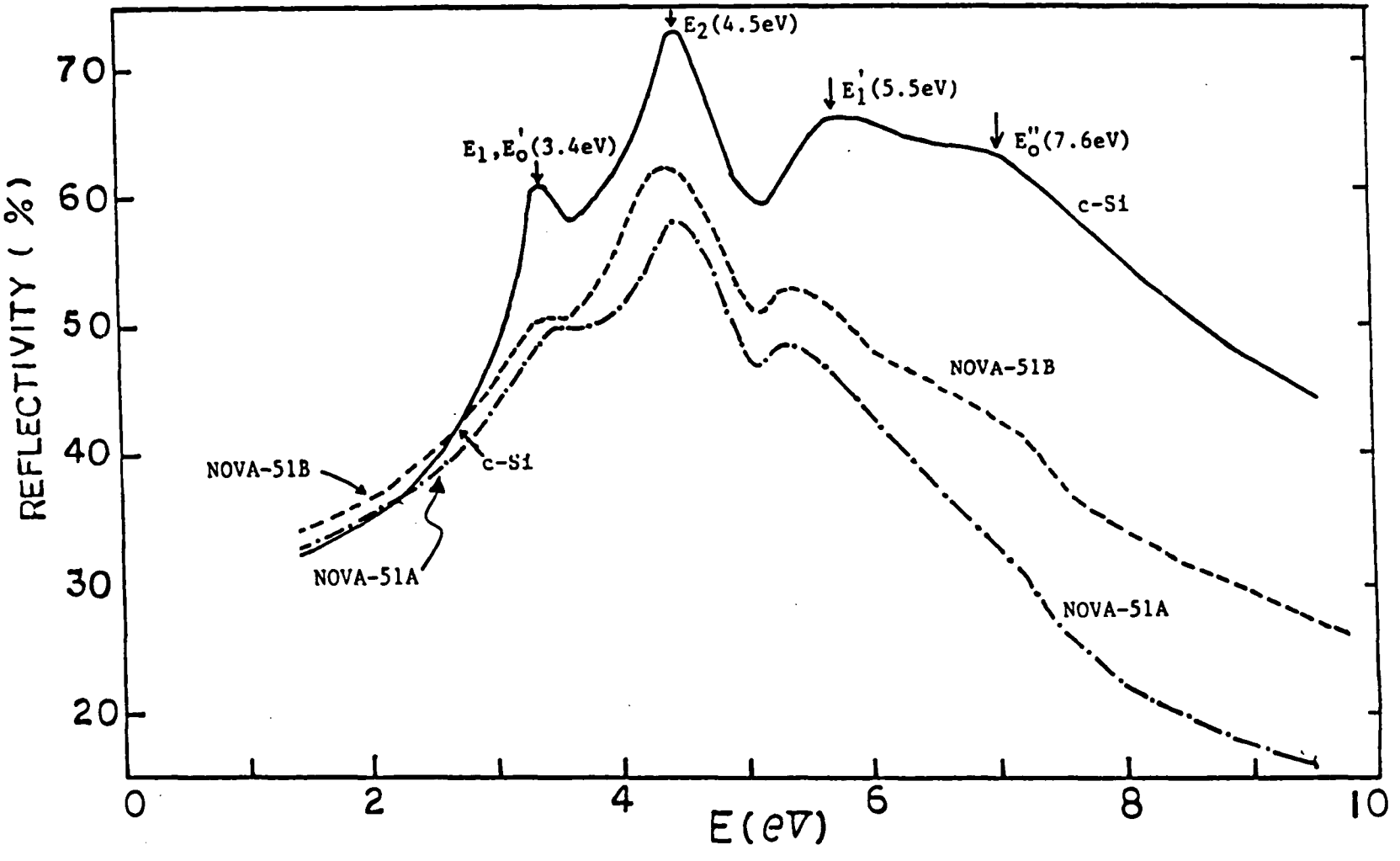

Fig.(3.4.8) The reflectance spectra for HTA-a-Si:H(B) and c-Si.

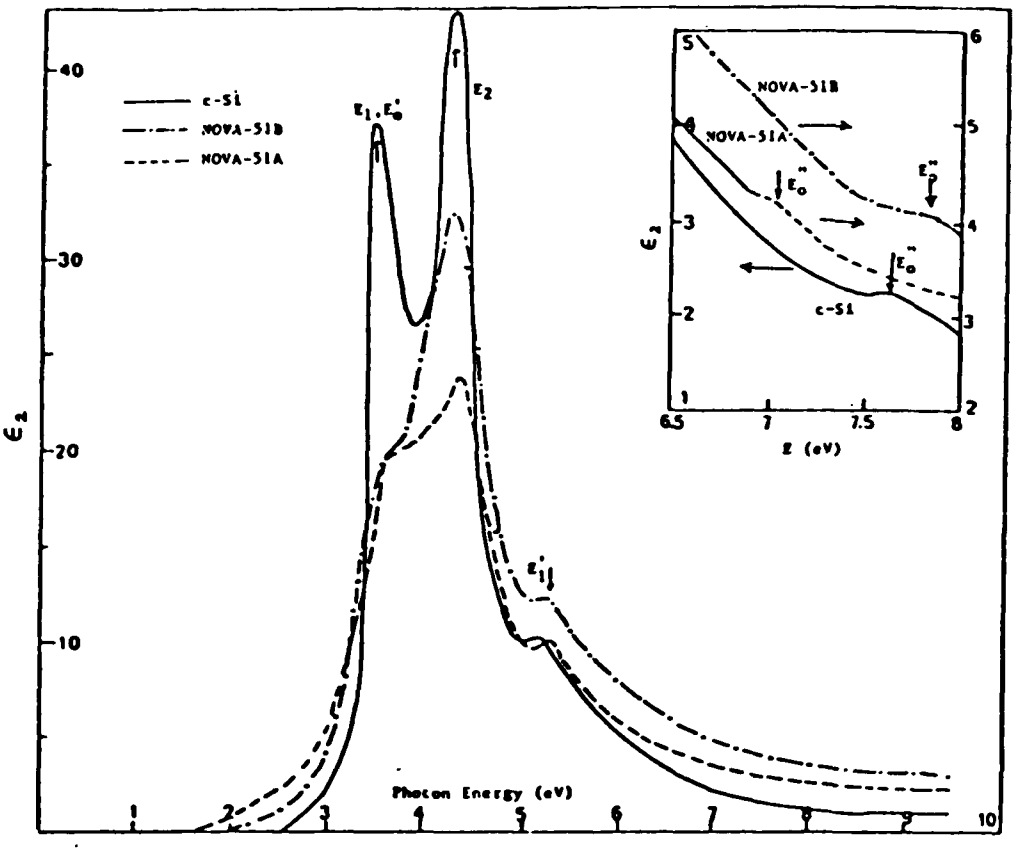

Fig.(3.4.9) The imaginary part $\epsilon_2(\omega)$ of the dielectric function for HTA-a-Si:H(B) and c-Si.

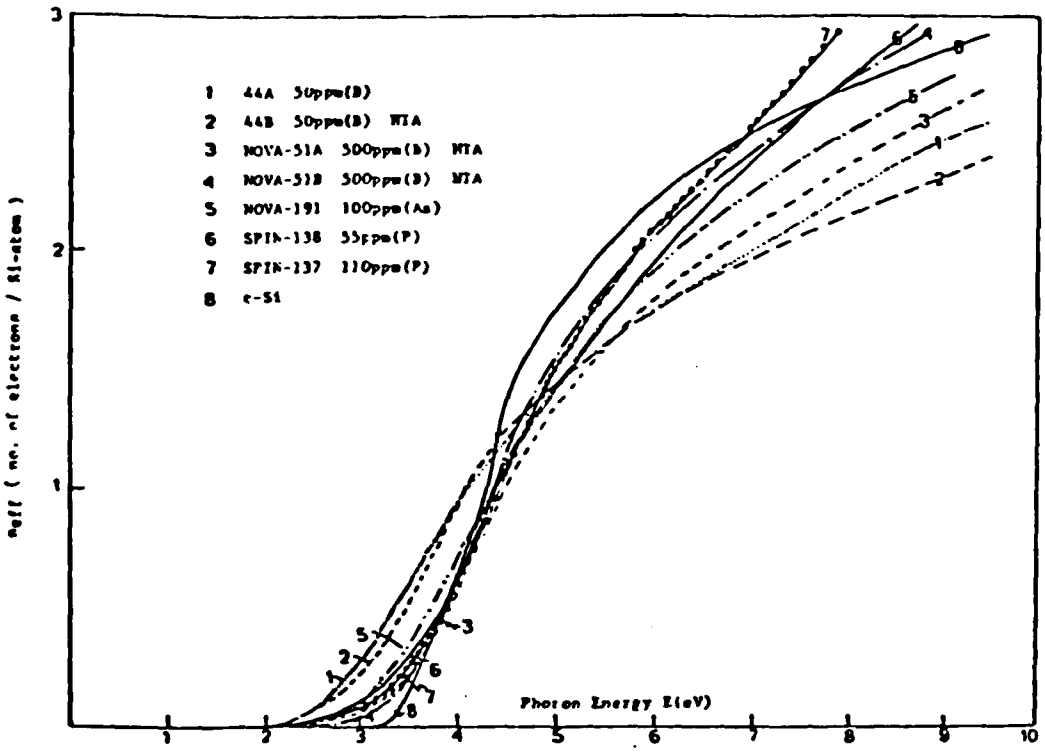

Fig.(3.4.10) The effective number of electrons per atom contributing to optical absorption.

References

1. A.F.Ioffe and A.R.Regel, Prog. Semicond. 4, 237 (1960).

2. D.E.Carlson and C.R.Wronski, Appl. Phys. Lett. 28, 671 (1976).

3. I.Shimizu, T.Komatsu, K.Saito and E.Inoue, J.Non-Cryst. Solids, 35-36, 773 (1980).

4. P.G.Le Comber, W.E.Spear and A.Ghaith, Electron Lett. 15, 79 (1979).

5. D.E.Polk, J. Non-Cryst. Solids, 5, 365 (1971).

6. M.H.Brodsky, R.S.Title, K.Weiser and G.D.Pettit, Phys. Rev. B1, 2632 (1970).

7. W.E.Spear and P.G.Le Comber, J. Non-Cryst. Solid, 8-10, 727 (1972).

8. S.Ovshinsky and A.Madan, Nature, 276, 482 (1978).

9. J.A.McMillan and E.M.Peterson, J. Appl. Phys. 50, 5238 (1979).

10. R.Fisch and D.C.Licciardello, Phys. Rev. Lett. 41, 889 (1978).

11. H.Muller, H.Ryssel and I.Ruge, Proc. of 2nd Int. Conf. on Ion Implentation (Springer-Verlag Press, ed. by Ruge et al.) (1971), p.85.

12. A.Madan, S.R.Ovshinsky and E.Benn, Phil. Mag. B40, 259 (1979).

13. Z.Iqbal, A.P.Webb and S.Veprek, Appl. Phys. Lett. 36, 136 (1980).

14. H.Matsumura, Appl. Phys. Lett. 36, 439 (1980).

15. H.Matsumura, Proc. 15th Int. Conf. on Phys. of Semiconductors, p. 1253 (1980).

16. H.Matsumura, J. Appl. Phys. 52, 291 (1981).

17. H.Matsumura, K.Sakai, Y.Kawakyn and S.Furukawa, J. de Physique 42, C4-209 (1981).

18 H.Matsumura, Y.Nakagome and S.Furukawa, Appl. Phys. Lett. 36, 439 (1980).

19. T.Shimada, Y.Katayama and S.Horigome, Jap. J. Appl. Phys. 19, 265 (1980).

20. C.J.Fang, L.Ley, H.R.Shanks, K.J.Gruntz and M.Cardona, Phys. Rev. B15, (1981).

21. T.Shimada and Y.Katayama, in Proc. 15th Int. Conf. on Phys. of Semiconductors, p. 1245 (1980).

22. S.Veprek and V.Mareck, Soled State Electronics, 11, 683 (1968).

23. A.Matsuda, S.Yamasaki, K.Nakagawa, H.Okushi, K.Tamaka, S.Izima, H.Matsumura and H.Yamamoto, Japan J. Appl. Phys. 19, L305 (1980).

24. A.Matsuda, S.Yamasaki, H.Okuski, S.Izima, K.Tanaka, H.Yamamoto and H.Matsumura, ibid (1981).

25. W.E.Spear, G.Willke, P.G.Le Comber and A.G.Fritzgerald, Journal de Physique, 42, C4-257 (1981).

26. R.Tsu, M.Izu, S.R.Ovshinsky and F.H.Pollak, Solid State Commum. 36, 817 (1980).

27. R.Tsu, M.Izu, V.Cannella, S.R.Ovshinsky, G.J.Jan and F.H.Pollak, Proc. of the 15th Int. Conf. Phys. of Semiconductors, Kyoto (1980); J. Phys. Japan Supp. A49, 1249 (1980).

28. R.Tsu, S.S.Chao, M.Izu, S.R.Ovshinsky, G.J.Jan and F.H.Pollak, Proc. of the 9th Int. Conf. of Amorphous and Liquid Semicond. Grenohle, France (1981).

29. K.Tanaka, K.Nakagawa, A.Matsuda, H.Matsumura, H.Yamamoto, S.Yamasaki, H.Okusi and S.Izima, Proc. 12th Conf. Solid State Decices, Tokyo (1980).

30. T.Hamasahi, H.Kurate, M.Hirose and Y.Osaka, Appl. Phys. Lett. 37, 1084 (1980).

31. See, for example, R.Tsu, in Defects in Semiconductors, eds. J. Narayan and T.Y.Tan (North Holland, N.Y. 1980), p.445 and references therein.

32. F.H.Pollak in Proc. of the Soc. of Photo-Optical Instrumentation Eng., Bellingham, Washington, 276, 142 (1981).

33. M.Cardona, Modulation Spectroscopy, Academic Press, (1969).

34. D.E.Aspnes, Handbook on Semiconductors, ed. by M.Bakkanshi Vol. 2, (North-Holland, Amsterdam, 1980), p.109.

35. Y.Hamakawa and T.Nishino in Optical Properties of Solids:New Developments, ed. by B.O.Serphin (North-Holland, Amsterdam, 1976), p.256.

36. H.Okamoto, Y.Nitta, T.Adachi and Y.Hamakawa, Surface Sci. 86, 486 (1979).

37. E.C.Freeman, D.A.Anderson and W.Paul, Phys. Rev. B21, 4721 (1980).

38. S.Nonomura, H.Okamoto, T.Nishino and Y.Hamakawa, Journal de Physique, 42, C4-261 (1981).

39. U.Gerhardt and G.W.Rublof, Applied Optics 8, 305 (1969).

40. S.S.M.Lu, F.H.Pollak and P.M.Raccah, Phys. Rev. B17, 1970 (1978).

41. S.S.M.Lu, Ph.D. Thesis, Yeshiva University, 1976 (unpublished).

42. J.Ziman, J. Phys. C4, 3129 (1971).

43. B.Kramer and J.Truesch, in Proceedings of the Twelfth Int. Conf. on Phys. of Semiconductors, Stuttgart, (1974).

44. M.H.Cohen, J.Singh and F.Yonezewa, J. Non-Cryst. Solids 35-36, 55 (1980).

45. J.D.Joannopoulos and M.C.Cohen, Phys. Rev. B1, 2644 (1973).

46. J.Singh, Phys. Rev. B23, 456 (1981).

47. K.Tanaka and R.Tsu, Phys, Rev. B24, 2038 (1981).

48. D.Weaire and M.F.Thorpe, Phys. Rev. B4, 2058 (1971).

49. M.F.Thorpe and D.Weaire, Phys. Rev. B4, 3518 (1971).

50. D.Weaire and M.F.Thorpe, "Electronic Structure of Amorphpus Semiconductors", in Computational Methods for Large Molecules and Localized States in Solids, ed. by F.Herman, A.D.McLan and R.K.Nesbet (Plenum, New York, 1973), p.208.

51. P.W.Anderson, Phys. Rev. 109, 1492 (1958).

52. E.A.Davis, Topics in Applied Physics: Amorphous Semiconductors, ed. by M.H.Brofsky Vol. 36, (Springer-Verlag, New York, 1979), p.42.

53. N.F.Mott and E.A.Davis, Electronic Processes in Non-Crystalline Materials, 2nd ed. (Oxford University Press, Oxford).

54. M.F.Thorpe and D.Weaire, "The Theory of the Electronic Density of States in Amorphous Semiconductors", in Amorphous and Liquid Semiconductors, ed. by J.Stukd and W.Brenig (Tatlor and Francis, London 1974), p.917.

55. N.Shevchik, "Photoelectron Spectroscopy of Amorphous Group IV and III-II Semiconductors", in Tetrahedrally Bonded Amorphous Semiconductors, ed. by M.H.Brodsky, S.Kirpatrick and D.Weaire (A.I.P., New York 1972), p.72.

56. W.E.Spear, "Photoemission Spectroscopy and the Electronic Structure of Amorphous Studies of Ge and Si", in Amorphous and Liquid Semiconductors, ed. by J.Stuke, W.Brenig (Taylor and Francis, London 1974), p.499.

57. J.Tauc, "Optical Properties of Amorphous Semiconductors", in Amorphous and Liquid Semiconductors, ed. by Tauc (New York: Plenum, 1974), p.159.

58. M.L.Theye, Optical Semiconductors, ed. by J.Stuke, W.Brenig (London: Taylor and Francis, 1974), p.479.

59. H.Richter and L.Ley, Journal de Physique, 42, C4-261 (1981).

60. A.I.Gubanov, Quantum Theory of Amorphous Conductors (New York: Consultants Bureau, 1965).

61. M.H.Cohen, H.Fritzsche and S.R.Ovshinsky, Phys. Rev. Lett. 22, 1065 (1969).

62. M.H.Brodsky, R.S.Title, K.Weiser and P.G.Pettit, Phys. Rev. B1, 2632 (1970).

63. W.E.Spear and P.G.Le Comber, Phil. Mag, 33, 935 (1976).

64. P.G.Le Comber, W.E.Spear, Phys. Rev. Lett. 25, 509 (1970).

65. W.E.Spear and P.G.Le Comber, Solid State Commun. 17, 1193(1975).

66. N.J.Shevchik and W.Paul, J.Non-Cryst. Solids, 8-10, 381 (1972).

67. W.Beyer and J.Stuke, Phys. Stat. Sol. 30, 511 (1975).

68. A.J.Lewis, G.A.N.Connel, W.Paul, J.R.Pawlik and R.J.Temkin, Tetrahedially Bonded Amorphous Semiconductors, ed. by M.Brodsky, S.Kirkpatrick and D.Weaire (A.I.P. New York 1974), p.27.

69. W.Paul, A.J.Lewis, G.A.N.Connel and T.D.Moustakas, Solid State Comm. 20, 969 (1976).

70. N.F.Mott, Phil. Mag. 19, 835 (1969).

71. R.A.Street, Adv. Phys. 25, 397 (1976).

72. Y.Uchida, T.Ichimura, M.Vene and M.Ohsawa, Proceeding of the 9th Int. Conf. on Amorphous and Liquid Semiconductors, Grenoble, France (1981).

73. D.E.Carlson, Prog. Cryst. Growth Charact. 4, 173 (1981).

74. R.C.Chittick, J. Non-Cryst. Solid, 3, 255 (1970).

75. F.H.Pollak, R.Tsu and E.E.Mendz, in Laser and Electron Beam Processing of Materials, ed. by C.W.White and P.S.Poercy (New York: Academic Press, 1980), p.195.

76. R.Loudon, Adv. in Phys. 13, 423 (1964).

77. M.Born and M.Bradburn, Proc. Roy. Soc. A188, 161 (1947).

78. H.M.J.Smith, Phil. Trans. A241, 105 (1948).

79. R.Shuker and R.Gamon, Phys. Rev. Lett. 25, 222 (1970); in Proc. 2nd Intern. Conf. Light Scattering in Solids, Paris, 1971 (Flammarion Sciences, Paris, 1971), p.334.

80. J.F.Morhange, G.Kanellis and M.Balknaski, Solid State Comm. 31, 805 (1979).

81. R.Tsu, J.E.Baglin and T.Y.Tan, Private Commun.

82. Z.Igbal, S.Veprek, A.P.Webb and P.Capezzuto, Solid State Comm. 37, 993 (1981).

83. G.Dolling, Elastic Scattering of Neutron Symp. Chalk River 2, 37 (1972).

84. B.N.Brockhouse, Phys. Rev. Lett. 2, 256 (1959); H.Palevsky, D.J.Hughes, W.Kley and E.Tunkelo, Phys. Rev. Lett. 2, 258 (1959).

85. U.Fano, Phys. Rev. 124, 1866 (1961).

86. M.Chandrasekhar, J.B.Renucci and M.Cardona, Phys. Rev. B17, 1623 (1978).

87. M.Cardona and F.H.Pollak, Phys. Rev. 142, 530 (1966).

88. M.Cardona, K.L.Shaklee and F.H.Pollak, Phys. Rev. 154, 696 (1967).

89. H.R.Philip and H.Ehremeich, Phys. Rev. 129, 1550 (1963).

90. H.R.Philip and H.A.Taft, Phys. Rev. 120, 37 (1960).

91. H.R.Philip, J.Phys. Chem. Solid, 32, 1935 (1971).

92. D.T.Pierce and W.E.Spicer, Phys. Rev. B5, 3017 (1972).

93. G.Weiser, D.Ewald and M.Milleville, J. of Non-Cryst. Solids, 35&36, 447 (1980).

94. D.Wald, M.Milleville and G.Weiser, Phil. Mag. 40, 291 (1979).

95. G.J.Jan, F.H.Pollak and R.Tsu, to be published in Solar Energy Materials.

96. J.D.E.McIntyre, Optical Properties of Solids: New Developments, ed. by B.O.Seraphin (North-Holland, Amsterdam, 1976), p.555.

97. M.Cardona, in Optical Properties of Solids, ed. by S.Nudelman and S.S.Mitra (Plenum, New York, 1969), p.137.

98. See, for example, M.L.Theye in Optical Properties of Solids - New Developments, ed. by B.O.Seraphin (North Holland, N.Y., 1976), p.355 and references therein.

99. See, for example, G.A.N.Connell in Amorphous Semiconductors, ed. by M.H.Brodsky (Springer - Verlag, N.Y., 1979), p.73 and references therein.

100. See, for example, W.Paul and D.A.Anderson, Solar Energy Materials 5, 229 (1981) and references therein.

101. J.R.Chelikowsky and M.L.Cohen, Phys. Rev. B10, 5095 (1974).

102. See, for example, J.Stuke and G.Zimmerer, Phys. Stat. Sol. (b)49, 513 (1972).

103. D.E.Aspnes in Proc. Symposium on Laser and Electron Beam Processing of Electronic Materials, eds. C.L.Anderson, C.K.Celler and G.A.Rozgonyi (Electrochemical Society, Princeton, 1980), p.414.

```
      IMPLICIT COMPLEX*16(F-G)
      DIMENSION U(300),XNEFF(300),Y1(300)
      DIMENSION F(300),R(300),THI(21),E(50),YI(300),
     1 THA(300),ON(300), OK(300),ALF(300),W(300),
     2 TRANS(300),EO(300),ET(300)
      TH=5.5E-1
  900 READ(5,555,END=999) N5
  555 FORMAT(I5)
      WRITE(6,82) N5
   82 FORMAT(//1X,4HN5= ,I5)
      N5P=N5+1
      ALF(1)=0.0
      EO(1)=0.0
      ET(1)=0.0
      OK(1)=0.0
      ON(1)=0.0
      TRANS(1)=0.0
      DO 3 I=1,N5
      READ(5,5) F(I),R(I)
    5 FORMAT(F5.3,F5.3)
      I1=I-1
    3 CONTINUE
    7 RMAX=R(I1)
      EMAX=E(I1)
      I2=I1-1
      WRITE(6,80) (E(I),I=1,N5)
   80 FORMAT(//,10(2X,F7.4,3X))
      WRITE(6,80) (R(I),I=1,N5)
   10 P(1)=1
      DO 200 I=2,40
  200 P(I)=P(I-1)+.6
      PMAX=P(3)
      I4=1
      I3=0
   14 IF (P(I3) .EQ. PMAX) GO TO 45
      I3=I3+1
      WRITE (6,15) P(I3)
   15 FORMAT(1H1,5H P = , 1PE15.4///)
      WRITE (6,16)
   16 FORMAT(1H ,11H WAVELENGTH,2X,6HENERGY,1X,
     1 12HREFLECTIVITY,4X,5HALPHA,6X,1HN,8X,1HK,
     2 8X,7HTHETA,8X,1HT,10X,2HEO,8X,2HET,//)
      DO 42 J=2,I2
      DO 21 I=1,I1
      IF (E(I).EQ.E(J)) GO TO 17
      XD=R(I)
      IF(ABS(XD-1.) .GT. 1E-10) GO TO 70
      XLD=XD-1.
      GO TO 72
   70 XLD=ALOG(XD)
   72 CONTINUE
      XE=R(J)
      IF(ABS(XE-1.) .GT. 1E-10) GO TO 71
```

```
      XLE=XE-1.
      GO TO 73
   71 XLE=ALOG(XE)
   73 CONTINUE
      RM=XLO-XLE
      XEJI=E(J)**2-E(I)**2
      XCC=RM/XEJI
      YI(I)=XCC
      GO TO 19
   17 XIM=R(I-1)
      IF(ABS(XIM-1.) .GT. 1E-10) GO TO 90
      XIMLG=XIM-1.
      GO TO 92
   90 XIMLG=ALOG(XIM)
   92 CONTINUE
      XIP=R(I+1)
      IF(ABS(XIP-1.) .GT. 1E-10) GO TO 91
      XIPLG=XIP-1.
      GO TO 93
   91 XIPLG=ALOG(XIP)
   93 CONTINUE
      YJIM=E(J)**2-E(I-1)**2
      YJIP=E(J)**2-E(I+1)**2
      XJ=R(J)
      XJJ=ALOG(XJ)
      YY=0.5*((XIMLG-XJJ)/YJIM+(XIPLG-XJJ)/YJIP)
      YI(I)=YY
      Z1=YI(J)
   19 IF(I .EQ. I1) GO TO 23
   21 CONTINUE
   23 DO 25 I=1,I5
      YI(I)=(YI(I)+YI(I+1))*(E(I+1)-E(I))*.5
      IF(I .EQ. I2) GO TO 27
   25 CONTINUE

   27 THA(J)=0
      YI(J-1)=Z1*(E(J)-E(J-1))
      YI(J)=Z1*(E(J+1)-E(J))
      DO 29 I=1,I2
      THA(J)=THA(J)+YI(I)*E(J)/3.14159
      IF(I.EQ. I2) GO TO 31
   29 CONTINUE
   31 Y=ABS(EMAX-E(J))
      XX=R(J)/RMAX
      IF(ABS(XX-1.) .GT. 1E-10) GO TO 61
      XLG=XX-1.
      GO TO 65
   61 XLG=ALOG(XX)
   65 YY=ABS((EMAX+E(J))/Y)
      IF(ABS(YY-1.) .GT. 1E-10) GO TO 62
      YMG=YY-1.0
      GO TO 64
   62 YMG=ALOG(YY)
```

```
   64 CONTINUE
      THA(J)=THA(J)+(0.159154)*XLG*YMG
      Z=0.0
   32 DO 33 I=1,50
      Z=Z+1.0
      EEC=E(J)/FMAX
      THA(J)=THA(J)+(P(I3)*((2.0*Z-1.0)**(-2))*
     1EEC**(2*I-1))/3.14159
   33 CONTINUE
      ON(J)=(1.0-R(J))/(1.0+R(J)-2.0*SQRT(R(J))*
     1COS(THA(J)))
      OK(J)=(2.0*SQRT(R(J))*SIN(THA(J)))/(1.0+
     1R(J)-2.0*SQRT(R(J))*COS(THA(J)))
   42 CONTINUE
   44 DO 46 J=2,N5
      W(J)=1.23946/E(J)
      ALF(J)=4.0*3.14159*OK(J)/W(J)
      U(J)=ATAN(2.0*OK(J)/((ON(J)*ON(J))+(OK(J)*
     1OK(J))-1.0))
      TRANS(J)=(((1.0-R(J))**2)+(4.0*R(J)*SIN(U(J))*
     1SIN(U(J))))*EXP(-ALF(J)*TH)/
     2(1.0-R(J)*R(J)*EXP(-2.0*ALF(J)*TH))
      EO(J)=ON(J)**2-OK(J)**2
      ET(J)=2*ON(J)*OK(J)
      WRITE(6,35) W(J),E(J),R(J),ALF(J),ON(J),OK(J),
     1THA(J),TRANS(J),EO(J),ET(J)
   35 FORMAT(1H ,1P10E10.2)

   46 CONTINUE
C     THIS PARTS ARE CALCULATING THE EFFECTIVE DENSITY
C     OF ELECTRONS NEFF(E) CONTRIBUTING TO ABSORPTION
C     BELOW ENERGY E.
C     THE RESULTS OF NEFF(E) MUST MULTIPY THE ORDER
C     OF OF MAGNITUDE ( TEN OF 20 ).
      CONST = 4.6195
      DO 300 J=2,I2
      SUM=0.0
      DO 400 I=2,J
      DE=E(I)-E(I-1)
      XFNE=E(I)*ET(I)*DE
      SUM=SUM+XFNE
  400 CONTINUE
      XFNEFF(J)=SUM*CONST
      Y1(J)=XFNEFF(J)
  300 CONTINUE
      WRITE (6,500) ((XFNEFF(J),J=1,I2))
  500 FORMAT(1H,1P10E10.2)
      CALL MPLOT ( Y1,1,1,N5,.1,.1)
      GO TO 14
   45 I4=I4+1
  999 STOP
      END
```

```
      SUBROUTINE GPLOT(A,IDMS,IMAX,JMAX,YMIN,DY)
      DIMENSION A(1),IB(11),IOUT(101),ISYB(11)
      DATA ISYB/1H1,1H2,1H3,1H4,1H5,1H6,1H7,1H8,1H9,1HA,1HB/
      DATA IBLAK,IDOT,IMSYB/1H ,1H.,1HM/
      IXRG=100
      AMIN=A(1)
      AMAX=A(1)
      J1=0
      DO 1 J=1,JMAX
      DO 5 I=1,IMAX
      I1=I+J1
      IF(A(I1)-AMIN)3,2,2
    3 AMIN=A(I1)
    2 IF(A(I1)-AMAX) 5,5,4
    4 AMAX=A(I1)
    5 CONTINUE
    1 J1=J1+IDMS
      XRANG=AMAX-AMIN
      DX=XRANG/(IXRG-1)
      IF(DX-1.E-37)300,300,22
   22  XSCAL=1.
      IF(XSCAL-DX) 23,21,20
   20  XSCAL=XSCAL*0.1
      IF(DX-XSCAL)20,21,21
   23  XSCAL=XSCAL*10.
      IF(DX-XSCAL)25,21,23
   25  XSCAL=XSCAL*0.1
   21  XSCAL=XSCAL*0.1
       I=DX/XSCAL+0.5
      DX=I*XSCAL
      IF(AMIN*AMAX) 30,30,31
   30  AM=0.
       I=1
       DX10=DX*10.
   34 IF(AM-AMIN) 32,32,33
   33  AM=AM-DX10
       I=I+10
       GO TO 34
   32 AN=0.
    37  IF(AN-AMAX) 35,36,36
   35 AN=AN+DX10
       I=I+10
       GO TO 37
   36 IF(I-101) 40,40,41
   41  DX=DX+XSCAL
      GO TO 30
   40  IXRG1=I
   45  IRX=0
      T=AM/DX
       IF(T) 90,90,92
   90  IB(1)=T-0.5
       GO TO 60
```

```
   92    IB(1)=T+0.5
         GO TO 60
   31    I=AMIN/DX-0.5
         AM=I*DX
   52    IF(AM-AMIN) 50,50,51
   51     AM=AM-DX
         GO TO 52
   50     I=(AMAX-AM)/DX+1.5
         IXRG1=(I-2)/10*10+11
         IF(IXRG1-101) 55,55,54
   54    DX=DX*XSCAL
         GO TO 31
   55    IF( ABS(AM/DX)-3000.)145,55,56
   56      IBX=AM*(1.0+0.5*DX)/DX
         IB(1)=0
   60    T=YMIN/DY
         IF(T)93,93,94
   93    IY=T-0.5
         GO TO 95
   94     IY=T+0.5
   95    IRY=0
         T=DX+0.5*XSCAL
          IF(IY-700)13,13,14
   14    IRY=IY
         IY=0
    13  WRITE(6,9111)
         WRITE(6,100) IBX,T,IRY,DY
 9111    FORMAT(1H1)
  100    FORMAT(/,1X,'RELATIVE ZERO OF X-AXIS IS ',I5,20X,
        X'SCALE OF Y-AXIS IS ',E12.4,
        Y       /,1Y,'RELATIVE ZERO OF Y-AXIS IS ',I5,20X,
        Y'SCALE OF Y-AXIS IS ',E12.4/)
          JR=1
         DO 70 I=11,IXRG1,10
          JR=JR+1
    70    IB(JR)=IB(JR-1)+10
           WRITE(6,102)(IB(I),I=1,JR)
    102     FORMAT(1H ,I13,10I10)
         JM1=(JMAX-2)/10*10+11
         J1=0
        DO 80 J=1,JM1
        DO 81 I=1,IXRG1
    81    IOUT(I)=IMARK
         ICM=10
        IF(J-2)141,142,143
    142    ICM=5
        GO TO 145
    143 IF(J-JM1+1)144,142,141
    144 IF(J-J/10*10-1)145,141,145
    141 ICM=1
    145 DO 151 I=1,IXRG1,ICM
    151   IOUT(I)=IMARK
```

```
      IF(J-J/5*5-1) 152,153,152
  153  IOUT(2)=IDOT
       IOUT(IXRG1-1)=IDOT
  152 IF(J-JMAX) 156,156,165
  156 DO 160 I=1,IMAX
       I1=J1+I
       ID=(A(I1)-AM)/DX+1.5
      IF(IOUT(ID)-IBLAK) 161,162,161
  161 IF(IOUT(ID)-IDOT) 163,162,162
  163 IOUT(ID)=ISYB
       GO TO 160
  162 IOUT(ID)=ISYB(I)
  160   CONTINUE
  165 IF(IC-1) 170,171,170
  171   WRITE(6,103) IY,(IOUT(K),K=1,IXRG1)
      IY=IY+10
       GO TO 80
  170  WRITE(6,104)(IOUT(K),K=1,IXRG1)
   80 J1=J1+IDES
      WRITE(6,102)(IB(I),I=1,JR)
  301   RETURN
  103 FORMAT(1H ,I11,1X,101A1)
  104 FORMAT(1H ,12X,101A1)
C
  300   WRITE(6,105) DX
       GO TO 301
  105 FORMAT(' DX=',E12.4,5X,'ALL CURVES ARE STRAIGHT LINES')
      RETURN
      END
```